Contamination of Mafic to Ultramafic Magmas by Sulfur-bearing Sediments: Evaluation of the Environment of Deposition and Tracing the Unique Signature of the Contaminants Through the Magma Using Multiple Sulfur and Iron Isotope Data

By

Russel Shane Hiebert

A Thesis submitted to the Faculty of Graduate Studies of

The University of Manitoba

in partial fulfilment of the requirements of the degree of

DOCTOR OF PHILOSOPHY

Department of Geological Sciences,

University of Manitoba

Winnipeg

ABSTRACT

In this thesis, multiple stable isotopes of sulfur ($\delta^{33}S$, $\delta^{34}S$, and $\Delta^{33}S$) and iron ($\delta^{56}Fe$) are used to identify the sources of sedimentary rock contamination at both the Voisey's Bay (Labrador, Canada) and the Hart (Ontario, Canada) magmatic Ni-Cu-platinum-group element (PGE) deposits. At both locations, sulfide minerals were formed in sedimentary rocks during diagenesis as a result of bacterial sulfate reduction, prior to interaction with the magmas that resulted in the formation of the sulfide mineralization. In the Hart area, both exhalite and graphitic argillite were formed under predominantly anoxic conditions with localized, or transient, oxygen oases in seawater. The fluid composition was a result of mixing of seawater with hydrothermal fluids. Sulfur in the sediments in the Hart area was derived from the reduction of sulfate that had been mass-independently fractionated in the anoxic Archean atmosphere prior to delivery to the seawater.

Multiple sulfur isotopes identified the sources of contamination in both the Voisey's Bay and Hart deposits, and determined that the Main Zone and Eastern Extension at Hart likely had different contaminants that provided sulfur to form the mineralization. Signatures of these contaminants were distinguishable up to a few hundred meters from the sulfide-rich zones, allowing this to be used as a geochemical tool to vector towards the mineralization. The iron isotopic composition of sulfides from the Voisey's Bay deposit was too heavily influenced by the host silicate magma to recognize the signature of contamination, but could be used to identify contamination in the Hart deposit. However, this data does not uniquely identify the source of contamination in the Hart deposit, and is not able to identify the signature of contamination at distances of more than a few meters from sulfide mineralization. These data sets have different sensitivity to contamination during equilibrium isotope exchanges with the silicate magma due to the difference in the initial concentration in the magma, as indicated the difference in the distance away from sulfide mineralization at which contamination can

still be recognized. In conclusion, based on this study, use of multiple isotope and elemental methods to determine the presence and extent of contamination is strongly recommended.

ACKNOWLEDGEMENTS

I would like to acknowledge the immeasurable assistance of my advisors and co-authors on these papers: Dr Andrey Bekker, Dr Michel Houlé, Dr Boswell Wing, and Dr Olivier Rouxel. Your input, advice, instruction, and support are greatly appreciated. The input of the reviewers and editors of my published papers also helped to improved the quality of this research. I also would like to thank all the members of my advisory committee, I enjoyed the discussions we had during the annual update meetings, and encouragement to finish up. I would also like to acknowledge the friends I have made among the students and staff in the department throughout the years I have been a student here. Finally, and most importantly, I would like to acknowledge the support and encouragement of my family, wife Rebekah, and daughters Lucy and Hope. Although the latter two may have been more of a distraction than a help at times, I finished in part for them.

For assistance in the work on the Voisey's Bay project, I acknowledge support from NSERC through the Discovery Grant program, Vale Inco Inc., and the Targeted Geoscience Initiative program of the Geological Survey of Canada. Discussion and help from Peter Lightfoot, Dawn Evans-Lamswood, Trevor Rice, and Mike Lesher were greatly appreciated.

For assistance in the work on the Hart area projects I would like to express my appreciation to Northern Sun Mining Corp. (formerly Liberty Mines Ltd.) for their logistical support, access to properties, information, and discussions with staff throughout this project. Discussions with, and advice from, Dr C. Michael Lesher (Laurentian University) during the course of this study was greatly appreciated. I also greatly appreciate the helpful reviews by S.J. Barnes, M. Fiorentini and P. Thurston, whose comments significantly added to these chapters, and editorial suggestions by Georges Beaudoin. Financial support for this project has been provided by the Targeted Geoscience Initiative 4 of the Geological Survey of Canada and Natural Sciences and Engineering Research Council of Canada (NSERC) Discovery and

Accelerator Grants to Andrey Bekker. I also thank Thi Hao Bui for technical assistance in the McGill Stable Isotope Laboratory.

I would like to dedicate this to my wife Rebekah, and my daughters, Lucy and Hope.

CONTRIBUTIONS OF THE AUTHORS

I am the primary author and researcher responsible for all data collected and written product in this thesis.

Dr Andrey Bekker is my primary advisor, and assisted by edited and revising all written material in this thesis. He also helped to design and develop the projects that make up this thesis, and assisted in fieldwork and sampling on the Voisey's Bay project.

Dr Michel Houlé is the primary contact with the Geological Survey of Canada, which served as a significant source of funding for this research. He served as an advisor, helped with designing and developing the Hart area projects, and assisted in fieldwork and sampling on these projects. He also assisted by editing, revising, and providing some photographs for use in the Hart area papers.

Dr Boswell Wing assisted in teaching me methods for sulfur extraction from these rocks and analysis using the mass spectrometer in his lab at McGill University. He also assisted with interpretation of the results of the stable isotope analysis. He assisted in editing and revising the written product for all papers.

Dr Olivier Rouxel performed the iron isotope analysis. He also assisted in editing and revision of the written product for all papers.

Table of Contents

LIST OF TABLES

List of Figures

CHAPTER 1: INTRODUCTION

1.1 RESEARCH OBJECTIVES

Magmatic Ni-Cu-(PGE) sulfide deposits are known to form from a variety of magma compositions and tectonic environments. However, they generally require a mafic-ultramafic magma to encounter an external sulfur source to produce significant accumulations of sulfide minerals (e.g. review by Naldrett, 2011).

In this thesis, I focus on two locales: Voisey's Bay, NL (Figures 1 & 2), and the Hart area of the Shaw Dome, within the Abitibi greenstone belt, ON (Figures 1 & 3). These project areas represent very different environments at the time of formation of the sulfide mineralization; the Hart deposit is associated within ~2.7 Ga komatiitic lava flows that thermomechanically eroded sulfidic sedimentary rocks (Houlé et al., 2010; Houlé and Lesher, 2011), whereas the Voisey's Bay deposit is associated with intrusion of a troctolitic magma into granulite-facies metamorphosed sulfidic paragneisses at ~1.3 Ga (Lightfoot et al., 2012). In these project areas, there are marked differences in both mode of magma emplacement and magma composition.

Additionally, differences in history of the country rocks that act as the source(s) of sulfur are significant. The Tasiuyak gneiss (TGN) associated with the Voisey's Bay deposit is a sulfidic and graphitic, garnet-bearing paragneiss deposited in the Proterozoic prior to peak metamorphism to granulite-facies during the Torngat orogen ~1.85 Ga (Ryan, 2000). The sedimentary rocks in the Hart area underwent some degree of diagenesis prior to the eruption of the komatiitic lava flows, and may have even been largely unconsolidated during eruption in other locations within the Abitibi greenstone belt (Houlé et al., 2008).

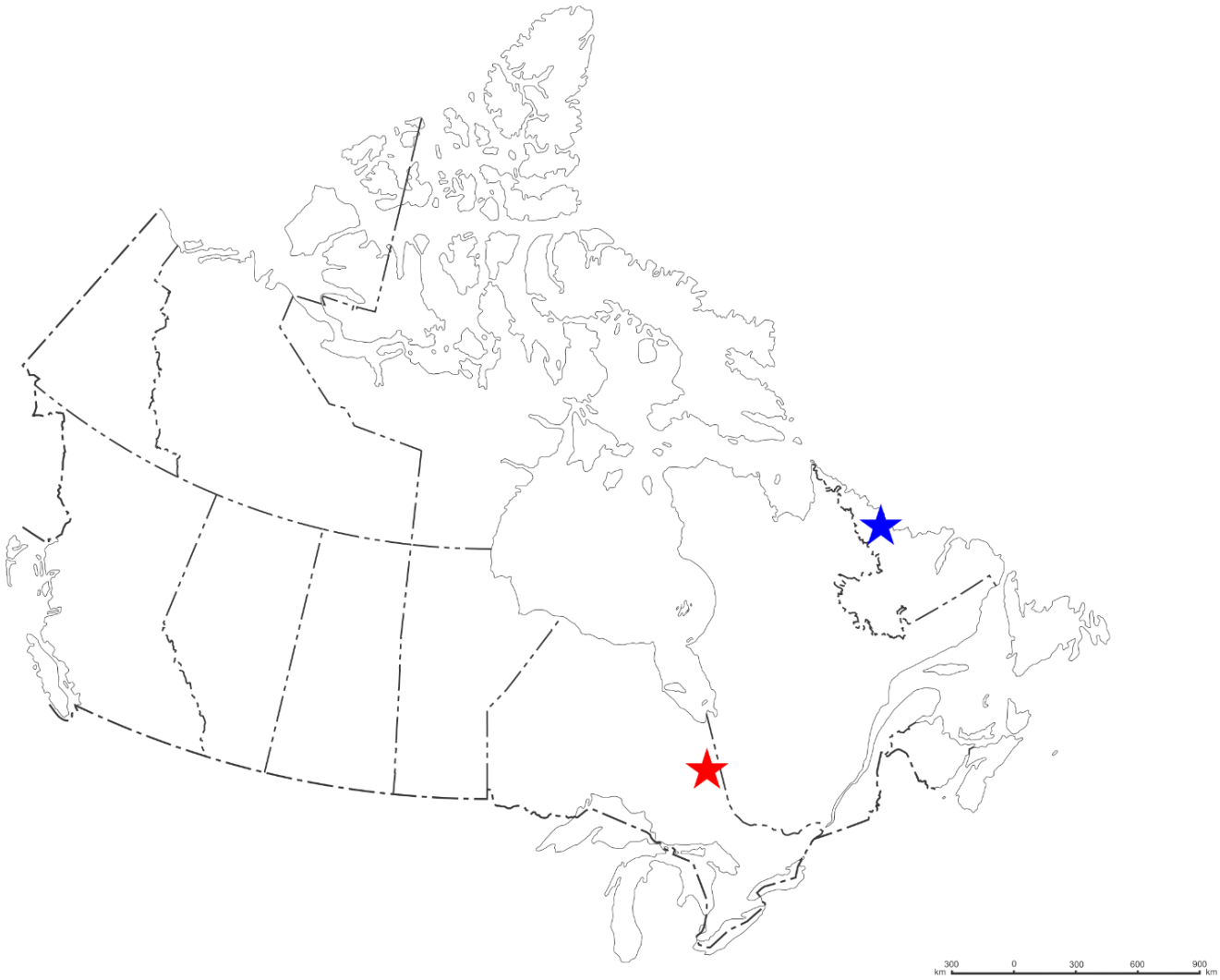

Figure 1: Map of Canada showing approximate project locations. The Voisey's Bay area is indicated by the blue star, and the Hart deposit area (Shaw Dome) is indicated by the red star.

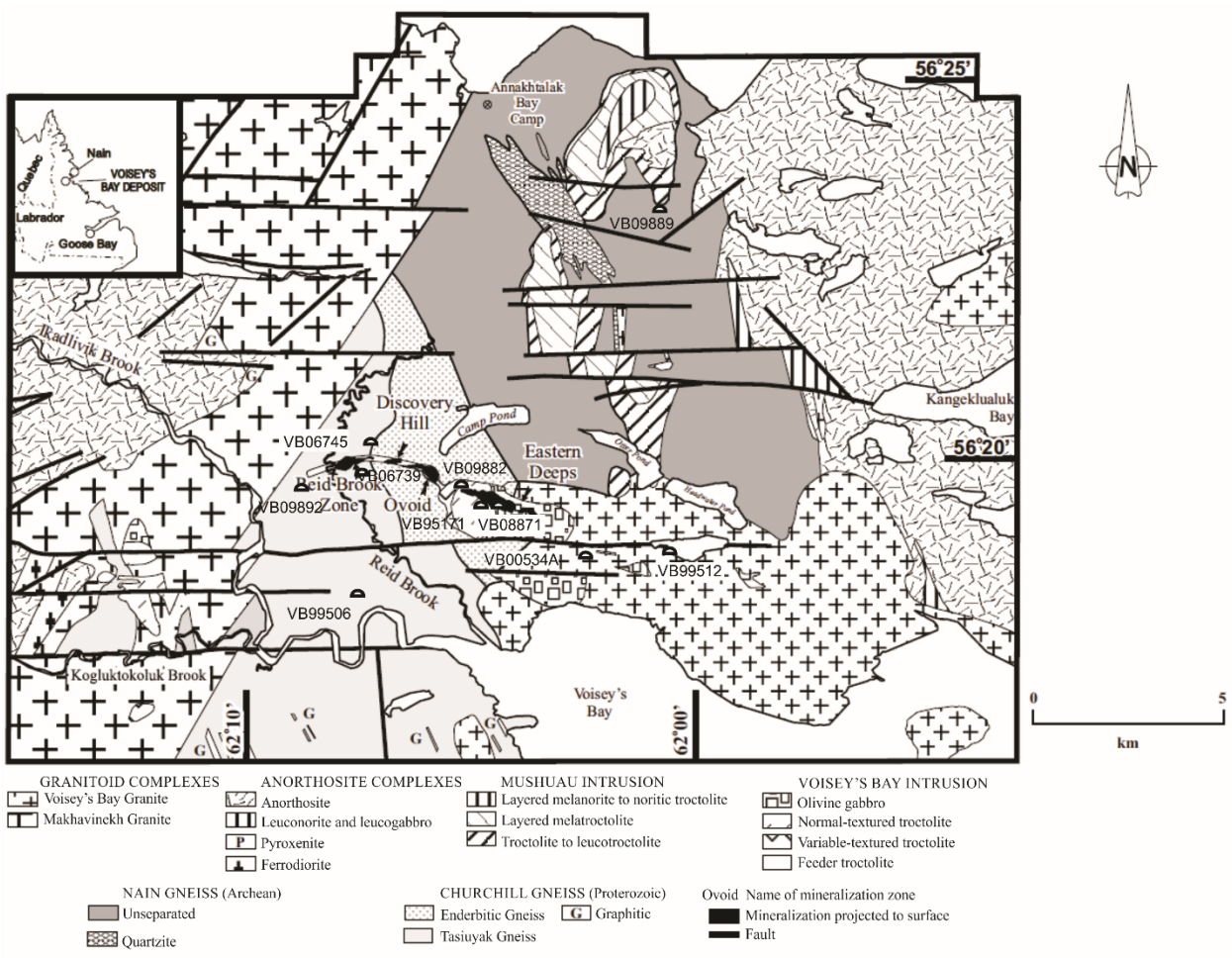

Figure 2: Geologic map of the Voisey's Bay area with location of sampled drill holes shown. Modified from Evans-Lamswood et al. (2000).

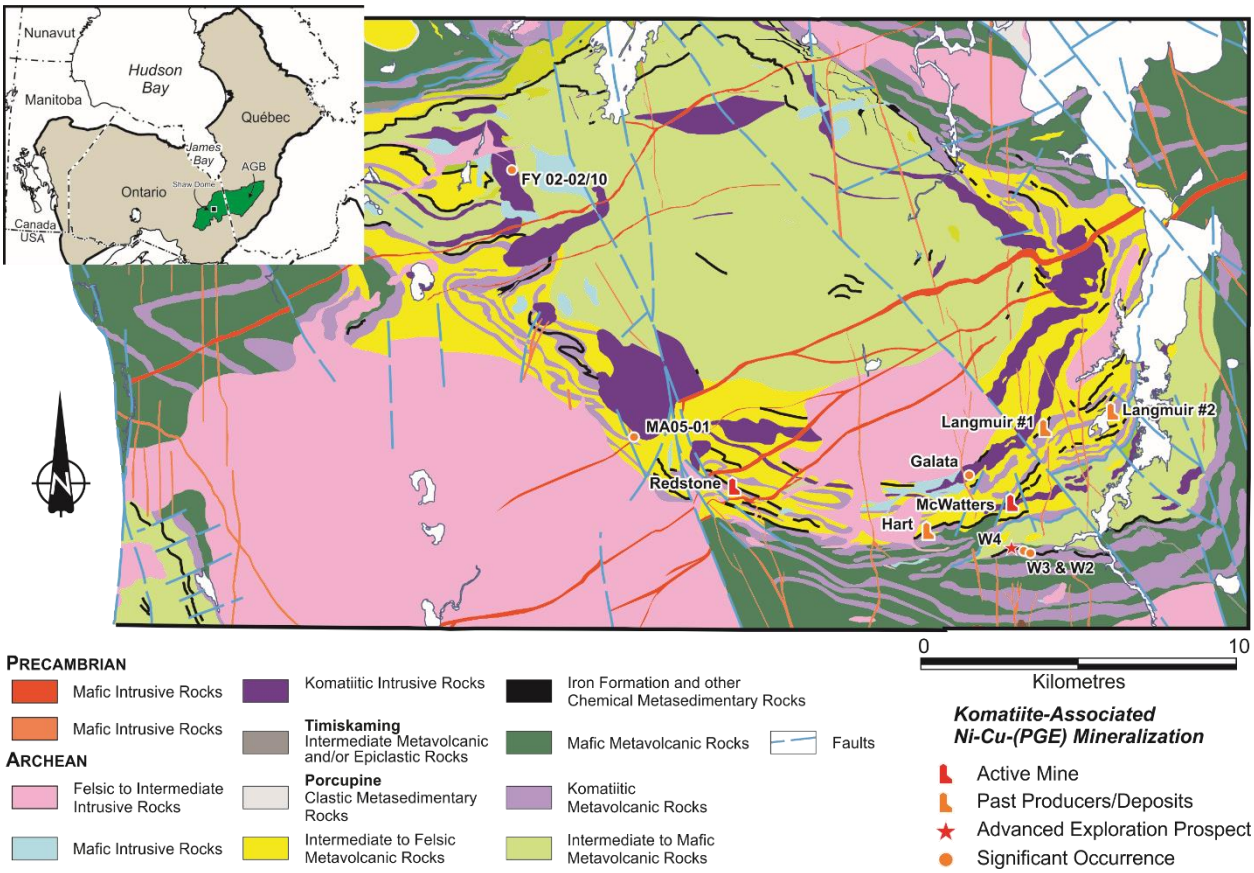

Figure 3: Geological map of the Shaw Dome, Abitibi greenstone belt (modified from Houlé et al. 2010a, b).

The differences between the magmas at Voisey's Bay and Hart, combined with the differences in the country rocks that serve as sulfur sources, allows for the demonstration of the usefulness of multiple S and Fe isotope systems. When these isotopic systems are used along with petrography, and whole rock geochemistry they can provide a link between the magmatic sulfide deposits, the source of sulfur and the conditions at the time of deposition. This thesis consists of three separate, but related, projects (Chapters 2 – 4). The Voisey's Bay project examines the relationship between the magmatic sulfide deposit and the TGN and the impact of silicate magma to sulfide liquid mass ratio (R-factor) on the isotopic signature of contamination; the Hart deposit project examines the source of sulfur for the two mineralized zones within the Hart deposit and traces the signature of contamination moving away from the mineralized zones within the host komatiite; and the Hart Area Sedimentary Rocks project examines the depositional environment and water column chemical characteristics during the deposition of the sedimentary units that provide sulfur to the Hart deposit.

Each of these projects attempts to answer several key questions:

1. As magmatic sulfide deposits are generally linked to external S-bearing contaminants, typically sedimentary rocks, how can multiple S and Fe isotope data be used to interpret the environmental conditions during deposition and diagenesis of the sedimentary rocks, and how the sulfide was formed in these environments?
2. Can multiple S and Fe isotope data identify sources of contamination in magmatic systems where traditional S isotope compositions ($\delta^{34}S$) of the sulfides fall within the mantle range?
3. Can these methods be used to vector towards zones of mineralization in a magmatic sulfide system? Within a magmatic sulfide system, how does reaction and isotopic exchange affect these isotopic values where silicate magma to sulfide liquid ratios are high?

These questions are all directly related to the processes and environments of formation for magmatic sulfide deposits.

1.1.1 Voisey's Bay Project Objectives (Chapter 2: The role of paragneiss assimilation in the origin of the Voisey's Bay Ni-Cu sulfide deposit, Labrador: multiple S and Fe isotope evidence)

The Voisey's Bay Ni deposit is hosted by the generally troctolitic Voisey's Bay Intrusion, part of the ca. 1.3 Ga Nain Plutonic Suite, at the boundary between Archean Nain orthogneisses (NGN), of the Nain province, and Proterozoic Tasiuyak paragneisses (TGN), of the Churchill province (Figure 1; Ripley et al., 1999; 2002; Lightfoot et al., 2012). The objectives of this project are to use multiple sulfur isotopes to identify the method of sulfur isotope fractionation in the Tasiuyak gneiss, and determine if this signature was passed from the Tasiuyak gneiss to the Voisey's Bay mineralization, as the Tasiuyak gneiss is widely regarded to be the most likely source of S for the Voisey's Bay magmatic sulfide deposit (Lightfoot et al., 2012). This defines a new method for the use of multiple sulfur isotopes to identify crustal contamination in igneous rocks by sulfide-bearing country rocks. Additionally, this project intends to evaluate mass-balance equations to estimate the R-factor (ratio of silicate magma mass to sulfide magma mass in equilibrium) for the Voisey's Bay magmatic system, and to test the sensitivity of different stable isotope systems to the R-factor.

The objectives of this project are designed to address all three of the key questions related to this thesis. These questions are addressed by analyzing the Tasiuyak gneiss, which was derived from a sedimentary protolith, to determine if the signature of biological processing of sulfur is present. Additionally, the $\delta^{34}S$ data from three of the four mineralized zones in the Voisey's Bay deposit are within the range of values considered normal for uncontaminated mantle-derived magmas (Ripley et al., 1999; 2002), and multiple S isotope ratios are required to identify contamination. Finally, the deposit has been found to have a

very high R-factor, and can be used to examine the relative sensitivity of multiple S and Fe isotope systems to the R-factor.

The Voisey's Bay study was funded by Vale, owner of the Voisey's Bay mine, and the Geological Survey of Canada (GSC) Targeted Geoscience Initiative-4 (TGI-4) program. The Voisey's Bay mine offered an opportunity to examine and sample an extensive drill core library and gain access to the open pit mine.

A paper detailing this project has been published in Economic Geology (Hiebert et al., 2013), and Chapter 2 of this thesis contains a modified version of that paper.

1.1.2 Hart Deposit Project Objectives (Chapter 3: Tracing sources of crustal contamination using multiple S and Fe isotopes in the Hart komatiite-associated Ni-Cu-(PGE) sulfide deposit, Abitibi greenstone belt, Ontario, Canada)

The main mineralized zone of the Hart deposit is hosted by the basal komatiite flow in the Shaw Dome within the Abitibi greenstone belt (Figure 3). A second mineralized zone, referred to as the eastern extension is hosted within the second komatiite flow in this succession. Mineralization of the main zone is localized at the base of a wide (>200 m) embayment into its footwall that is interpreted to have been produced by thermomechanical erosion of underlying rocks (Houlé et al., 2010; Houlé and Lesher, 2011). The rocks that underlie the komatiite flows are dominantly composed of felsic to intermediate volcanic and volcaniclastic rocks with a lesser, but regionally extensive, banded iron formation (Houlé et al., 2010), and minor graphitic argillite. In the vicinity of the Hart deposit, the iron formation has been interpreted to represent an exhalite due to the predominance of chert and chert-rich lithologies.

This location was selected for study due to the availability of abundant drill core and cleared trenches through the mineralization resulting from recent exploration activity, and easy access to the site near Timmins, Ontario. Governmental funding through the Geological Survey of Canada (GSC) Targeted Geoscience Initiative-4 (TGI-4) program was also available, as one of the focusses of the TGI-4 funding

was in the Abitibi greenstone belt. This project includes detailed sampling traverses both vertically (from footwall to hangingwall) and laterally through the stratigraphy of the Hart deposit with samples from both drill core and surface trenches taken for petrography, multiple S isotope and Fe isotope analyses, and whole rock geochemical analysis. This sampling strategy allows for creation of a section across the mineralized zones and determines the isotopic variations within the komatiite flows. Researchers (e.g. Lesher and Stone, 1996; Lesher and Keays, 2002; Arndt et al., 2008) have suggested that the komatiite that has crystallized directly above mineralization in komatiite channels is likely to have been emplaced after the mineralization due to continued flow in the channel, and the komatiite material involved in the formation of the sulfide mineralization may only be preserved on the flow flanks. Therefore, sampling laterally into the flanks of komatiite sequences may be critical to trace the isotopic signatures of contamination. Using isotopic data from the mineralization, the footwall lithologies, the komatiite flows directly above mineralization, and the flanks of the komatiite flows, a comparison can be made between the mineralization and the contaminant, and also the mineralization and the unmineralized areas surrounding the mineralization.

The $\delta^{34}S$ values for the Hart mineralization are dominantly within the mantle range, and require the multiple S isotopic method to distinguish between the S source for the mineralization and mantle derived S. Additionally, in the two main zones of mineralization at the Hart deposit, which are hosted by two different komatiite flows, the multiple S and Fe isotope analyses suggest that these zones may not share a common source of contamination. Finally, the sampling strategy was designed to determine whether multiple S and Fe isotopes can be used as a vector towards mineralization.

A paper detailing his project has been published in Mineralium Deposita (Hiebert et al., 2016), and Chapter 3 of this thesis contains a modified version of that paper.

1.1.3 Hart Area Sedimentary Rocks Project Objectives (Chapter 4: Depositional setting of the Late Archean Fe oxide- and sulfide-bearing chert and graphitic argillite in the Shaw Dome, Abitibi greenstone belt, Canada)

The source of magma contamination in both the Voisey's Bay and Hart deposits is considered to be the associated sedimentary rocks (or metasedimentary rocks in the case of the Voisey's Bay deposit). Therefore, identifying the mechanisms for the precipitation or deposition of sulfides in these sedimentary rocks is necessary to fully understand the genetic history of these deposits. Due to the excellent preservation and low grade metamorphism of the sedimentary rocks in the Hart area (Houlé et al., 2010; Lightfoot et al., 2012), the Hart area was selected for this study.

Key objectives are: (1) determine if the environment was anoxic or oxic, (2) establish whether the exhalite was deposited directly from a hydrothermal plume as many have suggested for iron formations (e.g. Isley, 1995), (3) determine the timing of deposition of sulfides, (4) identify the significance of biological activity during sulfide precipitation, (5) ascertain whether the sulfides represent replacement of primary Fe-oxyhydroxides, or are primary precipitates from the water column, and (6) determine if sulfur in the iron formations in the Hart area was derived from the seawater, or from circulating hydrothermal fluids either in subsurface or a hydrothermal plume spreading from volcanic centres.

A paper detailing his project has been published in Precambrian Research (Hiebert et al., 2018), and Chapter 4 of this thesis contains a modified version of that paper.

1.2 References

Arndt N.T., Lesher C.M., Barnes S.J. 2008. Komatiite. Cambridge University Press, New York, 467 p.

Hiebert, R.S., Bekker, A., Wing, B.A., Rouxel, O.J. 2013. The role of paragneiss assimilation in the origin of the Voisey's Bay Ni-Cu sulfide deposit, Labrador: multiple S and Fe isotope evidence. Economic Geology, 108; 1459-1469.

Hiebert, R.S., Bekker, A., Houlé, M.G., Wing, B.A., Rouxel, O.J. 2016. Tracing sources of crustal contamination using multiple S and Fe isotopes in the Hart komatiite-associated Ni-Cu-(PGE) sulphide deposit, Abitibi greenstone belt, Ontario, Canada. Mineralium Deposita, 51; 919-935.

Hiebert, R.S., Bekker., A. Houlé, M.G., Rouxel, O.J. 2018. Depositional setting of the Late Archean Fe oxide- and sulfide-bearing chert and graphitic argillite in the Shaw Dome, Abitibi greenstone belt, Canada. Precambrian Research, 311; 98-116.

Houlé, M.G., Lesher, C.M. 2011. Komatiite-associated Ni-Cu-(PGE) deposits, Abitibi greenstone belt, Superior Province, Canada; *In:* Magmatic Ni-Cu and PGE deposits: geology, geochemistry, and genesis. Society of Economic Geologists, Reviews in Economic Geology, 17; 89-121.

Houlé, M.G., Gibson, H.L., Lesher, C.M., Davis, P.C., Cas, R.A.F., Beresford, S.W., Arndt, N.T. 2008. Komatiitic sills and multigenerational peperite at Dundonald Beach, Abitibi greenstone belt, Ontario: volcanic architecture and nickel sulfide distribution. Economic Geology, 103; 1269-1284.

Houlé, M.G., Lesher, C.M., Préfontaine, S., Ayer, J.A., Berger, B.R., Taranovic, V., Davis, P.C., Atkinson, B. 2010. Stratigraphy and physical volcanology of komatiites and associated Ni-Cu-(PGE) mineralization in the western Abitibi greenstone belt, Timmins area, Ontario: a field trip for the 11th International Platinum Symposium; Ontario Geological Survey, Open File Report 6255, 99p.

Isley, A. 1995. Hydrothermal plumes and the delivery of iron to banded iron formations. Journal of Geology, 103; 169-185.

Lesher, C.M., Stone, W.E. 1996. Exploration geochemistry of komatiites. *In:* Igneous Trace Element Geochemical Applications for Massive Sulfide Exploration. *Edited by:* D.A. Wyman, Geological Association of Canada, Short Course Notes 12, p. 153-204.

Lesher, C.M. and Keays, R.R. 2002. Komatiite-associated Ni-Cu-(PGE) deposits: mineralogy, geochemistry, and genesis; *in* The geology, geochemistry, mineralogy, and mineral beneficiation of the platinum-group elements, Canadian Institute of Mining, Metallurgy and Petroleum, Special Volume 54, p. 579-617.

Lightfoot, P.C., Keays, R.R., Evans-Lamswood, D., Wheeler, R. 2012. S saturation history of Nain Plutonic Suite mafic intrusions: origin of the Voisey's Bay Ni-Cu-Co sulfide deposit, Labrador, Canada. Mineralium Deposita, 47; 23-50.

Naldrett, A.J. 2011. Fundamentals of magmatic sulfide deposits. *In:* Magmatic Ni-Cu and PGE deposits: geology, geochemistry, and genesis. Society of Economic Geologists, Reviews in Economic Geology, 17; 1-50

Ripley, E.M., Park, Y.R., Li, C., and Naldrett, A.J., 1999, Sulfur and oxygen isotopic evidence of country rock contamination in the Voisey's Bay Ni-Cu-Co deposit, Labrador, Canada. Lithos, 47; 53–68.

Ripley, E.M., Li, C., Shin, D. 2002, Paragneiss assimilation in the genesis of magmatic Ni-Cu-Co sulfide mineralization at Voisey's Bay, Labrador; $\delta^{34}S$, $\delta^{13}C$, and Se/S evidence. Economic Geology, 97; 1307-1318.

Ryan, B. 2000, The Nain-Churchill boundary and the Nain Plutonic Suite: A regional perspective on the geologic setting of the Voisey's Bay Ni-Cu-Co deposit. Economic Geology, 95; 703–724.

CHAPTER 2: THE ROLE OF PARAGNEISS ASSIMILATION IN THE ORIGIN OF THE VOISEY'S BAY NI-CU SULFIDE DEPOSIT, LABRADOR: MULTIPLE S AND FE ISOTOPE EVIDENCE

R. Hiebert[1], A. Bekker[1], B.A. Wing[2,3], and O.J. Rouxel[4, 5]

[1]Department of Geological Sciences, University of Manitoba, Winnipeg, MB R3T 2N2, Canada

[2]Department of Earth and Planetary Sciences, McGill University, 3450 University Street, Montreal, Quebec, H3A 2A7 Canada

[3]GEOTOP Research Center, C.P. 8888, Succursale Centre-ville, Montreal, Quebec H3C 3P8, Canada

[4]Institut Universitaire Européen de la Mer, UMR 6538, Université de Bretagne Occidentale, BP 80 F-29280 Plouzané, France

[5]IFREMER, Centre de Brest, Unité Géosciences Marines, 29280 Plouzané, France

This chapter is a modified version of the paper published in Economic Geology as:

Hiebert, R.S., Bekker, A., Wing, B.A., Rouxel, O.J. 2013. The role of paragneiss assimilation in the origin of the Voisey's Bay Ni-Cu sulfide deposit, Labrador: multiple S and Fe isotope evidence. Economic Geology, 108; 1459-1469.

2.1 Abstract

Isotopic and geochemical studies conducted on the Voisey's Bay magmatic Ni-Cu-(PGE) sulfide deposit, Labrador, Canada, suggest crustal contamination of the primary magma as a trigger for sulfur saturation and formation of the deposit. The use of multiple S isotopes has allowed for the identification of a bacterial sulfate reduction biosignature in the Tasiuyak Gneiss in the footwall to the Voisey's Bay deposit. This putative biosignature is preserved in the deposit even at high silicate magma / sulfide melt ratios (R-factor) and links the S present in the Voisey's Bay deposit to the Tasiuyak Gneiss. Iron isotopes in the Voisey's Bay deposit do not preserve this biosignature due to isotopic exchange with large volumes of magma at R-factors > ≈100 that results in isotopic values similar to that of a mantle-derived magma (0.1 ± 0.1‰). S isotope data can be used to model higher R-factors due to the lower concentration of S in the silicate magma, and high concentration of S in the sulfide liquid. A contamination model resulted in a calculated R-factor of 433 ± 177 (1 standard deviation error). The multiple S isotope data are a new tool to directly link S from the deposit to crustal S sources even in deposits with high R-factors where equilibration with a large amount of silicate magma can result in $\delta^{34}S$ values within the mantle range (0 ± 2‰).

2.2 Introduction and Geological Setting

Many studies have been already conducted to understand the geology of the troctolite-type Voisey's Bay magmatic Ni-Cu-(PGE) sulfide deposit and the Nain Plutonic Suite, Labrador, Canada (e.g., Scott, 1998; Evans-Lamswood et al., 2000; Ryan, 2000; Rawlings-Hinchey et al., 2003; and references therein). The Voisey's Bay deposit is hosted by the generally troctolitic Voisey's Bay Intrusion (Figure 2), part of the ca. 1.3 Ga Nain Plutonic Suite, at the boundary between Archean Nain orthogneisses (NGN) of the Nain province, and Proterozoic Tasiuyak paragneisses (TGN) of the Churchill province (Evans-Lamswood et al., 2000; Ryan, 2000;). The Nain and Churchill provinces collided during the 1.85 Ga Torngat orogeny,

resulting in granulite facies regional metamorphism in the area around the Voisey's Bay deposit (Ryan, 2000). At the boundary between the NGN and TGN is an orthopyroxene-bearing granitoid gneiss that represents a metamorphosed igneous intrusion (enderbitic gneisses; EGN), and has been interpreted to be coeval to other similar 1.91 – 1.87 Ga intrusions into the TGN (Ryan, 2000). Although this boundary between Archean orthogneisses and the Proterozoic TGN may not be the actual Nain-Churchill boundary (Ryan 2000), this terminology is well established in previous publications and will be used here.

The Voisey's Bay intrusion consists of two distinct troctolitic bodies and a dyke complex (Evans-Lamswood et al., 2000). Mineralization is present both in the magma conduits feeding the Voisey's Bay Intrusion (Reid Brook deposit and Ovoid) and at the base of the intrusion where magma conduits, represented by troctolite dykes, fed the intrusion (Eastern Deeps). The easternmost magma chamber hosts the Eastern Deeps deposit and outcrops at surface (Figure 2), but the western magma chamber is found at depth below the Reid Brook deposit (Evans-Lamswood et al., 2000). Both magma chambers contain similar rock types, including a gabbroic basal breccia, variably-textured troctolite and normally-textured troctolite (Lightfoot and Naldrett, 1999; Evans-Lamswood et al., 2000). The magma conduit hosting the Ovoid and Eastern Deeps deposits is a subvertical dyke that dips steeply to the south near surface, but rolls over to a northerly dip at depth (Evans-Lamswood et al., 2000). The distribution of deposits in this dyke are controlled by morphologic features of the dyke, such as changes in width and orientation of the dyke, and structural discontinuities such as embayments and fractures/faults in the host rocks (Evans-Lamswood et al., 2000). The Eastern Deeps feeder is a sub-horizontal sill-like feeder to the base of the Eastern Deeps chamber, but might be steeper and joining the dyke that hosts the Ovoid deposit to the north (Lightfoot and Naldrett, 1999). Mineralization in the Voisey's Bay deposits consists of pyrrhotite (75-80% in 100% sulfides) with lesser pentlandite (10-15% in 100% sulfides) and chalcopyrite (5-8% in 100% sulfides) +/- magnetite.

The magmatic conduit system intrudes all three types of gneisses found in the region, and evidence exists for assimilation of multiple types of country rocks during magma ascent and crystallization. In particular, contamination by both the Tasiuyak Gneiss and the Nain Gneiss near the deposits has been proposed as an important factor in producing the mineralization at Voisey's Bay (Lightfoot and Naldrett, 1998; Li et al., 2000). In this study we use multiple S and Fe isotope data to investigate the significance of crustal assimilation in the formation of the Voisey's Bay deposits, with a focus on constraining the specific host-rock contaminants. We present calculations that relate the observed isotopic data to the calculated R-factor for the deposit. Finally, we demonstrate a new technique for using S isotope to identify biological S isotope fractionation signatures in high-grade metamorphic rocks with a sedimentary protolith like the Tasiuyak Gneiss and show how that signature can be preserved in the mineralization in the Voisey's Bay deposit.

2.3 S AND FE STABLE ISOTOPE SYSTEMS

Stable S and Fe isotope ratios are expressed in per mil (‰) using the delta notation, where

$$\delta^{xx}S\ (‰) = \left(\frac{{}^{xx}S/{}^{32}S_{sample}}{{}^{xx}S/{}^{32}S_{standard}} - 1\right) \times 1000 \quad (1)$$

and

$$\delta^{xx}Fe\ (‰) = \left(\frac{{}^{xx}Fe/{}^{54}Fe_{sample}}{{}^{xx}Fe/{}^{54}Fe_{standard}} - 1\right) \times 1000 \quad (2)$$

In the case of S, xx = 33, 34, or 36, and in the case of Fe, xx = 56 or 57. For S isotopes, results are reported on the Vienna-Canõn Diablo Troilite (V-CDT) scale, and for Fe isotopes relative to the international standard IRMM-14 produced as elemental Fe by the Institute for Reference Materials and Measurements. Many authors (e.g. Beard et al., 2003) use the terrestrial igneous rock standard, which has values of δ^{56}Fe=0.09‰ and δ^{57}Fe=0.11‰ relative to IRMM-14 (Beard et al., 2003).

Isotope fractionation depends on the relative mass differences of the different isotopes (Bigeleisen and Mayer, 1947; Urey, 1947). As a result, mass-dependent fractionation (MDF) by both equilibrium and kinetic processes produces characteristic covariations between $\delta^{33}S$ and $\delta^{34}S$ values that follow the approximate relationship $\delta^{33}S \approx 0.515 \times \delta^{34}S$. However, this linear relationship does not exactly describe the actual $\delta^{33}S$- $\delta^{34}S$ patterns because isotopic fractionation is governed by an exponential relationship between isotope ratios, not a linear relationship. To accurately quantify the actual $\delta^{33}S$- $\delta^{34}S$ patterns, S isotope compositions must be converted to quantities with a linear relationship by taking the natural logarithm of the S isotope values, which are defined as follows:

$$\delta^{xx}S^{*}(‰) = 1000 \times \ln\left(1 + \frac{\delta^{xx}S\ (‰)}{1000}\right). \quad (3)$$

Logarithmic values, $\delta^{33}S^{*}$ and $\delta^{34}S^{*}$, allow for a straightforward evaluation of the characteristic fractionation accompanying equilibrium or kinetic processes because a specific process should produce a unique linear slope on a plot of $\delta^{33}S^{*}$ versus $\delta^{34}S^{*}$, referred to as λ. In the case of equilibrium between aqueous and gaseous sulfur species, λ was calculated to be 0.5159 at temperatures consistent with magmatic and hydrothermal environments, but decreases to 0.5149 at low temperatures (e.g., ~20°C; Ono, 2008). However, during kinetic isotope fractionation associated with biological S processing, λ can vary between 0.5077 and 0.5125 for dissimilatory sulfate reduction, a process of anaerobic respiration that produces H_2S, and from 0.5140 to 0.5187 for sulfur disproportionation (Johnston et al., 2005; Johnston, 2011).

The deviation from equilibrium fractionation can also be quantified through $\Delta^{33}S$ values, which represent the difference between observed $\delta^{33}S$ values and $\delta^{33}S$ values expected based on equilibrium fractionation of sulfur with the observed $\delta^{34}S$ values. The $\Delta^{33}S$ values are defined as follows:

$$\Delta^{33}S\ (‰) = \delta^{33}S - 1000 \times \left[\left(1 + \frac{\delta^{34}S}{1000}\right)^{0.515} - 1\right]. \quad (4)$$

The $\Delta^{33}S$ value can shed light on mass-dependent fractionation relationships, since λ values smaller than 0.515 should lead to negative $\Delta^{33}S$ values associated with positive $\delta^{34}S$ values and positive $\Delta^{33}S$ values associated with negative $\delta^{34}S$ values, whereas λ values greater than 0.515 should impart the opposite signature. Additionally, $\Delta^{33}S$ values can also be used to detect extremely small S contributions from Archean sedimentary rocks, as Archean sedimentary rocks are characterized by extremely large $\Delta^{33}S$ values (Johnston, 2011) associated with cycling of S through an anoxic Archean atmosphere followed by incorporation of the atmospherically cycled S into Archean sediments. In magmatic environments, however, fractionation is limited, near 0‰ for both $\delta^{34}S$ and $\Delta^{33}S$ values, between silicate and sulfide liquids and between sulfide minerals (Ohmoto and Rye, 1979; Hubberten, 1980; Bente and Nielsen, 1982; Ohmoto and Lasaga, 1982; Szaran, 1996).

In several types of sedimentary rocks, the $\delta^{56}Fe$ (and $\delta^{57}Fe$) values have been shown to exhibit significant variability (Johnson et al., 2003; Rouxel et al., 2005; Yamaguchi et al., 2005; Archer and Vance, 2006; Dauphas and Rouxel, 2006), and can be used to provide information on the extent of country rock assimilation. However, in igneous rocks, the $\delta^{56}Fe$ (and $\delta^{57}Fe$) values have very limited variability (Beard and Johnson, 2004). An exception to this is when redox reactions control the $\delta^{56}Fe$ variability. Schuessler et al. (2007) determined a fractionation factor of 3.5‰ between pyrrhotite and a peralkaline rhyolite melt at 840°C when Fe^{3+}/Fe^{2+} was approximately 0.62/0.38. In magmas with a higher temperature and higher proportion of Fe^{2+} this fractionation factor is expected to decrease and may approach 0‰ in basalts of MORB composition at >1000°C (Schuessler et al., 2007).

2.4 Analytical Methods

Samples for multiple S and Fe isotope analyses were selected from drill cores provided by Vale Inc. to provide representative samples from the mineralized zones of the Voisey's Bay deposit, the host troctolitic rocks, and the country rocks surrounding the Voisey's Bay deposit (Table 1). Country rocks

were sampled to be representative of possible sulfur sources, and sampled drill holes were located both near the mineralized zones, to provide a representation of the country rock the Voisey's Bay magma intruded into, and far from the mineralized zones, to provide a representation of the country rocks unaffected by the intrusion of the Voisey's Bay magma (Figure 2). Samples of massive sulfide and sulfide grains of sufficient size were microdrilled to generate nearly pure sulfide powder, and samples with finely disseminated sulfide were crushed to generate powder in an agate mill at the Stable Isotopes for Innovative Research (SIFIR) laboratory, University of Manitoba. As pyrrhotite is the dominant sulfide mineral in this deposit, care was taken to only micro-drill pyrrhotite grains. The S from all samples was extracted and converted to Ag_2S through a Cr(II) reduction procedure following Canfield et al. (1986) in the Stable Isotope Laboratory of the Earth and Planetary Sciences Department at the McGill University. Not all samples of EGN and NGN produced sufficient Ag_2S for analysis (>0.0025 wt.%), which is why only one EGN and two NGN samples were analyzed.

The Ag_2S was fluorinated at 225°C in a Ni bomb under ≈20X stoichiometric excess of F_2 for >9 hours. The SF_6 produced was purified cryogenically, using liquid nitrogen traps, and chromatographically, in a gas chromatograph, and then analyzed on a Thermo Electron MAT 253 multi-collector mass-spectrometer for multiple sulfur isotope ratios in a dual-inlet mode. Analyses were done using sample-standard bracketing with 20 seconds of sample gas, followed by 20 seconds of no gas to allow the signal to return to background, then 20 seconds of standard gas, and another 20 seconds of no gas. This cycle was repeated 3 times and the results of the 3 sample runs were averaged to give the reported value. In the mass spectrometer, the SF_6 gas is ionized to SF_5^+, and, as F has only one stable isotope (mass = 19 amu), masses 127, 128, 129 and 131 (corresponding to ^{32}S, ^{33}S, ^{34}S and ^{36}S) were measured simultaneously with no known interferences. The sulfur isotope compositions are reported with respect to the V- CDT scale, on which the $\delta^{34}S$ value of certified standard IAEA-S-1≡ -0.3‰ produced by the International Atomic Energy Agency as Ag_2S, and $\Delta^{33}S$ calculated to be 0.094‰ based on work by Ding et al. (2001).

Table 1: $\delta^{34}S$, $\delta^{33}S$, $\Delta^{33}S$, $\delta^{56}Fe$, and $\delta^{57}Fe$ values, with major and trace element data.

Sample	VB-10-02	VB-10-03	VB-10-04	VB-10-06	VB-10-08	VB-10-09	VB-10-12	VB-10-14	VB-10-16
Litho Grp[1]	MIN	MIN	MIN	TR	MIN	TGN	TGN	TGN	TGN
Drillhole	Ovoid pit	Ovoid pit	Ovoid pit	Ovoid pit	Ovoid pit	VB-99-506	VB-99-506	VB-09-892	VB-09-892
Sample Type	Sulfide	Sulfide	Sulfide	Whole rock	Sulfide	Sulfide	Whole rock	Whole rock	Sulfide
Po/Pn/Cp (%)[2]	75/15/5	90% Cub	75/15/5	15/3/0	53/5/2	5/0/0	2/0/0	2/0/0	2/0/0
$\delta^{33}S$[3]	-0.77	-0.46	-0.36	-0.17	-0.10	-4.46	-4.85	-5.23	-0.99
$\delta^{34}S$[3]	-1.55	-0.92	-0.74	-0.36	-0.22	-8.70	-9.47	-10.27	-1.96
$\Delta^{33}S$[4]	0.02	0.02	0.02	0.01	0.01	0.03	0.04	0.07	0.02
$\delta^{56}Fe$[5]	0.00	0.14	0.14	-0.21		-0.32	-0.46	-0.01	-0.16
$\delta^{57}Fe$[6]	0.02	0.10	0.24	-0.32		-0.66	-0.66	-0.03	-0.24
Fe (wt%)[7]	53.65	46.13	54.54			40.62			42.12
Cu (wt%)[7]	0.65	18.42	1.68			bdl			bdl
Ni (wt%)[7]	4.94	0.37	2.44			0.07			0.10
Al (wt%)[7]	bdl	bdl	0.07			0.88			0.87
Ca (wt%)[7]	bdl	bdl	0.08			2.13			0.23
Na (wt%)[7]	bdl	bdl	bdl			0.14			0.23
Mg (wt%)[7]	bdl	bdl	bdl			1.84			0.34
K (wt%)[7]	bdl	bdl	bdl			bdl			bdl
Ti (wt%)[7]	bdl	bdl	bdl			0.07			0.08
Co (ppm)[8]	1657	48	943			46			197
Cr (ppm)[8]	bdl	bdl	bdl			15			10
Mn (ppm)[8]	866	125	535			341			35
Sr (ppm)[8]	bdl	bdl	bdl			bdl			9
Zn (ppm)[8]	95	1612	86			37			23

Table 1: continued.

Sample	VB-10-18	VB-10-24	VB-10-25	VB-10-27	VB-10-32	VB-10-33	VB-10-34	VB-10-35	VB-10-36
Litho Grp[1]	TGN	MIN	EGN	TR	NGN	PX	NGN	TR	TR
Drillhole	VB-09-892	VB-06-739	VB-09-882	VB-09-882	VB-09-889	VB-99-512	VB-99-512	VB-99-512	VB-99-512
Sample Type	Whole rock	Sulfide	Whole rock	Sulfide	Whole rock	Whole rock	Whole rock	Sulfide	Sulfide
Po/Pn/Cp (%)[2]	2/0/0	45/4/1	0/0/0	28/5/2	0/0/0	0/0/0	0/0/0	24/4/2	5/<1/0
$\delta^{33}S$[3]	-3.67	-1.12		-0.01	0.93		1.98	0.10	0.67
$\delta^{34}S$[3]	-7.15	-2.20		-0.03	1.78		3.81	0.20	1.32
$\Delta^{33}S$[4]	0.02	0.01		0.01	0.02		0.02	0.00	-0.01
$\delta^{56}Fe$[5]	0.12	-0.02	0.05	0.08	0.05	0.24	0.18	0.25	0.41
$\delta^{57}Fe$[6]	0.20	-0.12	0.12	0.05	0.17	0.23	0.21	0.30	0.50
Fe (wt%)[7]		37.73	4.36	39.48	1.46	3.29	1.19	27.63	43.17
Cu (wt%)[7]		0.03	0.01	0.66	bdl	bdl	0.00	0.95	1.22
Ni (wt%)[7]		3.50	0.00	3.01	0.00	0.02	0.00	3.21	4.39
Al (wt%)[7]		2.06	7.97	0.98	10.19	1.17	8.15	0.77	2.92
Ca (wt%)[7]		1.08	3.44	0.53	3.28	16.09	4.86	2.22	1.95
Na (wt%)[7]		0.45	3.47	0.13	4.58	0.18	3.75	0.07	0.62
Mg (wt%)[7]		1.05	1.78	0.53	0.71	12.19	0.83	12.69	2.37
K (wt%)[7]		bdl	0.07	bdl	bdl	bdl	bdl	bdl	bdl
Ti (wt%)[7]		0.06	0.61	bdl	0.18	0.10	0.10	0.11	0.77
Co (ppm)[8]		1110	17	1213	bdl	34	10	968	1237
Cr (ppm)[8]		95	45	bdl	20	401	8	3151	72
Mn (ppm)[8]		371	679	28	135	817	160	942	347
Sr (ppm)[8]		85	966	20	669	142	1397	16	134
Zn (ppm)[8]		8	74	82	24	26	18	110	70

Table 1: continued.

Sample	VB-10-37	VB-10-38	VB-10-40	VB-10-42	VB-10-44	VB-10-47	VB-10-49	VB-10-51	VB-10-52
Litho Grp[1]	MIN	MIN	MIN	MIN	MIN	TR	TR	TGN	TGN
Drillhole	VB-00-534A	VB-00-534A	VB-00-534	VB-08-871	VB-08-871	VB-95-171	VB-95-171	VB-06-745	VB-06-745
Sample Type	Sulfide	Sulfide	Sulfide	Sulfide	Sulfide	Sulfide	Whole rock	Whole rock	Whole rock
Po/Pn/Cp (%)[2]	44/4/2	72/6/2	25/3.5/1.5	70/10/10	55/4/1	15/2/1	5/tr/0	2/0/0	2/0/0
$\delta^{33}S$[3]	-0.47	-0.35	-0.23	0.09	-0.24	0.02	1.77		-2.52
$\delta^{34}S$[3]	-0.92	-0.65	-0.44	0.20	-0.45	0.06	3.46		-4.93
$\Delta^{33}S$[4]	0.01	-0.02	0.00	-0.01	-0.01	-0.01	-0.01		0.02
$\delta^{56}Fe$[5]	0.01	-0.01		0.14	0.09	0.03	0.18	0.12	0.22
$\delta^{57}Fe$[6]	-0.01	-0.07		0.15	0.10	-0.22	0.32	0.12	0.12
Fe (wt%)[7]	38.62	50.86		45.40	41.21	37.65	5.54	7.82	11.88
Cu (wt%)[7]	0.39	0.67		7.97	0.72	1.04	0.00	0.03	0.08
Ni (wt%)[7]	4.15	2.88		1.63	3.12	6.28	0.03	0.02	0.02
Al (wt%)[7]	0.84	1.61		bdl	1.59	1.77	10.65	7.69	5.67
Ca (wt%)[7]	0.57	0.67		0.05	0.98	1.41	7.11	0.91	1.42
Na (wt%)[7]	0.19	0.43		bdl	0.33	0.32	1.82	1.79	1.54
Mg (wt%)[7]	0.46	0.58		bdl	1.06	6.83	5.11	1.93	1.57
K (wt%)[7]	bdl	bdl		bdl	bdl	bdl	bdl	bdl	bdl
Ti (wt%)[7]	0.43	0.22		bdl	0.35	0.13	0.75	0.35	0.41
Co (ppm)[8]	885	1621		703	1810	1927	49	32	50
Cr (ppm)[8]	425	39		65	37	171	112	145	126
Mn (ppm)[8]	399	109		29	584	669	620	323	804
Sr (ppm)[8]	44	117		bdl	60	51	635	173	191
Zn (ppm)[8]	70	54		205	145	91	37	117	131

Notes: bdl = below detection limits, [1]MIN = mineralized zones, TR = troctolite, TGN = Tasiuyak Gneiss, EGN = Enderbitic Gneiss, NGN = Nain Gneiss; [2]Po = pyrrhotite, Pn = pentlandite, Cp = chalcopyrite, Cub = cubanite; [3]2σ error < 0.25‰; [4]2σ error < 0.01‰; [5]2σ error = 0.08‰ [6]2σ error = 0.11‰; [7]detection limit = 0.05 %; [8]detection limit = 5 ppm

Repeated analysis of internal reference materials return 2σ uncertainties on $\delta^{34}S$ and $\Delta^{33}S$ values that are <0.25 and <0.01‰, respectively.

Aliquots for Fe isotope analysis and major and trace element analysis were prepared from the remaining material following S isotope analysis by crushing the whole rock sample in an agate mortar. The crushed sample was then completely dissolved in a trace-metal grade HNO_3-HCl acid mixture and evaporated to dryness on a hot plate at 60°C. Complete dissociation and oxidation of Fe was achieved by dissolving this residue in aqua regia and evaporating to dryness on a hot plate again. The dry residue was dissolved in 6N HCl in a heated vessel (40°C), which was agitated by ultrasonication. Major and trace element concentrations were measured by ICP-AES at Pole Spectrometrie Ocean (PSO), IFREMER in Brest on the splits of the derived solutions, which were also used for Fe isotope analysis (Table 1). The detection limit for these analyses is 0.05 weight % and 5 ppm, for major and trace elements respectively. The split of the solution used for Fe isotope analysis was then centrifuged to separate, and remove, any C-rich material. Fe was extracted from a volume of solution corresponding to 2500 µg of Fe by Bio-Rad AG-1X8 anion resin, which adsorbs ferric iron to the surface of the resin, in a column. The matrix was then dissolved, and other ions striped from the resin, by passing 20 mL of 6N HCl through the column. Iron was then eluted in a 20 mL bath of 0.12N HCl. This solution was evaporated to dryness and the residue was dissolved with 1% HNO_3 to obtain 5 mL of 500 ppm Fe in solution. Elemental Fe reference materials, such as IRMM-14, were also dissolved with 1% HNO_3 to obtain 5 mL of 500 ppm Fe in solution. Isotopic ratios ($\delta^{56}Fe$ and $\delta^{57}Fe$) were determined with a Thermo Electron Neptune multi-collector inductively-coupled mass-spectrometer (MC-ICP-MS) at PSO in medium-resolution mode, which allows distinction between possible interferences of ArO on ^{56}Fe, ArOH or ^{57}Fe, and ArN on ^{54}Fe (Rouxel et al., 2005). Instrumental bias was corrected using simultaneous measurement of Ni isotopes (^{60}Ni and ^{62}Ni) from an internal standard solution that was introduced into the plasma with the sample. “Sample-standard” bracketing was also used to correct for instrumental mass discrimination and instrumental drift by

normalizing the sample to the average value for the standard measured before and after the sample. As the "sample-standard" correction method is prone to matrix effects, the combination of both measurement of Ni isotopes and the "sample-standard" bracketing corrects for this and provides accurate and precise results. Based on duplicated chemical purification and analysis of IRMM-14 and an internal reference standard periodically over the life of the lab, the external reproducibility is 0.08‰ for δ^{56}Fe and 0.11‰ for δ^{57}Fe values (2σ). Iron isotope values are reported relative to the standard IRMM-14, using the conventional delta notation (Table 1).

2.5 Results

2.5.1 Major and trace element data

Major (Fe, Al, Ca, Na, Mg, K, Ti, and Mn) and trace (Cu, Ni, Co, Cr, Sr, and Zn) element data were used to characterise samples and assess the purity of the sampled sulfide before isotopic work (Table 1). Several samples that were micro-drilled to obtain a "pure sulfide" powder still contained significant concentrations (>1 wt.%) of Al, Ca, and Mg, which indicates that silicate minerals are present in the massive sulfide as very fine disseminated grains or inclusions.

2.5.2 δ^{34}S, δ^{33}S, and Δ^{33}S values of Sulfide Mineralization and Voisey's Bay Troctolite

The δ^{34}S values observed in this study from barren troctolite and mineralized zones are near the mantle range, similar to the δ^{34}S values obtained by Ripley et al. (1999) from the Voisey's Bay mineralized zones. Sulfides in the barren troctolite and mineralized zones have δ^{34}S values ranging from -0.4 to +3.5 and -2.2 to +0.2‰, respectively (Table 1; Figure 4). The δ^{34}S values from the mineralized samples show a general trend of becoming more positive from the Reid Brook zone through the Discovery Hill zone and the Ovoid zone to the Eastern Deeps zone, as was also observed by Ripley et al. (1999). Sulfur isotope data show little variation in Δ^{33}S, with values ranging between -0.02 and +0.03‰.

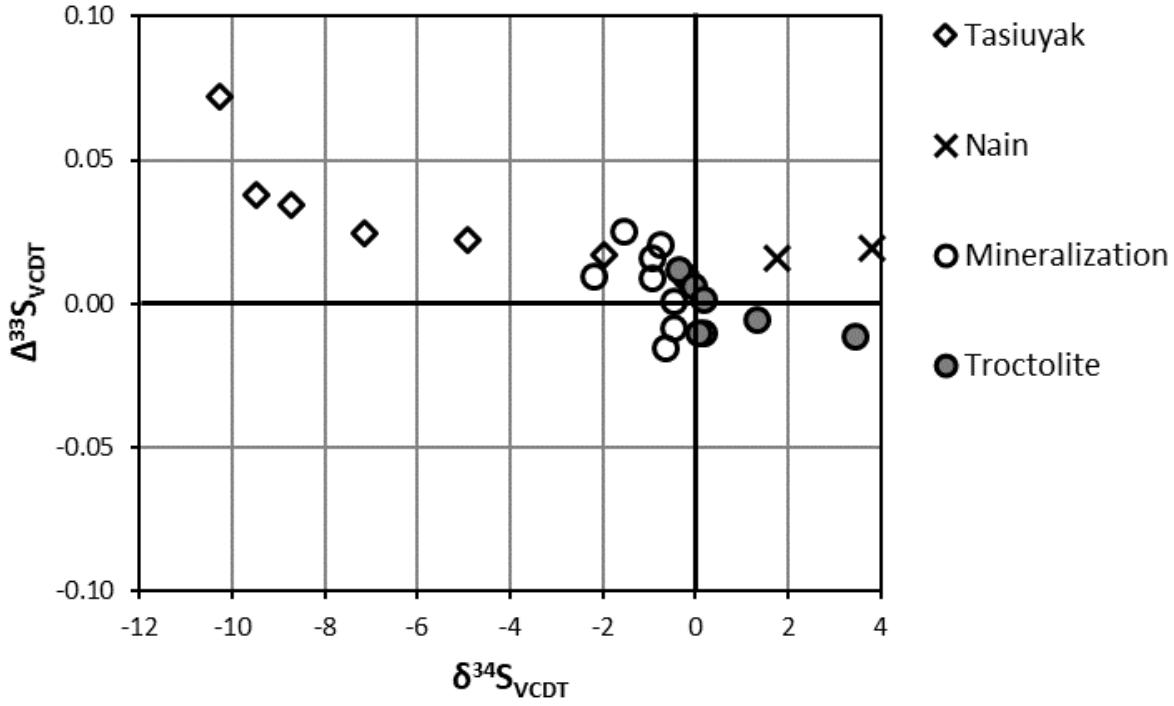

Figure 4: $\delta^{34}S$ vs. $\Delta^{33}S$ data for the Tasiuyak Gneiss, Nain Gneiss, mineralization, and troctolite.

2.5.3 $\delta^{34}S$, $\delta^{33}S$, AND $\Delta^{33}S$ VALUES OF TASIUYAK AND NAIN GNEISSES

The $\delta^{34}S$ values of Tasiuyak Gneiss observed in this study vary from -10.3 to -2.0‰, with an average value of -7.1‰ (Table 1; Figure 4). This data does not show as much variation as the -17.3 to +18‰ range reported by Ripley et al. (2002). Ripley et al. (2002) attributed this large range to bacterial sulfate reduction. As with the mineralization and troctolite samples, sulfur isotope values have little variation in $\Delta^{33}S$, with values ranging between +0.02 and +0.07‰. The Nain Gneiss has notably positive $\delta^{34}S$ values that are +1.8 and +3.8‰ from the two samples that had sufficient S for analysis. Associated $\Delta^{33}S$ values are both 0.02‰.

2.5.4 δ^{56}FE VALUES

Values of δ^{56}Fe for mineralized samples vary from -0.02 to +0.14‰ (Table 1; Figure 5), and troctolite samples vary from -0.21 to +0.41‰. Although these ranges overlap, samples from the mineralization show a much smaller range centered on the mantle range in comparison with those associated with troctolites (Beard and Johnson, 2004; Poitrasson et al., 2004).

The Nain and Enderbite gneisses are characterized by a narrow positive range of δ^{56}Fe values; +0.05 to +0.24‰ for the Nain gneiss and +0.05‰ for the single Enderbite gneiss sample. The Tasiuyak gneiss, however, has a wider range of δ^{56}Fe values than the other gneisses, and has predominantly negative δ^{56}Fe values, from -0.46 to +0.22‰.

2.6 DISCUSSION

2.6.1 $\delta^{34}S$ VALUES OF SULFIDE MINERALIZATION AND TASIUYAK GNEISS:

In sulfide mineralization from the Voisey's Bay deposit, Ripley et al. (1999) found a range of $\delta^{34}S$ values from -4.1 to +1.8‰. They also observed a change from negative values for the Reid Brook zone (-4.1 to -1.1‰) to slightly positive values in the Eastern Deeps (-2.4 to +1.8‰) with the Ovoid and Discovery Hill

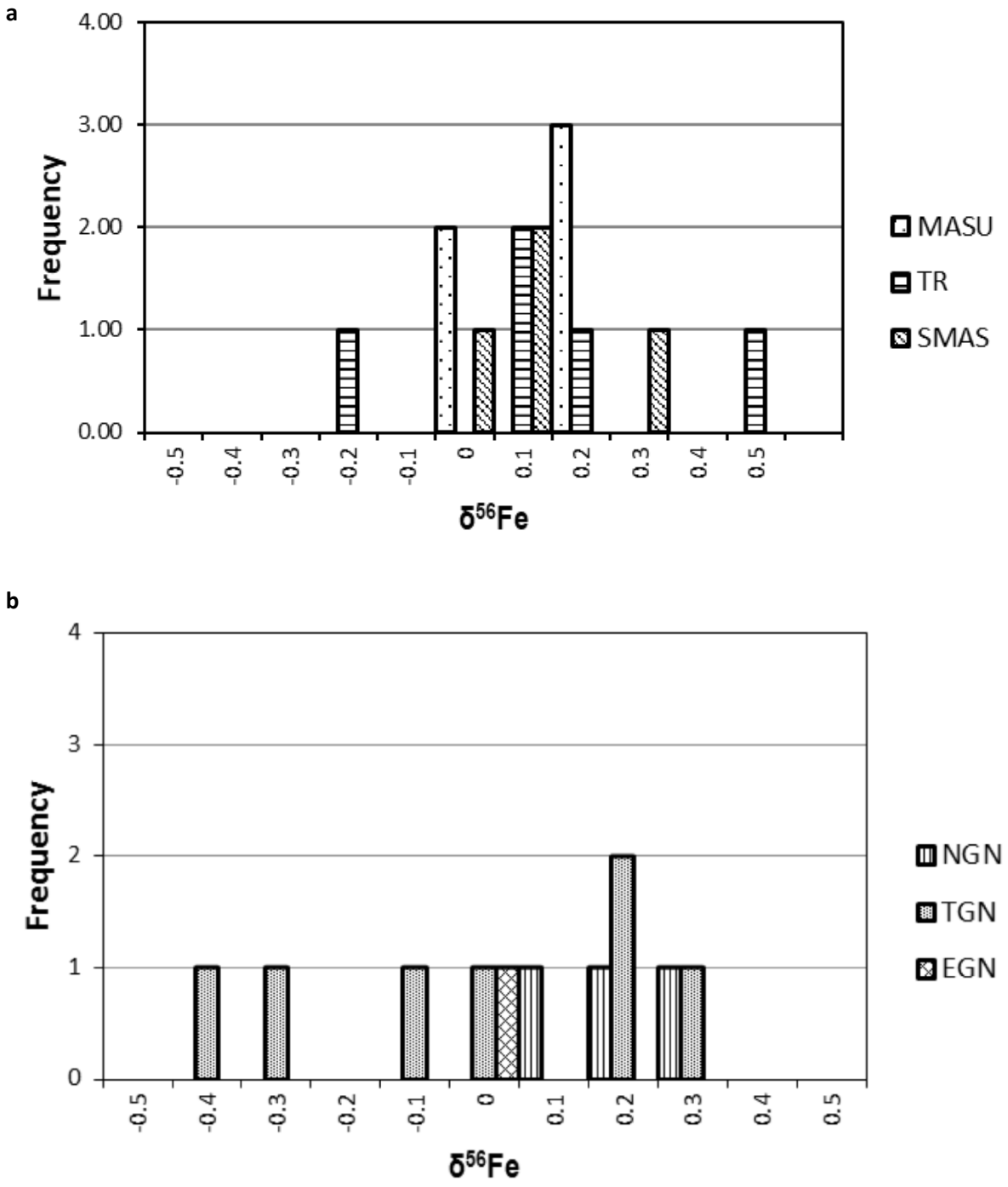

Figure 5: Histograms showing δ^{56}Fe values for (a) massive sulfide (>75% sulfide; MASU), semi-massive sulfide (25-75% sulfide; SMAS) and troctolitic rocks (<25% sulfide; TR), and (b) country rocks: Nain Gneiss (NGN), Tasiuyak Gneiss (TGN), and enderbite gneiss (EGN).

zones having intermediate ranges (Figure 2). Except for some Reid Brook samples, the observed $\delta^{34}S$ values for mineralization do not fall outside the mantle range of 0 ± 2‰ (Chaussidon et al., 1989).

As these values are similar to mantle values, linking the sulfur isotope values of the mineralization to those of the country rocks has been problematic. Ripley et al. (1999) showed that there is limited direct evidence linking the contaminant source to the sulfide deposits except for the Reid Brook deposit, in which $\delta^{34}S$ values of the mineralization are similar to those of the Tasiuyak gneiss. Subsequently, Ripley et al. (2002) published new data with a wider range of $\delta^{34}S$ values for the Tasiuyak gneisses (-17 to +18.3‰) with an average near 0‰ similar to $\delta^{34}S$ values of mineralization. Ripley et al. (2002) interpreted the sulfur isotope composition of the mineralization to be a result of assimilation of Tasiuyak gneiss with a wide range of $\delta^{34}S$ values, followed by mixing and isotopic exchange of sulfur to produce the observed range of $\delta^{34}S$ values in the mineralization. However, this interpretation is not unique and does not rule out other scenarios for the formation of mineralization with near-zero $\delta^{34}S$ values. In addition, high-temperature equilibrium isotope fractionations found in magmatic S can be distinguished from low-temperature kinetic isotope fractionations found in sedimentary S through multiple S isotope analyses, potentially allowing identification of the dominant fractionation process for S isotopes in this deposit.

2.6.2 Application of multiple sulfur isotopes to magmatic systems

The assimilation of country rock is thought to be a significant contributor to sulfur saturation in mafic to ultramafic magmas (e.g., Lesher and Groves, 1986; Keays and Lightfoot, 2010; Bekker et al., 2009). Several isotopic studies have been performed to determine the source of contamination responsible for sulfur saturation in the Voisey's Bay intrusion. These studies explored Sm-Nd, U-Pb, Re-Os, and Rb-Sr radiogenic isotope systematics (Amelin et al., 2000; Lambert et al., 2000), and oxygen and sulfur isotopes (Ripley et al., 1999, 2000, 2002). Additionally, major and trace element geochemistry was utilized by Li et al. (2000) to show that at least two different types of country rocks were assimilated

during the rise of the magma through the crust, one being an unknown mid-crustal felsic gneiss and the other the Proterozoic Tasiuyak gneiss.

Multiple sulfur isotope data can help to distinguish between mantle- and crust-derived sulfur when magmatic sulfide $\delta^{34}S$ values are similar to the mantle range of values, as is the case at Voisey's Bay. Mass-dependent fractionation can lead to slight deviation from equilibrium fractionation in terms of relative ^{33}S-^{32}S and ^{34}S-^{32}S variations (Johnston et al., 2005, 2007). In systems that do not show significant mass-independent fractionation, such as the Voisey's Bay mineralization, logarithmic $\delta^{33}S^*$ and $\delta^{34}S^*$ axes (see S and Fe stable isotope systems section above and figure caption for Figure 6 for explanation of these notations) give information about the processes responsible for fractionation of sulfur, and, as described here, can be also used to understand ore genesis. Equilibrium fractionation, as is expected for all high-temperature magmatic processes such as fractional crystallization, should result in a linear trend that follows a slope of 0.5159 on a plot of $\delta^{33}S^*$ vs. $\delta^{34}S^*$ (Ono, 2008). However, as discussed earlier, mass-dependent kinetic processes such as diffusion or biologically-mediated reactions (e.g. bacterial sulfate reduction), will result in a slightly different slope from that of equilibrium processes, and can potentially be used to identify the dominant process that fractionated S in the contaminant rock. High-temperature, magmatic S isotope fractionations are small (e.g., Ohmoto and Goldhaber, 1997), and do not significantly change S isotope values of sulfides. As a result, the relationship between $\delta^{33}S^*$ and $\delta^{34}S^*$ values in the contaminant lithology should be preserved in the mineralization produced by assimilation.

However, mixing of two S reservoirs that each have the same relationship between $\delta^{33}S^*$ and $\delta^{34}S^*$, will produce non-zero intercepts on a $\Delta^{33}S$- $\delta^{34}S$ plot. This non-zero intercept is produced because fractionation among isotope pairs is governed by exponential relationships while mixing required for homogenization is governed by linear relationships (Farquhar and Wing, 2003). Larger initial differences in the isotopic composition of the mixing end-members creates larger magnitude non-zero intercepts

a

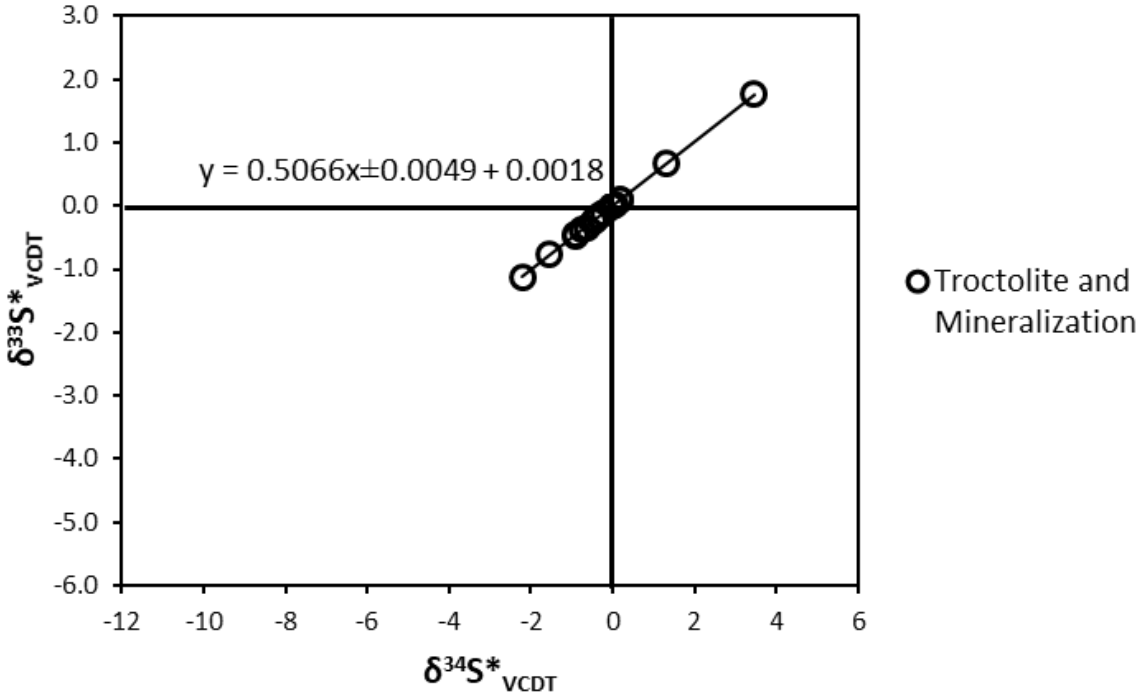
y = 0.5066x±0.0049 + 0.0018
δ33S*VCDT
δ34S*VCDT
Troctolite and Mineralization

b

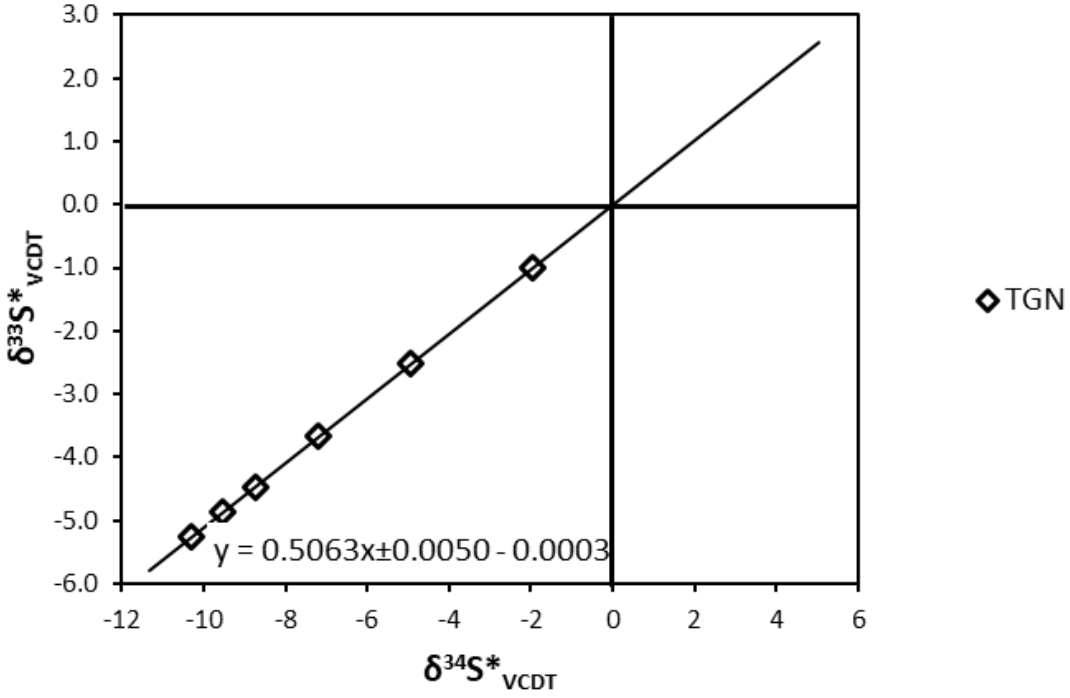
y = 0.5063x±0.0050 - 0.0003
δ33S*VCDT
δ34S*VCDT
TGN

c

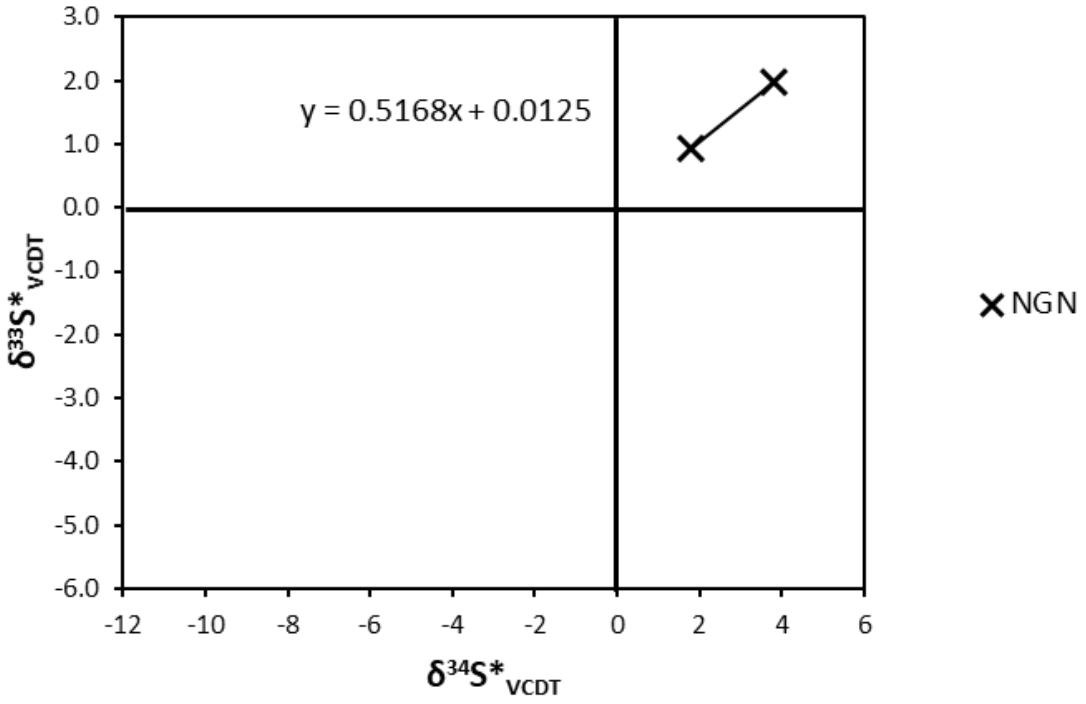

Figure 6: $\delta^{33}S^*$ vs. $\delta^{34}S^*$ data for the Voisey's Bay troctolite and mineralization (a), Tasuiyak Gneiss (b), and Nain Gneiss (c). Equations for the trend lines are presented as y = mx±n + b, where y=$\delta^{33}S^*$, x=$\delta^{34}S^*$, m=slope of the line, n=uncertainty of the slope, and b=y intercept value. Note that the natural logarithmic expression for delta notations was used on this figure to compensate for non-linear behavior of traditional delta notations. $\delta^{33}S$ and $\delta^{34}S$ values are conventional δ notations with respect to VCDT (Vienna–Canyon Diablo Troilite) defined as $\delta^{x}S = 1000[(^{x}S/^{32}S)_{sample}/(^{x}S/^{32}S)_{VCDT} - 1]$, where ^{x} is 33 and 34, respectively. $\delta^{33}S^*$ and $\delta^{34}S^*$ values are defined as $\delta^{xx}S^* = 1000\ln[(\delta^{x}S/1{,}000) + 1]$, where ^{x} is 33 and 34, respectively.

(either positive or negative), although the intercept may approach zero in a situation where a small amount of S from one reservoir is diluted by an extremely large amount of S from a second (e.g. resetting S isotope values of a sulfide liquid to uniform near-mantle composition through interaction with a large amount of silicate melt). Thus, these two different isotopic representations for a magmatic sulfide deposit can be useful for understanding the processes involved in mineralization as well as for characterization of the contaminant lithology. The slope on a $\delta^{33}S^*$ vs. $\delta^{34}S^*$ graph can be used to link the mineralization and the contaminant because the slope will be the same for both, while non-zero intercepts on a $\Delta^{33}S$ vs. $\delta^{34}S$ graph can reveal the influence of mixing processes because mixing will produce a non-zero intercept.

The $\Delta^{33}S$ vs. $\delta^{34}S$ plots for the sulfide mineralization and troctolite at Voisey's Bay show a distinct negative trend that passes through the origin (Figure 4). The non-zero slope indicates that the λ value for the mineralization is not 0.515, implying that something other than high-temperature equilibrium influenced the sulfur isotope compositions.

We applied a Monte Carlo simulation to the measured sulfur isotope data to estimate the influence of the measurement error when calculating the trend of the data on the $\delta^{33}S^*$ vs. $\delta^{34}S^*$ graph. The slope of the trend in the data was calculated using a bootstrap method in which "synthetic" datasets of the same size as the original dataset were created by randomly sampling the original dataset. For each sample, 50 values were randomly generated to produce a dataset with a normal distribution around the measured value for $\delta^{33}S$ and $\delta^{34}S$, with one standard deviation of these randomly generated values equal to the 1σ measurement error. The average of these 50 randomly generated values was used to produce synthetic $\delta^{33}S^*$ and $\delta^{34}S^*$ values to calculate the slope. The slope was calculated by ordinary least squares regression. To compensate for the assumption of no error in y-axis values in the ordinary least squares regression, slopes were calculated twice for each dataset using $\delta^{34}S^*$ on the y-axis and $\delta^{33}S^*$ on the x-

axis for one calculation, and reversing the axes for the second. This process was repeated 1000 times in Microsoft Excel to produce a statistically significant average slope value with associated error.

The data for the Tasiuyak Gneiss forms a trend with the slope of 0.5066 ± 0.0049 (1σ error), which is identical within error to that expected for sulfur processed by bacterial sulfate reduction when the overall ^{34}S-^{32}S fractionation is small (Farquhar et al., 2003; Ono et al., 2006; Johnston et al., 2005, 2007). Bacterial sulfate reduction is a common process in marine and terrestrial aqueous environments, it is therefore not surprising to find evidence for influence of this process on the sedimentary protolith to the Proterozoic Tasiuyak Gneiss (Canfield, 2001). The data from the Voisey's Bay mineralization and troctolite forms a trend with the slope of 0.5063 ± 0.0050 (1σ error), which is identical within errors to that of the Tasiuyak Gneiss (Figure 6). Thus, it is likely that sulfur derived from the Tasiuyak Gneiss was incorporated into the sulfide mineralization present at the Voisey's Bay deposit. The steeper slope, admittedly based on only 2 data points, from the Nain Gneiss (0.5168; Figure 5) is close to that associated with high-temperature equilibrium fractionation. As there are only 2 data points, no error could be calculated and this slope is considered to be poorly constrained, however, the calculated slope is consistent with previous interpretations that little or no S from the Nain Gneiss involved in the mineralization process (e.g. Lightfoot et al., 2012).

2.6.3 R-Factor Considerations

As the observed $\delta^{34}S$ values from the Voisey's Bay troctolite and mineralization are near mantle values, it is difficult to distinguish mantle and crustal sulfur sources based on these values alone. However, as has been shown previously (e.g., Lesher and Burham, 2001; Ripley and Li, 2003), mantle or near-to-mantle isotopic and concentration ratios can be produced through interaction between sulfide melt and the large amounts of the host magma. The degree of interaction between sulfide melt and the host magma can be quantified with the R-factor, which is the silicate to sulfide mass ratio (Campbell and Naldrett, 1979). Previous estimates of the R-factor in the Voisey's Bay deposit that have been based on

different elemental and isotopic proxies are presented in Table 2 (e.g., Naldrett et al., 2001; Lambert et al., 1999, 2000; Lightfoot et al., 2012).

Calculation of the R-factor required to produce the observed $\delta^{34}S$ and $\delta^{56}Fe$ values was done using the formula derived by Lesher and Burnham (2001) for isotopic mixing:

$$\delta_M = \frac{\delta_A X_A \frac{R}{1+R} + \delta_B X_B \frac{1}{1+R}}{X_A \frac{R}{1+R} + X_B \frac{1}{1+R}} \quad (5)$$

where X is the initial concentration of S or Fe in the silicate magma (A) or sulfide melt (B), and δ is the $\delta^{34}S$ or $\delta^{56}Fe$ value for the initial isotopic composition of the magma (A), sulfide liquid (B), or the resulting sulfide mineralization (M). Input parameters for models presented here are shown in Table 3. Ripley and Li (2003) point out that isotope exchange, which is a different process, can be modelled using a slightly different equation:

$$\delta_M = \frac{\delta_B + \frac{X_B}{X_A} R(\delta_A + \Delta)}{1 + \frac{X_B}{X_A} R} \quad (6)$$

Where Δ is the isotopic difference between sulfur in the sulfide liquid and the silicate melt in equilibrium. However, for our data, this equation yields an essentially identical result for R of 442.

As indicated in equations 5 and 6, initial S or Fe concentrations and isotopic compositions for magma and sulfide are required for R factor calculation. Based on the PGE-depleted nature of Voisey's Bay sulfides, Naldrett (2010) concluded that the Voisey's Bay magma reached sulfur saturation prior to emplacement as a result of earlier contamination, becoming unsaturated again as it rose through the crust. Using difference in PGE concentrations in disseminated and massive sulfides, and the generally PGE-depleted nature of all Nain Plutonic Suite rocks, Lightfoot et al. (2012) interpreted that, although prior contamination could have occurred, sulfur saturation was not necessary to produce the observed variability in PGE concentrations. In either case, sulfur concentration in the initial Voisey's Bay magma

Table 2: Calculated R-factors for the Voisey's Bay deposit.

R-Factor	Derived Using:	Reference
280 – 1000	Ni, Cu, PGE	Naldrett et al., 2000
200 – 1000	Re-Os	Lambert et al., 1999
50 – 500	Re – Os (uncontaminated magma)	Lambert et al., 2000
400 - >5000	Re – Os (previously contaminated magma)	Lambert et al., 2000
439	Ni	Lightfoot et al., 2012
433 ± 177	$\delta^{34}S$	This study

Table 3: R-factor model parameters.

	Initial $\delta^{34}S_A$ (‰)[1]	**X_A (wt.%)[2]**	**Initial $\delta^{34}S_B$ (‰)[3]**	**X_B (wt.%)[4]**	**Final $\delta^{34}S_M$ (‰)**	**Calculated R value[8]**
$\delta^{34}S$	1.0	0.25	-5.2 (7.4)	38	-1.3 (1.0)	433±177
	Initial $\delta^{56}Fe_A$ (‰)[5]	**X_A (wt.%)[6]**	**Initial $\delta^{56}Fe_B$ (‰)[7]**	**X_B (wt.%)[4]**		
$\delta^{56}Fe$ model 1	0.09	7.2	-0.22	62		
$\delta^{56}Fe$ model 2	0.09	9.3	-0.22	62		
$\delta^{56}Fe$ model 3	0.09	9.7	-0.22	62		

Notes:

1. Estimate of initial $\delta^{34}S_A$ based on Ripley et al. (1999).
2. Estimate of X_A for sulfur discussed in text.
3. Estimate of $\delta^{34}S_B$ based on the average of $\delta^{34}S$ values for TGN with >0.5 wt.% S from Ripley et al. (1999, 2002) and our study. Standard deviation is in parentheses.
4. Estimate of X_B based on approximate sulfide liquid composition of FeS.
5. Estimate of initial $\delta^{56}Fe_A$ based on the average value for terrestrial igneous rocks (Beard et al., 2003).
6. Estimates of X_A for Fe are intended to cover the full range of possible primary magma compositions from high Al-basalt to tholeiitic basalt.
7. Estimate of $\delta^{56}Fe_B$ based on the average of $\delta^{56}Fe$ values for TGN from our study.
8. Average and 1σ error based on Monte Carlo simulation of 1000 values, see text for discussion.

would be near saturation, which has been modelled to be ≈2750 ppm by Naldrett (2010). Accordingly, we selected a value of 2500 ppm that is near, but slightly below, sulfur saturation as the initial sulfur concentration in our modelling to reflect this possible earlier contamination. Earlier contamination would also impact the S isotope ratio of the initial magma, and Ripley et al. (1999) used an initial $\delta^{34}S$ value of +1‰ for the contaminated Voisey's Bay magma. To be consistent with previously reported results, we adopted this value of +1‰ for our modelling.

Data from Ripley et al. (1999; 2002) was used in addition to our data to estimate the initial $\delta^{34}S$ value for the TGN to account for the large range in $\delta^{34}S$ values in these data sets that are not observed in our data. The average of data from Ripley et al. (1999; 2002) and this study, has a value of -2.0‰. However, Lightfoot et al. (2012) interpreted that the assimilation of a sulfide-rich layer of the TGN was most critical for the Voisey's Bay magma to reach sulfur saturation. The $\delta^{34}S$ data for the TGN samples with relatively high S concentrations tend to be more negative (Ripley et al., 1999; 2002; this study). For example, if a cut-off of >0.25 wt.% S would be applied to the $\delta^{34}S$ data, the average $\delta^{34}S$ value would become -3.8‰, with a >0.5 wt.% S cut-off, the average $\delta^{34}S$ value would shift to -5.2‰, and with a >1.0 wt.% S cut-off, the average $\delta^{34}S$ value would be -5.9‰. For our modelling, a cut-off of 0.5 wt.% S was used, giving an initial sulfide $\delta^{34}S$ value of -5.2‰ to represent this high-sulfide layer of the TGN.

Due to uncertainty in the initial S concentration of the magma, and variability in the $\delta^{34}S$ values of the mineralization in the Voisey's Bay intrusion, only an estimate of the range of R-factor values can be obtained. To assess the accuracy of this estimate, a Monte Carlo simulation was done by generating random values with a normal distribution around the mean and with the same standard deviation as the measured data for sulfide mineralization (δ_M) and Tasiuyak Gneiss sulfide with >0.5 wt.% S (δ_B). The results of the Monte Carlo simulation were used to calculate the R-factor using equation 6. This process was repeated 1000 times. The 1000 calculated R-factor values were then divided into groups of 50, taking an average of the 50 calculated R-factor values. These 20 average values were then used to

calculate the reported R-factor and error for the R-factor of 433±177 (1σ standard error) to achieve the average $\delta^{34}S$ value of the mineralization (Figure 7). This value is nearly identical to previous estimates (Naldrett et al., 2000; Lambert et al., 1999, 2000; Lightfoot et al., 2012).

Due to the higher concentration of Fe in the magma (Table 3), the signature of crustal contamination is essentially eliminated at an R-factor higher than 150 (Figure 8), and our data indicates that the sulfide melt and silicate magma were essentially in equilibrium as far as their Fe isotope compositions are concerned. Additionally, Fe isotopes have been shown to be fractionated in magmatic systems through crystallization of olivine (Teng et al., 2008; Weyer, 2008), as such, the observed Fe isotopic variation in the Voisey's Bay troctolite and mineralization could be the result of such magmatic fractionation and do not provide unequivocal evidence about contamination processes.

2.6.3.1 Theoretical Effect of R-Factor on $\delta^{33}S$-$\delta^{34}S$ Relationships:

The surprising preservation of the relationship expected for sulfur processed by bacterial sulfate reduction in the mineralized rocks of Voisey's Bay intrusion led us to investigate its sensitivity to equilibrium isotope exchange between sulfide and silicate melts. We used the formula (6) described previously, with theoretical values for $\delta^{33}S$, $\delta^{34}S$, and $\Delta^{33}S$ of -2.553, -5.000, and +0.025 respectively, as the initial composition, corresponding to λ=0.510 for this theoretical test.-. We assumed a theoretical magma characterized by 0‰ for $\delta^{33}S$, $\delta^{34}S$, and $\Delta^{33}S$ values. For the analytical precision reported here, the $\delta^{33}S^*$ and $\delta^{34}S^*$ values maintain the original relationships in both a $\Delta^{33}S$-$\delta^{34}S$ plot and a $\delta^{33}S^*$-$\delta^{34}S^*$ plot (Figure 9) up to R-factors >700.

2.7 Conclusions

Multiple S isotopic data can be used to identify crustal sources of S in magmatic sulfide deposits of any age. The S in the TGN was originally fractionated through bacterial sulfate reduction at the depositional site of its sedimentary protolith. This process is recorded by the relationship between $\delta^{33}S^*$ and $\delta^{34}S^*$,

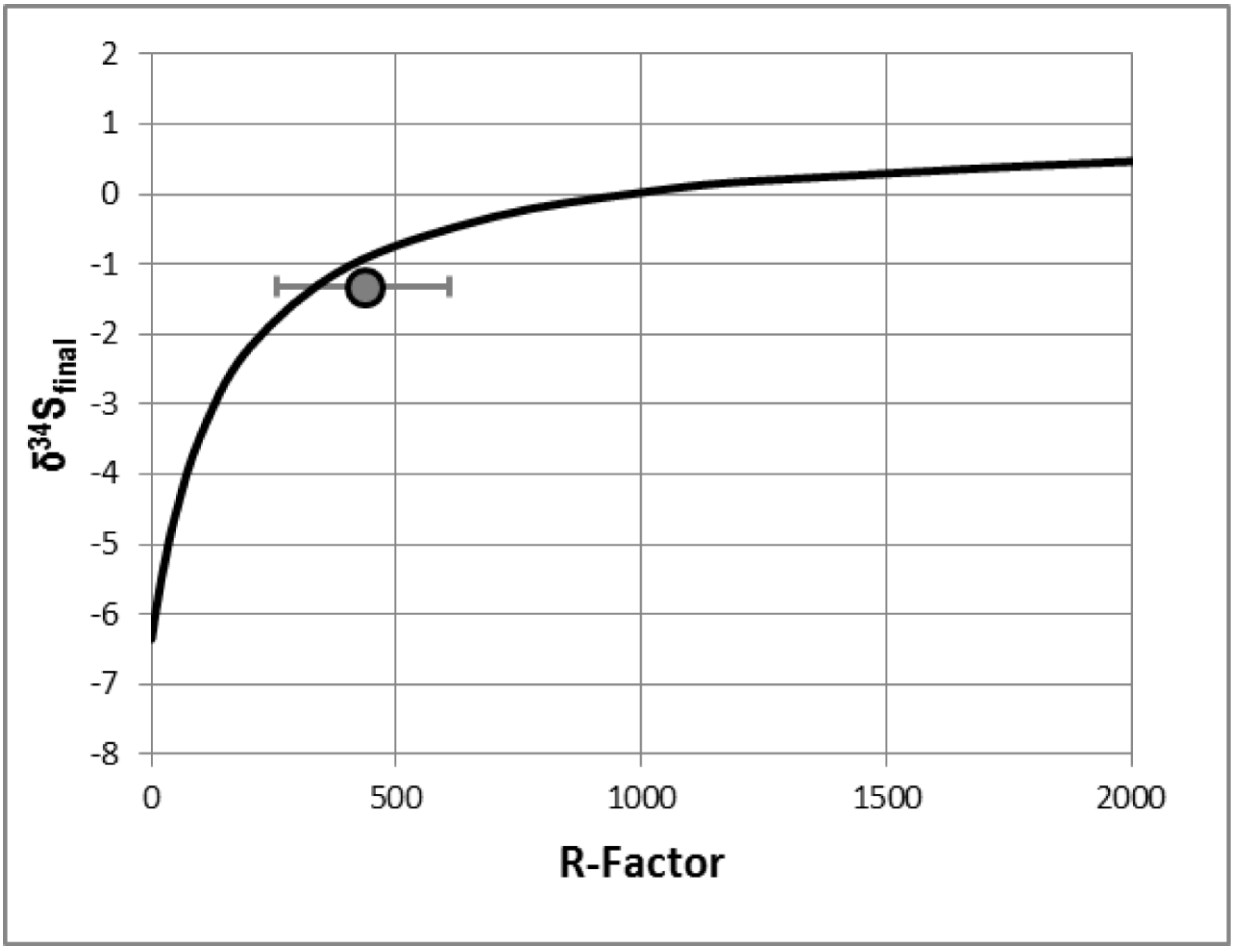

Figure 7: R-factor model showing the calculated final $\delta^{34}S$ values as a function of the R-factor. The circle with tick marks represents the calculated R-factor from our model with error bars. Values used in modeling of these curves are in Table 3.

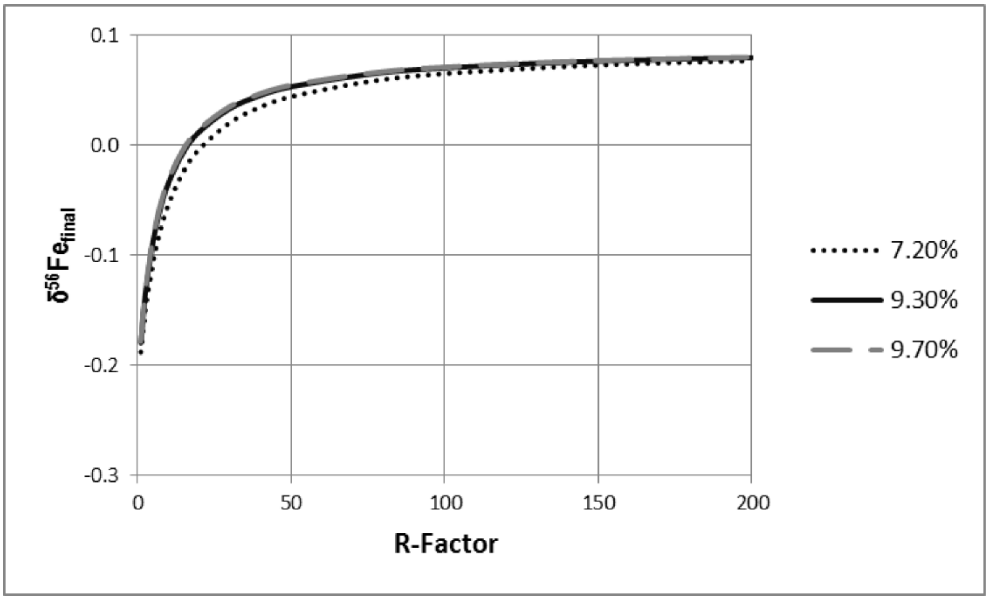

Figure 8: R-factor model showing the calculated final $\delta^{56}Fe$ values as a function of the R-factor. The curves represent initial Fe concentrations of 7.2, 9.3, and 9.7 wt% in magma used in our modeling. Values used in modeling of these curves are in Table 3.

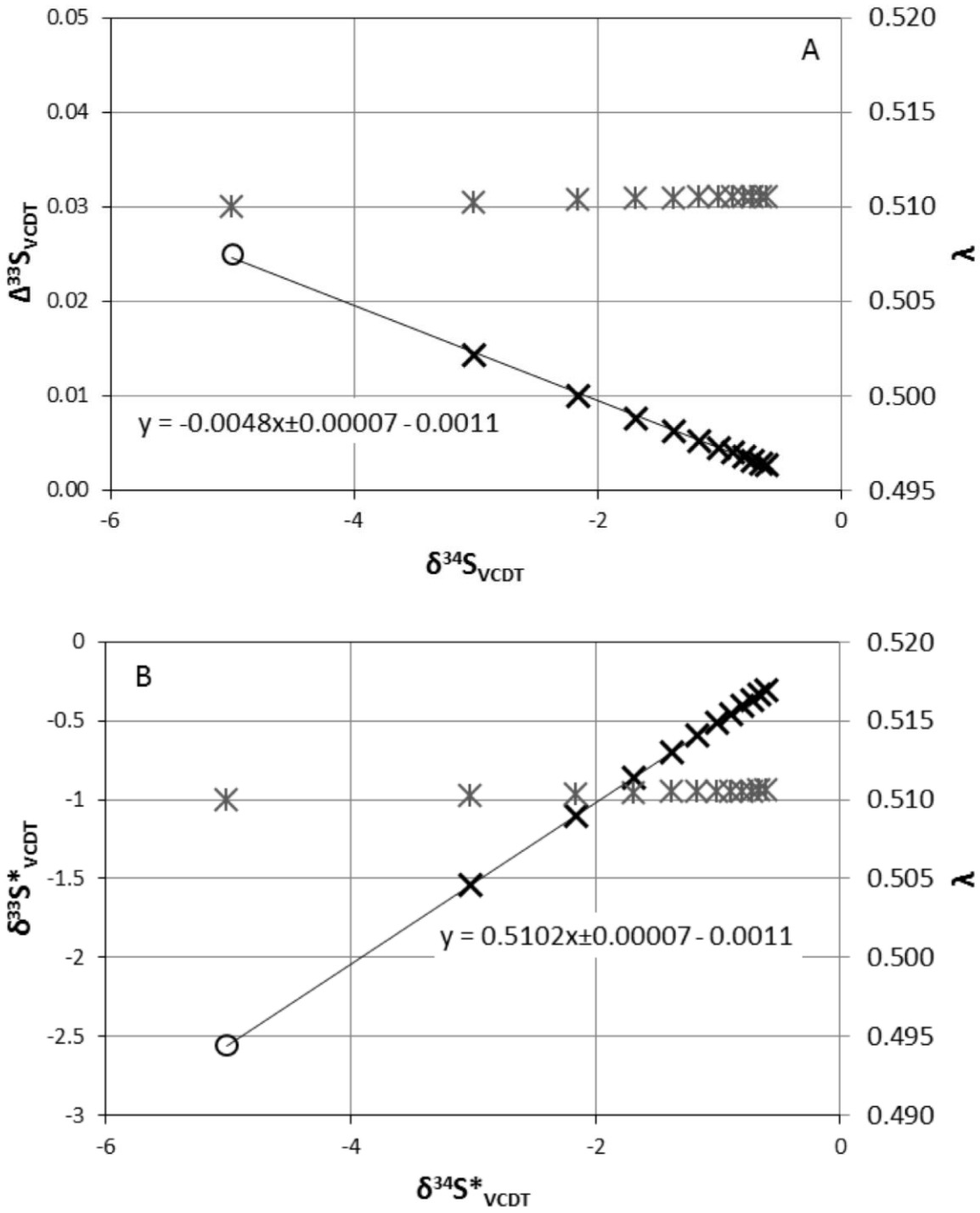

Figure 9: Modeling of preservation of S isotope relationship induced by bacterial sulfate reduction with increasing R-factor. The circle represents starting composition, with subsequent "x" points at R=100, 200, and up to 1100. In both A and B, S isotope values progress towards magmatic values maintaining the original isotopic relationship between $\Delta^{33}S$ and $\delta^{34}S$ and $\delta^{33}S^*$ and $\delta^{34}S^*$ up to R=700. The "⋇" symbols represent the change in λ with increasing R.

and is preserved in the Voisey's Bay magmatic sulfide mineralization. Preservation of this relationship in the Voisey's Bay magmatic sulfide mineralization indicates that the TGN is the dominant source of sulfur for this mineralization. Fe isotope values for the mineralization in the Voisey's Bay deposit are much more sensitive to equilibration of the sulfide liquid with silicate magma than S isotope values. Fe isotope values can be reset to magmatic values at R factors > ≈100, whereas resetting of S isotope values to magmatic values could require R factors of >2000, depending on the initial S concentration of magma. This is due to the relative concentration of these elements in the silicate magma and sulfide melt ($Fe_{silicate/sulfide} >> S_{silicate/sulfide}$). R factor for the Voisey's Bay deposit has been determined to be 433±177, which is in agreement with previously published values. This study shows that highly metamorphosed sedimentary rocks originally deposited <2.4 Ga, and magmatic sulfide deposits that incorporate sulfur from these sedimentary rocks, might preserve evidence of kinetic isotope fractionation in S isotopes that can be used to link these deposits to crustal contamination.

2.8 Applying Sulfur Isotope Methods to Magmatic Sulfide Deposits

In the study of the Voisey's Bay deposit, multiple sulfur isotope values ($\delta^{33}S$ and $\delta^{34}S$) were used to link bacterial sulfate reduction in the sedimentary protolith of the Tasiuyak gneiss to the processes forming mineralization in the deposit. This technique is a useful tool for identifying the signature of biological activity in sedimentary rocks of Proterozoic age rocks and younger where fractionation processes are strictly mass-dependent. It is robust through high grade metamorphic conditions of the sedimentary rocks, and at high R-factor in the formation of the magmatic sulfide deposits where the range of variability in the data is reduced but the relationship between $\delta^{33}S$ and $\delta^{34}S$ resulting from biological activity is maintained.

In comparison, in Archean-age magmatic sulfide deposits, the $\delta^{33}S$ and $\delta^{34}S$ signatures used in the Voisey's Bay study are often masked by mass independent fractionation processes. In the Hart deposit, a

komatiite-hosted magmatic sulfide deposit from the Abitibi greenstone belt, Canada, the overprint of mass-independent fractionation of sulfur isotopes has obscured the relationship between $\delta^{33}S$ and $\delta^{34}S$ that was used in the Voisey's Bay study to identify the signature of bacterial sulfate reduction. In these cases, a slightly different approach is required to identify S source based on the S isotope system. Using $\Delta^{33}S$, which represents the difference between the observed value of $\delta^{33}S$ and the expected value along the terrestrial fractionation line, to identify the effects of mass-independent fractionation, and allows for the identification of bacterial sulfate reduction on a plot of $\Delta^{33}S$ versus $\delta^{34}S$. Once the signature of the biological activity in the sedimentary rocks is identified, it can be used to link the mineralization in the Hart deposit to the sedimentary sulfur source, which will be demonstrated in the next chapter.

2.9 REFERENCES

Amelin, Y., Li, C., Valeyev, O., Naldrett, A.J. 2000. Nd-Pb-Sr isotope systematics of crustal assimilation in the Voisey's Bay and Mushuau intrusions, Labrador, Canada. Economic Geology, 96; 815-830.

Archer, C., Vance, D. 2006. Coupled Fe and S isotope evidence for Archean microbial Fe(III) and sulfate reduction. Geology, 42; 153-156.

Beard, B.L., Johnson, C.M. 2004. Fe isotope variations in the modern and ancient Earth and other planetary bodies. Reviews in Mineralogy and Geochemistry, 55; 319-357.

Beard, B.L., Johnson, C.M., Skulan, J.L., Nealson, K.H., Cox, L., Sun, H. 2003 Application of Fe isotopes to tracing the geochemical and biological cycling of Fe. Chemical Geology, 195; 87-117.

Bente, K., Nielsen, H. 1982. Experimental S isotope fractionation studies between coexisting bismuthinite (Bi_2S_3) and sulfur (S^0), Earth and Planetary Science Letters, 59; 18-20.

Bekker, A., Barley, M.E., Fiorentini, M.L., Rouxel, O.J., Rumble, D., Beresford, S.W. 2009. Atmospheric sulfur in Archean komatiite-hosted nickel deposits. Science, 326; 1086-1089.

Bigeleisen, J., Mayer, M.G. 1947. Calculation of equilibrium constants for isotopic exchange reactions. The Journal of Chemical Physics, 15; 261-267.

Campbell, I.H., Naldrett, A.J. 1979. The influence of silicate:sulfide ratios on the geochemistry of magmatic sulfides. Economic Geology, 75; 1503-1506.

Canfield, D. E. 2001. Biogeochemistry of sulfur isotopes. Reviews in Mineralogy and Geochemistry, 43; 607–636.

Canfield, D.E., Raiswell, R.R., Westrich, J.T., Reaves, C.M., Berner, R.A. 1986. The use of chromium reduction in the analysis of reduced inorganic sulfur in sediments and shales. Chemical Geology, 54; 149-155.

Chaussidon, M., Albarede, F., Sheppard, S.M.F. 1989. Sulfur isotope heterogeneity in the mantle from ion microprobe measurements of sulfide inclusions in diamonds. Nature, 330; 242-244.

Dauphas, N. Rouxel, O. 2006. Mass spectrometry and natural variations of iron isotopes. Mass Spectrometry Reviews, 25; 515-550.

Evans-Lamswood, D.M., Butt, D.P., Jackson, R.S., Lee, D.V., Muggridge, M.G., Wheeler, R.I., Wilton, D.H.C. 2000. Physical controls associated with the distribution of sulfides in the Voisey's Bay Ni-Cu-Co deposit, Labrador. Economic Geology, 96; 749-769.

Farquhar, J., Wing, B.A. 2003. Multiple sulfur isotopes and the evolution of the atmosphere. Earth and Planetary Science Letters, 213; 1-13.

Farquhar, J., Johnston, D.T., Wing, B.A., Habicht, K.S., Canfield, D.E., Airieau, S., Thiemens, M.H. 2003. Multiple sulfur isotopic interpretations of biosynthetic pathways: implications for biological signatures in the sulfur isotope record. Geobiology, 1; 27-36.

Hubberten, H-W. 1980. Sulfur isotope fractionation in the Pb-S, Cu-S and Ag-S systems. Geochemical Journal, 14; 177-184.

Johnson, C.M., Beard, B.L., Beukes, N.J., Klein, C. and O'Leary, J.M. 2003. Ancient geochemical cycling in the Earth as inferred from Fe isotope studies of banded iron formations from the Transvaal Craton. Contributions to Mineralogy and Petrology, 144; 523-547.

Johnston, D.T. 2011. Multiple sulfur isotopes and the evolution of Earth's surface sulfur cycle. Earth-Science Reviews, 106; 161-183.

Johnston, D.T., Farquhar, J., Wing, B.A., Kaufman, A.J., Canfield, D.E., Habicht, K.S. 2005. Multiple sulfur isotope fractionations in biological systems: a case study with sulfate reducers and sulfur disproportionators. American Journal of Science, 305; 645-660.

Johnston, D.T., Farquhar, J., Canfield, D.E. 2007. Sulfur isotope insights into microbial sulfate reduction: When microbes meet models. Geochimica et Cosmochimica Acta, 71; 3929-3947.

Keays, R.R., Lightfoot, P.C. 2010. Crustal sulfur is required to form Ni-Cu sulfide deposits: evidence from chalcophile element signatures of Siberian and Deccan Trap basalts. Mineralium Deposita, 45; 241-257.

Lambert, D.D., Frick, L.R., Foster, J.G., Li, C., Naldrett, A.J. 2000. Re-Os isotope systematics of the Voisey's Bay Ni-Cu-Co magmatic sulfide system, Labrador, Canada: II. Implications for parental magma chemistry, ore genesis, and metal redistribution. Economic Geology, 96; 867-888.

Lesher, C.M., Groves, D.I. 1986. Controls on the formation of komatiite-associated nickel-copper sulfide deposits. *In:* Geology and metallogeny of copper deposits. *Edited by:* A.D. Genkin, A.J. Naldrett, J.D. Ridge, R.H. Sillitoe, F.M. Vokes. Springer Verlag, Heidelberg, pp. 43-62.

Lesher, C.M., Burham, O.M. 2001. Multicomponent elemental and isotopic mixing in N-Cu-(PGE) ores at Kambalda, Western Australia. The Canadian Mineralogist, 39; 421-446.

Li, C., Naldrett, A.J. 1999. Geology and petrology of the Voisey's Bay intrusion: reaction of olivine with sulfide and silicate liquids. Lithos, 47; 1-31.

Li, C., Lightfoot, P.C., Amelin, Y., Naldrett, A.J. 2000. Contrasting petrological and geochemical relationships in the Voisey's Bay and Mushuau intrusions, Labrador, Canada: implications for ore genesis. Economic Geology, 96; 771-799.

Li, C., Ripley, E.M., Naldrett, A.J. 2003. Compositional variations of olivine and sulfur isotopes in the Noril'sk and Talnakh Intrusions, Siberia: Implications for ore-forming processes in dynamic magma conduits. Economic Geology, 98; 69-86.

Lightfoot, P.C., Naldrett, A.J. 1999. Geological and geochemical relationships in the Voisey's Bay Intrusion, Nain Plutonic Suite, Labrador, Canada. *In:* Keays, R.R., Lesher, C.M., Lightfoot, P.C., and Farrow, C.E.G. (eds.) Dynamic processes in magmatic ore deposits and their application to mineral exploration, Geological Association of Canada, Short Course Notes, v. 13, p. 1-30.

Lightfoot, P.C., Keays, R.R., Evans-Lamswood, D., Wheeler, R. 2012. S saturation history of Nain Plutonic Suite mafic intrusions: origin of the Voisey's Bay Ni-Cu-Co sulfide deposit, Labrador, Canada. Mineralium Deposita, 47; 23-50.

Miller, M.F. 2002. Isotopic fractionation and the quantification of ^{17}O anomalies in the oxygen three-isotope system: an appraisal and geochemical significance. Geochimica et Cosmochimica Acta, 66; 1881-1889.

Naldrett, A.J. 2010. From the mantle to the bank: the life of a Ni-Cu-(PGE) sulfide deposit. South African Journal of Geology. 113; 1-32.

Naldrett, A.J., Li, C. 2007. The Voisey's Bay deposit, Labrador, Canada. *In:* Goodfellow, W.D. ed. , Mineral Deposits of Canada: A Synthesis of Major Deposit-Types, District Metallogeny, the Evolution of Geological Provinces, and Exploration Methods: Geological Association of Canada, Mineral Deposits Division, Special Publication No. 5, p. 387-407.

Naldrett, A.J., Asif, M., Krstic, S., Li, C. 2000. The composition of mineralization at the Voisey's Bay Ni-Cu sulfide deposits, with special reference to Platinum-group elements. Economic Geology, 95; 845-865.

Ohmoto, H., Goldhaber, M., 1997. Sulfur and carbon isotopes, *In:* Barnes, H.L. ed., Geochemistry of hydrothermal ore deposits, 3rd edition: New York, John Wiley and Sons, p. 517–611.

Ohmoto H., Lasaga A.C. 1982. Kinetics of reactions between aqueous sulfates and sulfides in hydrothermal systems. Geochimica et Cosmochimica Acta, 46; 1727-1745.

Ohmoto H., Rye R.O. 1979. Isotopes of sulfur and carbon, *In:* Barnes, H.L. et., Geochemistry of Hydrothermal Ore Deposits, 2nd edition: New York, John Wiley and Sons, p. 509-567.

Ono, S. 2008. Multiple-sulfur isotope biosignatures. Space Science Reviews, 135; 203-220.

Ono, S., Wing, B., Johnston, D., Farquhar, J., Rumble, D. 2006. Mass-dependent fractionation of quadruple stable sulfur isotope system as a new tracer of sulfur biogeochemical cycles. Geochimica et Cosmochimica Acta, 70; 2238-2252.

Rawlings-Hinchey, A.M., Sylvester, P.J., Myers, J.S., Dunning, G.R., Kosler, J. 2003. Paleoproterozoic crustal genesis: calc-alkaline magmatism of the Torngat Orogen, Voisey's Bay area, Labrador. Precambrian Research, 125; 55-85.

Ripley, E.M., Li, C. 2003. Sulfur isotope exchange and metal enrichment in the formation of magmatic Cu-Ni-(PGE) deposits. Economic Geology, 98; 635-641.

Ripley, E.M., Park, Y.R., Li, C., Naldrett, A.J. 1999. Sulfur and oxygen isotopic evidence of country rock contamination in the Voisey's Bay Ni-Cu-Co deposit, Labrador, Canada. Lithos, 47; 53–68.

Ripley, E.M., Park, Y.-R., Naldrett, A.J., Li, C. 2000. Oxygen isotopic studies of the Voisey's Bay Ni-Cu-Co deposit, Labrador, Canada. Economic Geology, 95; 831–844.

Ripley, E.M., Li, C., Shin, D. 2002, Paragneiss assimilation in the genesis of magmatic Ni-Cu-Co sulfide mineralization at Voisey's Bay, Labrador; $\delta^{34}S$, $\delta^{13}C$, and Se/S evidence. Economic Geology, 97; 1307-1318.

Rouxel, O.J., Bekker, A., Edwards, K.J. 2005. Iron isotope constraints of the Archean and Paleoproterozoic ocean redox state. Science, 307; 1088-1091.

Rudnick, R.L., Eldridge, C.S., Bulanova, G.P. 1993. Diamond growth history from in situ measurement of Pd and S isotopic compositions of sulfide inclusions. Geology, 21; 13-16.

Ryan, B. 2000. The Nain-Churchill boundary and the Nain Plutonic Suite: A regional perspective on the geologic setting of the Voisey's Bay Ni-Cu-Co deposit. Economic Geology, 95; 703–724.

Schuessler, J.A., Schoenberg, R., Behrens, H, von Blanckenburg, F. 2007. The experimental calibration of the iron isotope fractionation factor between pyrrhotite and peralkaline rhyolitic melt. Geochimica et Cosmochimica Acta, 71; 417-433.

Scoates, J.S., Mitchell, J.N. 2000. The evolution of troctolitic and high Al basaltic magmas in Proterozoic anorthosite plutonic suites and implications for the Voisey's Bay massive Ni-Cu sulfide deposit. Economic Geology, 95; 677-701.

Scott, D.L. 1998. An overview of the U-Pb geochronology of the Paleoproterozoic Torngat Orogen, Northeastern Canada. Precambrian Research, 91; 91-107.

Szaran, J. 1996. Experimental investigation of sulfur isotopic fractionation between dissolved and gaseous H_2S. Chemical Geology, 127; 223-228.

Teng, F-Z., Dauphas, N., Helz, R.T. 2008. Iron isotope fractionation during magmatic differentiation in Kilauea Iki lava lake. Science, 320; 1620-1622.

Urey, H.C. 1947. The thermodynamic properties of isotopic substances. Journal of the Chemical Society, 1947; 562-581.

Wendlandt, R.F. 1982. Sulfide saturation of basalt and andesite melts at high pressures and temperatures. American Mineralogist, 67; 877-885.

Weyer, S. 2008. What drives iron isotope fractionation in magma? Science, 320; 1600-1601.

Yamaguchi, K.E., Johnson, C.M., Beard, B.L., Ohmoto, H. 2005. Biogeochemical cycling of iron in the Archean-Paleoproterozoic Earth: Constraints from iron isotope variations in sedimentary rocks from the Kaapvaal and Pilbara Cratons. Chemical Geology, 218; 135-169.

CHAPTER 3: TRACING SOURCES OF CRUSTAL CONTAMINATION USING MULTIPLE S AND FE ISOTOPES IN THE HART KOMATIITE-ASSOCIATED NI-CU-(PGE) SULFIDE DEPOSIT, ABITIBI GREENSTONE BELT, ONTARIO, CANADA

R.S. Hiebert[1], A. Bekker[2,1], M.G. Houlé[3,1], B.A. Wing[4], O.J. Rouxel[5]

[1]Department of Geological Sciences, University of Manitoba, Winnipeg, MB R3T 2N2, Canada

[2]Department of Earth Sciences, University of California, Riverside, CA 92521, USA

[3]Geological Survey of Canada, Québec, QC G1K 9A9, Canada

[4]Department of Earth and Planetary Sciences and GEOTOP, McGill University, Montréal, QC H3A 0E8, Canada

[5]IFREMER, Centre de Brest, Unité Géosciences Marines, Plouzané 56470, France

This chapter is a modified version of the paper published in Economic Geology as:

Hiebert, R.S., Bekker, A., Houlé, M.G., Wing, B.A., Rouxel, O.J. 2016. Tracing sources of crustal contamination using multiple S and Fe isotopes in the Hart komatiite-associated Ni-Cu-(PGE) sulphide deposit, Abitibi greenstone belt, Ontario, Canada. Mineralium Deposita, 51; 919-935.

3.1 ABSTRACT

Assimilation by mafic to ultramafic magmas of sulfur-bearing country rocks is considered an important contributing factor to reach sulfide saturation and form magmatic Ni-Cu-(PGE) sulfide deposits. Sulfur-bearing sedimentary rocks in the Archean are generally characterized by mass-independent fractionation of sulfur isotopes that is a result of atmospheric photochemical reactions, which produces isotopically distinct pools of sulfur. Likewise, low-temperature processing of iron, through biological and abiotic redox cycling, produces a range of Fe isotope values in Archean sedimentary rocks that is distinct from the range of the mantle and magmatic Fe isotope values. Both of these signals can be used to identify potential country rock assimilants and their contribution to magmatic sulfide deposits. We use multiple S and Fe isotopes to characterize the composition of the potential iron and sulfur sources for the sulfide liquids that formed the Hart deposit in the Shaw Dome area within the Abitibi greenstone belt in Ontario (Canada). The Hart deposit is composed of two zones with komatiite-associated Ni-Cu-(PGE) mineralization; the main zone consists of a massive sulfide deposit at the base of the basal flow in the komatiite sequence, whereas the eastern extension consists of a semi-massive sulfide zone located 12 to 25 m above the base of the second flow in the komatiite sequence. Low $\delta^{56}Fe$ values and non-zero $\delta^{34}S$ and $\Delta^{33}S$ values of the komatiitic rocks and associated mineralization at the Hart deposit is best explained by mixing and isotope exchange with crustal materials, such as exhalite and graphitic argillite, rather than intrinsic fractionation within the komatiite.

This approach allows tracing the extent of crustal contamination away from the deposit and the degree of mixing between the sulfide and komatiite melts. The exhalite and graphitic argillite were the dominant contaminants for the main zone of mineralization and the eastern extension zone of the Hart deposit, respectively. Critically, the extent of contamination, as revealed by multiple S and Fe isotope systematics, is greatest within the deposit and decreases away from it within the komatiite flow. This pattern points to a local source of crustal contamination for the mantle-derived komatiitic melt and a

low degree of homogenization between the mineralization and the surrounding lava flow. Coupled S and Fe isotope patterns like those identified at the Hart deposit may provide a useful tool for assessing the potential of a komatiitic sequence to host Ni-Cu-(PGE).

3.2 INTRODUCTION

Exploration models for magmatic nickel-copper-platinum group element (PGE) sulfide deposits are relatively well established, and, in komatiite-associated deposits, it is generally accepted that the source of metals is the mantle-derived ultramafic magmas. However, sulfur is generally thought to be derived from an external source (Lesher, 1989), typically from the melting of sulfur-bearing country rocks to generate sulfide xenomelts (Lesher and Campbell, 1993; Lesher and Burnham, 2001). An external sulfur source is necessary due to an increase in sulfur solubility in komatiitic magmas with the decrease in pressure during the magma ascent from the mantle through the crust to near-surface environments (Wendlandt, 1982; Lesher and Groves, 1986; Mavrogenes and O'Neill, 1999). Sulfur sources can be relatively well constrained by field evidence and geological relationships for some komatiite-associated deposits, such as those at Alexo (Houlé et al., 2012), Kambalda (Lesher, 1989), or the Agnew-Wiluna belt (Fiorentini et al., 2012). However, for some deposits where more than one possible sulfur source exists, identifying the one responsible for sulfide saturation becomes more difficult.

Early attempts to determine sulfur sources for komatiite-associated mineralization relied on $\delta^{34}S$. However, the range of bulk-rock $\delta^{34}S$ values in Archean supracrustal deposits is much smaller than in their Phanerozoic counterparts, resulting in potential crustal sources with $\delta^{34}S$ values that are largely indistinguishable from the mantle range (Ripley, 1999), which makes this approach inconclusive in some cases. More recently, multiple sulfur isotopes have been used to link nickel sulfide mineralization to sedimentary sulfur sources in Archean komatiite-associated deposits (Bekker et al., 2009; Fiorentini et al., 2012; Konnunaho et al., 2013; Hofmann et al., 2014).

This study expands on these previous efforts by linking magmatic nickel sulfide mineralization to the sedimentary sulfur source at the Hart deposit and investigates the lateral and vertical variations of the stable isotope signatures, using multiple sulfur isotopes and iron isotopes, with increasing distance away from the mineralization within the host komatiite flows. Stable isotope ($\delta^{34}S$, $\Delta^{33}S$, and $\delta^{56}Fe$), major- and trace-element geochemistry are used to identify the most likely sedimentary contaminants for the genesis of the Hart komatiite-associated Ni-Cu-(PGE) deposit within the Shaw Dome area in the Abitibi greenstone belt (Ontario, Canada).

3.3 BACKGROUND

Under present terrestrial conditions, most sulfur isotope fractionations are controlled by relative isotope mass difference, leading to a close 'mass-dependent' correspondence between δ values of $\delta^{33}S \approx 0.5 \times \delta^{34}S$. However, as a result of photochemical reactions in the anoxic Archean atmosphere, atmospherically processed Archean sulfur exhibits mass-independent fractionation that can be characterized by the difference between the $\delta^{33}S$ value expected from normal mass-dependent fractionation and the measured $\delta^{33}S$ value (Farquhar et al., 2000; Farquhar and Wing, 2003). It is calculated

$$\Delta^{33}S = \delta^{33}S - \left[\left(\frac{\delta^{34}S}{1000} + 1\right)^{\lambda_{RFL}} - 1\right] \times 1000 \quad (7)$$

where λ_{RFL} is the slope of the reference mass-dependant fractionation line, equal to 0.515.

Photochemically fractionated sulfur was delivered to Archean seawater and ultimately incorporated into sedimentary rocks. Unlike modern oceans, the Archean oceans had relatively low sulfate concentrations, less than 100-200 µmol L^{-1} (Habicht et al., 2002; Jamieson et al., 2013), which resulted in the preservation of small isotopic fractionations caused by microbial S cycling in marine sediments (Wing and Halevy, 2014). As a result, Archean sediments do not exhibit the large range in $\delta^{34}S$ values seen in

more recent marine sediments, hampering discrimination between crustal and mantle sulfur. However, Archean sedimentary rocks typically exhibit mass-independent fractionation of S isotopes as shown by their non-zero $\Delta^{33}S$ values (Farquhar et al., 2000; Farquhar and Wing, 2003). Therefore, multiple sulfur isotope ratios can constrain the sulfur source for nickel-copper-(PGE) sulfide mineralization in mafic to ultramafic systems and vector toward prospective areas, where crustal sulfur incorporation occurred and triggered sulfide saturation (e.g., Bekker et al., 2009).

Additionally, for several Archean lithologies, such as ferruginous sediments and organic matter-rich shales, the $\delta^{56}Fe$ (and $\delta^{57}Fe$) values have been shown to exhibit significant variability (Johnson et al., 2003; Rouxel et al., 2005; Yamaguchi et al., 2005; Archer and Vance, 2006; Dauphas and Rouxel, 2006), and can be used to provide independent constraints on the mechanisms that triggered sulfur saturation and the extent of country rock assimilation.

Once the signatures of potential sedimentary sources are established, tracing the contamination in the komatiite could provide insights into the flow regime and cooling history of the komatiite (Lesher and Arndt, 1995). Utilization of both S and Fe isotopes provides two tracers that are sensitive to different degrees of contamination (Hiebert et al., 2013b). Contaminant to komatiite ratios can be quantified with 2-component mixing and isotope exchange equations (Campbell and Naldrett, 1979; Lesher and Burnham, 2001; Ripley and Li, 2003); there is more Fe than S in komatiite magmas, which makes Fe isotopes in sulfide xenomelts more sensitive to lower silicate magma-sulfide melt ratios (R factor) than S isotopes.

3.4 GEOLOGICAL SETTING

Komatiites and komatiite-associated Ni-Cu-(PGE) deposits in the Abitibi greenstone belt (Figure 3) are recognized worldwide for their outstanding preservation and exposure (Barnes and Naldrett, 1987; Houlé and Lesher, 2011), including well-studied examples at Pyke Hill (Pyke et al., 1973; Houlé et al.,

2009), Dundonald Beach (Houlé et al., 2008), and Alexo (Houlé et al., 2012). The Abitibi greenstone belt can be subdivided into 7 volcanic episodes with associated lesser sedimentary packages (Thurston, 2008). Of these, four episodes contain most of the komatiites, but only two host significant Ni-Cu-(PGE) mineralization; the 2720 – 2710 Ma Kidd-Munro and 2710 – 2704 Ma Tisdale volcanic episodes. Most of the past and ongoing nickel production from this type of deposit in the Abitibi greenstone belt has come from the Shaw Dome area (Figure 3), which hosts the Hart deposit located approximately 30 km southeast of Timmins (Houlé and Lesher, 2011).

The volcano-sedimentary succession in the Shaw Dome comprises from oldest to youngest: 1) massive and pillowed intermediate volcanic rocks, thin, but laterally extensive, iron formations and subordinate massive to volcaniclastic felsic volcanic rocks of the 2734–2724 Ma Deloro volcanic episode; 2) felsic to intermediate volcaniclastic rocks intercalated with komatiitic dykes, sills, lavas and less extensive iron formations of the lower part of the 2710 – 2704 Ma Tisdale volcanic episode; 3) intercalated tholeiitic mafic and komatiitic volcanic rocks of the middle part of the Tisdale volcanic episode; and 4) calc-alkaline felsic to intermediate volcanic rocks in the upper part of the Tisdale volcanic episode (Houlé et al., 2010a, b; Houlé and Lesher, 2011).

The main mineralized zone of the Hart deposit is hosted in the basal komatiite flow of the middle Tisdale episode, where several stacked komatiite flows overly, and cross-cut the felsic to intermediate volcanic and sedimentary rocks of the lower Tisdale episode (Houlé et al., 2010a, b; Houlé and Lesher, 2011). The eastern extension of the Hart deposit is hosted within the second komatiite flow in this succession. Combined, the main zone contains 1.9 Mt with an average grade of 1.38% Ni (Houlé and Lesher, 2011). Following the terminology of Lesher and Keays (2002), the main zone of the Hart deposit is a classic, Type I stratiform basal mineralization hosted by thick, olivine orthocumulate to mesocumulate komatiite units in which the mineralization is localized at the base of a wide (>200 m) embayment into its footwall

rocks (Figures 10 and 11). The embayment is interpreted to have been produced by thermomechanical erosion of underlying felsic volcanic rocks and iron formation (Houlé et al., 2010b). In addition to the main zone, a secondary zone of semi-massive, net-textured, and disseminated sulfide, referred to as the eastern extension, is present 12 – 25 m above the base of the second flow. No significant mineralization is known to exist in komatiites or basalts above the second komatiite flow. Komatiites in the study area have been strongly altered to serpentinite, but pseudomorphs of original olivine cumulates are commonly preserved. All rocks in the study area have been metamorphosed under greenschist facies conditions.

The footwall rocks are dominantly composed of felsic to intermediate volcanic and volcaniclastic rocks with a lesser, but regionally extensive, banded iron formation, having variable content of magnetite-rich layers that are chert-rich locally, and minor graphitic argillite. In the vicinity of the Hart deposit, some of the iron formation have been interpreted to represent an exhalite (Figure 12) due to the predominance of chert and chert-rich lithologies. The exhalite typically contains minor laminae of Fe-oxides or sulfides (e.g., sample H11-16-411.4; 86.2% SiO_2, 10.9% Fe_2O_3). Locally, the chert or chert-rich lithologies within the exhalite grade into more typical banded iron formation (e.g., sample H11-13C-387.2; 41.73% SiO_2, 37.44% Fe_2O_3), or barren massive sulfides (pyrite), but these lithologies do not extend laterally for more than a few tens of meters in the area of the Hart deposit (Hiebert et al., 2013a), despite the regional extent of iron formation (Houlé et al., 2010b). Sulfides within the exhalite are typically masses of fine-grained pyrrhotite (0.1 – 0.2 mm in size) that have been locally recrystallized to form larger pyrite grains (0.25 – 0.6 mm in size; Figure 12d). Apparent thicknesses of exhalite observed in drillcore are typically less than 10 m, but may be up to 25 m thick.

The graphitic argillite is observed as two thin (<5 m) layers in drillcore northeast of the main zone of mineralization in the Hart deposit. It is composed predominantly of graphite (45 – 65 vol %) and pyrite

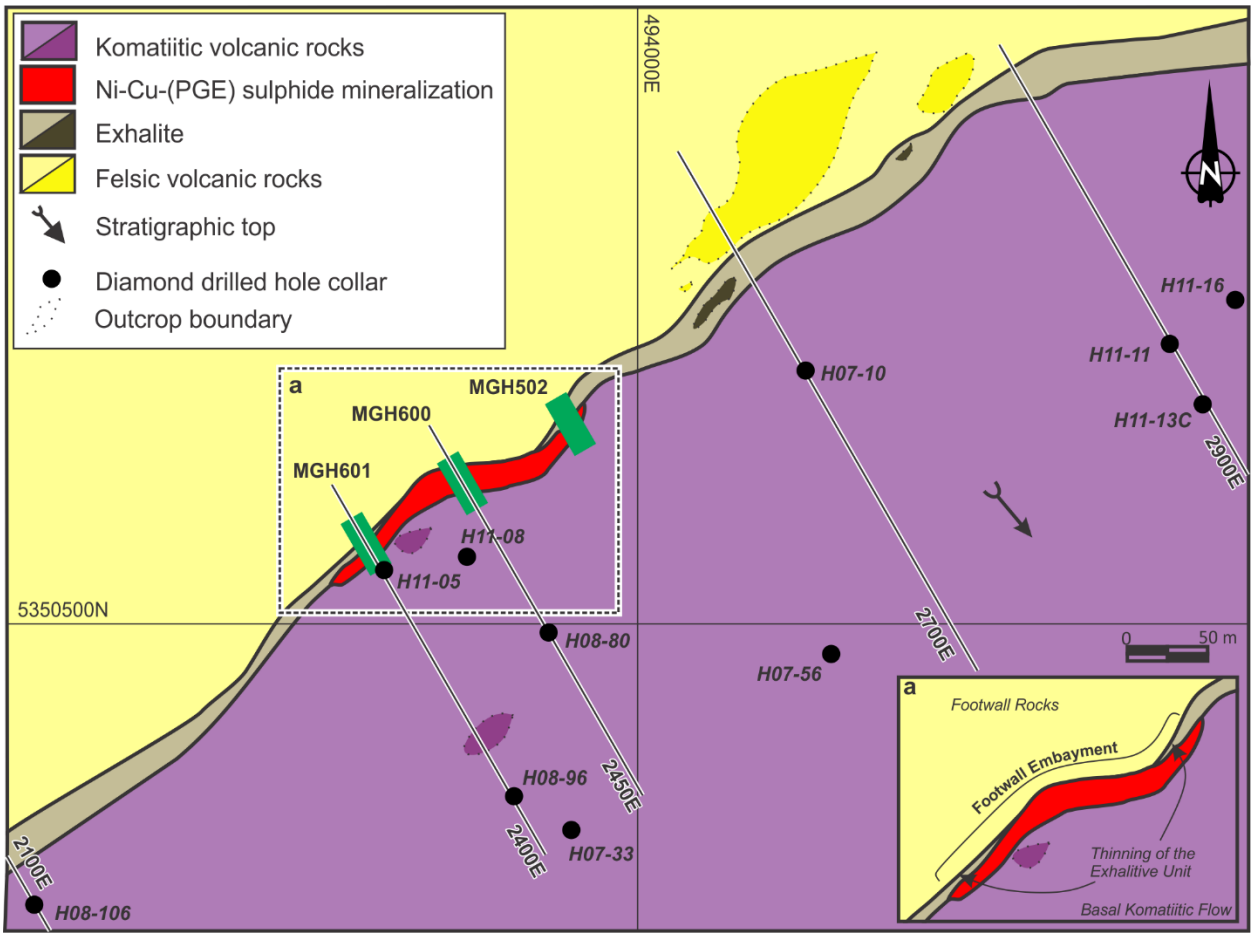

Figure 10: Geologic map of the Hart deposit area (modified from Houlé et al. 2010b). Drill hole collar locations and section lines for composite isotope data traverses through the deposit are indicated. Locations of sampled surface trenches are indicated by the green bars.

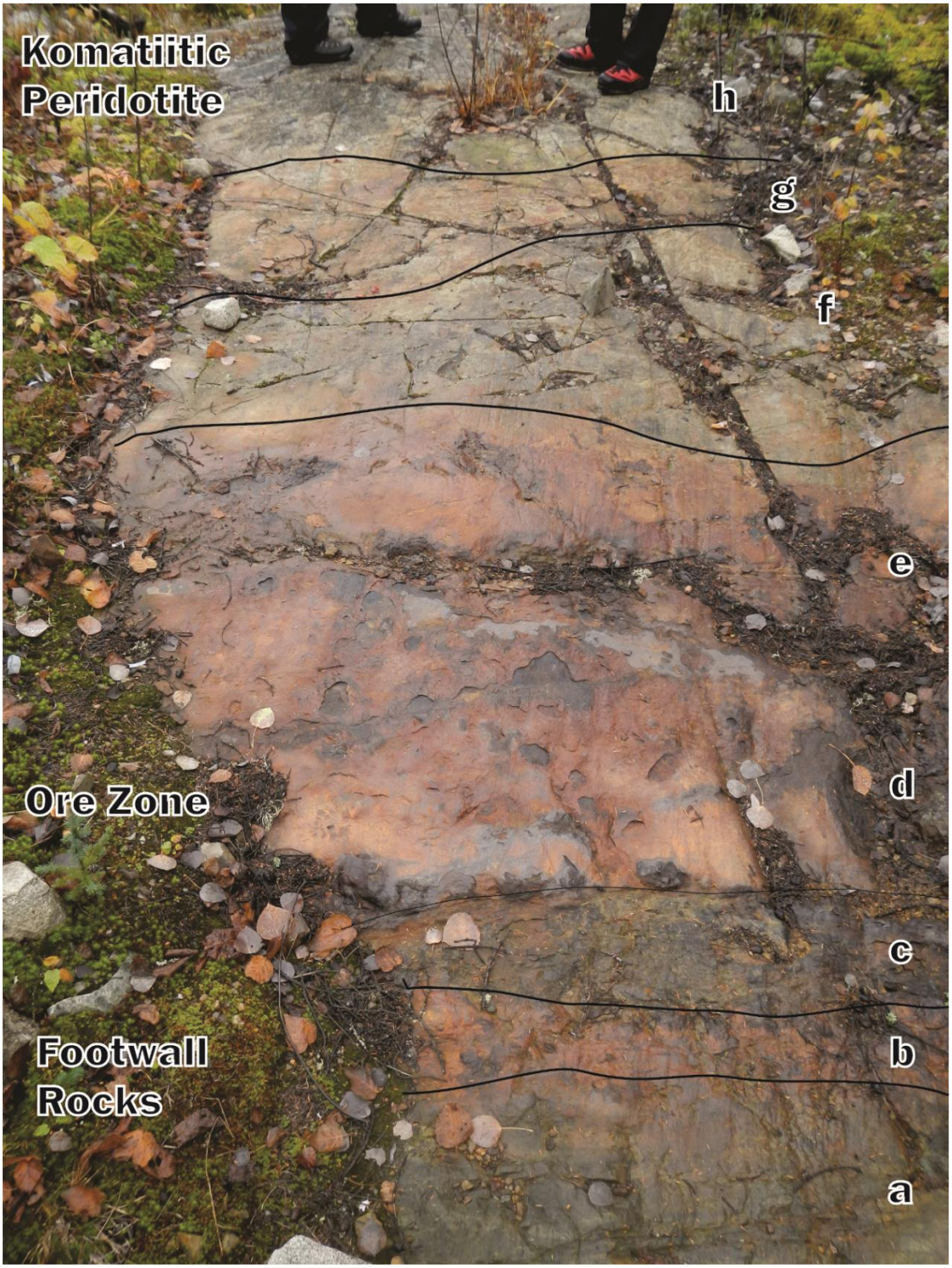

Figure 11: Field photograph of mineralized zone in trench MGH600. From stratigraphic base to top; a – felsic volcanic rocks, b – exhalite, c – felsic volcanic rocks, d – massive sulfides, e – net-textured sulfides, f – barren komatiite, g – disseminated sulfides in komatiitic peridotite, h – barren komatiitic peridotite.

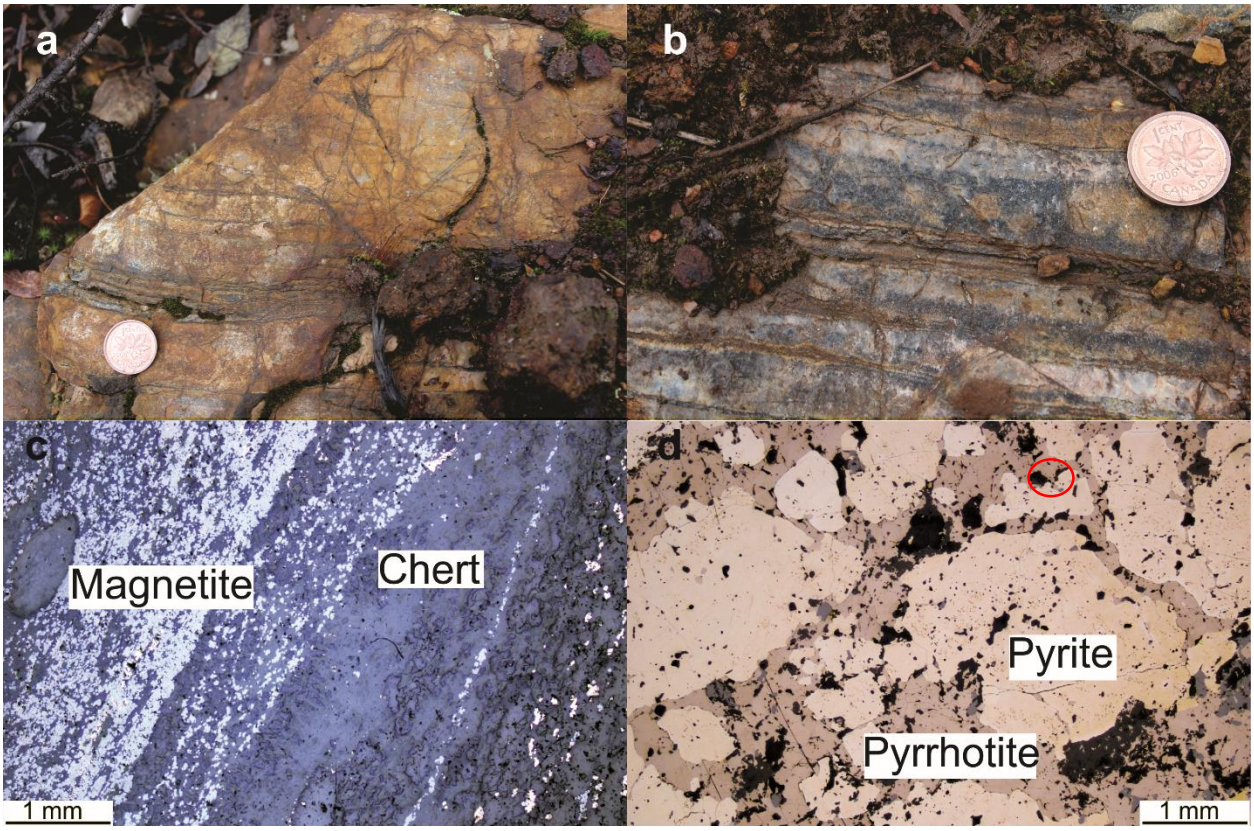

Figure 12: a-b Outcrop photographs of the exhalite unit, taken along strike from the Hart area, of chert (a) and iron formation (b) lithologies. The coin is 18 mm in diameter on figurea a and b. **c-d** Reflected light photomicrographs of exhalite in the footwall of the Hart deposit: oxide-rich laminae in chert (c: sample H11-13C-363) and fine pyrrhotite sulfide grains replaced by coarse pyrite grains containing inclusions of pyrrhotite (circled) in a barren sulfide lens within the exhalite unit (d: sample H11-08-58.3).

(10 – 40 vol %), with lesser amounts of metamorphic chlorite, epidote, and quartz (10 – 20 vol %; Figure 13a). Sulfide in the graphitic argillite takes two forms: finely disseminated pyrite (<0.1 mm in size; Figure 13b) or large (1 – 1.5 cm in diameter) pyrite nodules and bands (Figure 13a and c).

3.5 Material analyzed and analytical methods

3.5.1 Sampling methodology

The 93 samples were selected from mechanically-stripped trenches and diamond drill cores (Table 4, 5). Several transects were made within and away from the main mineralized zone at the Hart deposit to create composite traverses that include all footwall lithologies (felsic volcanic rocks, exhalite, and graphitic argillite), the mineralization (massive, semi-massive, net-textured, and disseminated sulfides), and the hosting komatiite flow immediately above the mineralization and upward into barren komatiitic flows. These transects utilized 11 diamond drill holes and 3 trenches along 5 sections on the local mine grid (Figure 10).

This sampling strategy ensured that the basal komatiitic flow, which hosts the main mineralized zone, was sampled as far as 500m east and 300m west of the main mineralized zone. The second komatiitic flow, which hosts the eastern extension zone, was only sampled west of the mineralization due to a lack of drilling east of mineralization at the time of the investigation. Additionally, one sample of the third flow from drill hole H07-33 was taken to represent barren komatiite flow that likely never interacted with the sulfur source rock.

3.5.2 Whole rock geochemistry

Samples were analyzed for major, trace, and rare-earth elements in two different laboratories: The Ontario Geological Survey Geoscience Laboratories (GeoLabs; Sudbury, Ontario), and the Acme Laboratories (Acme Labs; Vancouver, British Columbia). All the materials were crushed at the Stable Isotopes for Innovative Research (SIFIR) laboratory at the University of Manitoba to a fine powder (200

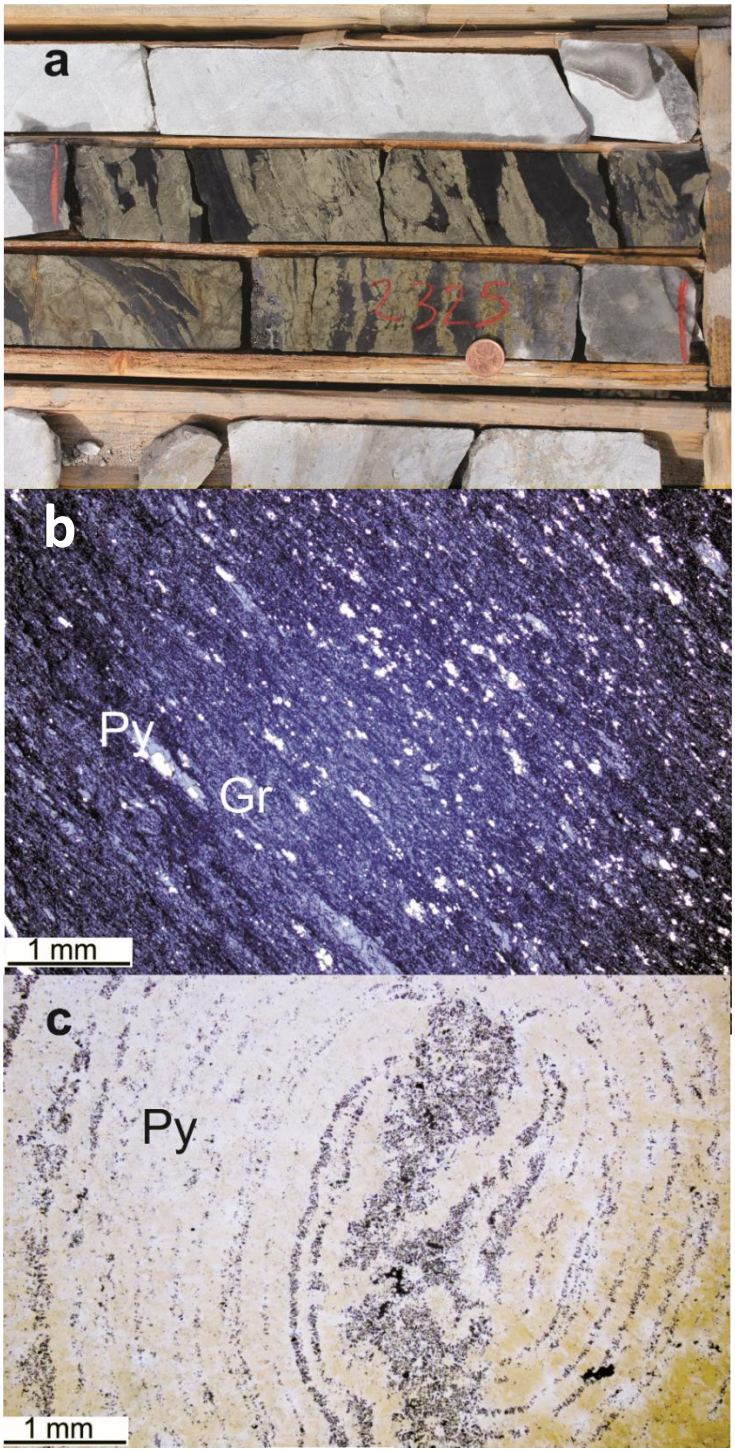

Figure 13: a Core photo of graphitic argillite showing nodules and bands of pyrite. The coin is 18 mm in diameter. **b** Photomicrograph of graphitic argillite unit in reflected-light (sample H11-13C-366.1) showing minor disseminated sulfide (bright grains) and opaque mineral (graphite). **c** Photomicrograph in reflected-light of pyrite nodule in graphitic argillite showing concentric growth bands (sample H11-13C-357.1).

Table 4: Whole rock geochemistry data for the Hart deposit. Ti, Ni, Zr, Nb, and La are in ppm, all others are in wt %.

Sample ID	H07-10-109.45	H07-10-32.1	H07-10-65.3	H07-33-128.3	H07-33-159.8
DDH/Trench	H07-10	H07-10	H07-10	H07-33	H07-33
Lithology	Felsic Volcanic	Komatiite	Komatiite	Komatiite	Spinifex Komatiite
Lab	Acme	Acme	Acme	Acme	Acme
SiO_2					
TiO_2	0.40	0.42	0.44	0.26	0.41
Al_2O_3	12.60	7.69	8.45	4.80	6.95
$Fe_2O_3^T$	7.55	10.25	11.15	9.48	10.51
MgO	2.32	21.66	20.63	24.34	21.04
MnO	0.07	0.18	0.25	0.08	0.18
CaO	3.19	7.81	8.10	3.33	8.83
Na_2O	1.68	0.20	0.06	0.01	0.13
K_2O	2.79	0.08	bdl	bdl	0.04
P_2O_5	0.09	0.03	0.03	0.01	0.03
LOI					
S	1.6	bdl	0.2	1.4	0.0
Ti					
Ni	59	1110	1443	1506	1332
Zr	150	27	9	2	19
Nb	4.4	0.9	0.6	0.5	0.6
La	11.2	1.7	0.8	0.6	1.1
Sample ID	**H07-33-193.7**	**H07-33-234.7**	**H07-33-251.2**	**H07-33-261.3**	**H07-56-182**
DDH/Trench	H07-33	H07-33	H07-33	H07-33	H07-56
Lithology	Komatiitic pyroxenite	Komatiite	Komatiite with disseminated sulfide	Felsic Volcanic	Komatiite
Lab	GeoLabs	Acme	Acme	Acme	Acme
SiO_2	45.58				
TiO_2	0.38	0.14	0.14	0.45	0.42
Al_2O_3	8.17	1.62	3.00	13.59	8.73
$Fe_2O_3^T$	12.57	8.72	9.56	9.38	12.21
MgO	20.84	37.83	28.14	2.50	19.17
MnO	0.21	0.09	0.05	0.10	0.20
CaO	8.04	0.04	0.18	3.88	8.61
Na_2O	0.21	bdl	0.01	2.35	0.38
K_2O	0.04	bdl	bdl	3.07	0.06
P_2O_5	0.03	bdl	0.00	0.11	0.03
LOI	5.1				
S	0.0	0.2	0.5	1.9	0.2
Ti	2362				
Ni	630	3348	2729	83	761
Zr	29	6	2	139	28
Nb	0.9	0.2	0.2	5.2	0.8
La	1.3	0.1	0.2	13.2	1.5

Table 4: continued.

Sample ID	H08-106-75.9	H08-106-93.65	H08-80-110.6	H08-80-112.5	H08-80-114.25
DDH/Trench	H08-106	H08-106	H08-80	H08-80	H08-80
Lithology	Komatiite	Komatiite with disseminated sulfide	Komatiite with disseminated sulfide	Semi-massive sulfide in komatiite	Massive sulfide
Lab	Acme	Acme	Acme	Acme	GeoLabs
SiO_2					4.59
TiO_2	0.41	1.03	0.19	0.05	0.01
Al_2O_3	7.78	15.47	4.01	0.98	0.13
$Fe_2O_3^T$	10.34	11.28	13.70	44.78	81.42
MgO	21.11	5.69	24.05	13.85	1.35
MnO	0.19	0.21	0.47	0.64	0.31
CaO	7.95	13.01	4.25	2.83	0.84
Na_2O	0.28	1.02	0.01	bdl	0.06
K_2O	0.08	1.60	bdl	bdl	bdl
P_2O_5	0.04	0.06	0.00	0.00	0.01
LOI					10.8
S	0.2	0.1	1.4	23.1	36.9
Ti					63
Ni	1092	73	2190	5842	4100
Zr	20	42	2	14	bdl
Nb	0.9	2.3	0.4	0.2	0.1
La	1.7	3.4	1.0	1.6	2.0
Sample ID	**H08-80-126.45**	**H08-80-134.65**	**H08-80-136**	**H08-80-139**	**H08-80-77.85**
DDH/Trench	H08-80	H08-80	H08-80	H08-80	H08-80
Lithology	Komatiite with disseminated sulfide	Semi-massive sulfide in komatiite	Stringer sulfide in komatiite	Felsic Volcanic	Komatiite with disseminated sulfide
Lab	Acme	Acme	GeoLabs	GeoLabs	Acme
SiO_2			7.78	71.45	
TiO_2	0.08	0.07	0.05	0.37	0.27
Al_2O_3	1.83	1.19	4.96	12.09	4.99
$Fe_2O_3^T$	9.49	33.93	64.20	5.16	9.54
MgO	37.11	14.49	6.28	2.49	23.85
MnO	0.07	0.20	0.14	0.11	0.16
CaO	0.15	7.12	0.08	2.37	7.07
Na_2O	0.01	0.03	0.03	4.08	0.04
K_2O	bdl	bdl	0.01	0.25	bdl
P_2O_5	bdl	bdl	0.02	0.11	0.01
LOI			14.8	1.8	
S	0.3	7.1	30.3	0.5	bdl
Ti			237	2239	
Ni	2378	7795	13909	60	1375
Zr	6	54	6	119	4
Nb	0.2	0.4	0.4	4.3	0.5
La	0.3	0.2	0.9	12.4	0.4

Table 4: continued.

Sample ID	H08-80-97.3	H08-96-259.6	H08-96-274.4	H08-96-277.8	H08-96-281
DDH/Trench	H08-80	H08-96	H08-96	H08-96	H08-96
Lithology	Komatiite with disseminated sulfide	Komatiite	Semi-massive sulfide in komatiite	Massive sulfide	Komatiite
Lab	GeoLabs	Acme	GeoLabs	Acme	GeoLabs
SiO_2	37.64		30.61		45.89
TiO_2	0.17	0.17	0.10	0.02	0.33
Al_2O_3	3.40	2.76	1.88	0.30	7.28
$Fe_2O_3^T$	12.17	11.09	25.89	79.57	11.74
MgO	30.38	34.13	25.47	0.41	21.94
MnO	0.15	0.11	0.24	0.04	0.27
CaO	2.67	0.42	1.81	0.21	7.83
Na_2O	bdl	bdl	bdl	0.00	0.12
K_2O	bdl	bdl	0.01	0.06	0.03
P_2O_5	0.01	0.01	0.01	bdl	0.02
LOI	10.8		10.8		5.0
S	0.8	1.2	6.4	41.0	0.2
Ti	1031		608		1758
Ni	2243	6807	4100	>10000	1051
Zr	12	8	6	10	20
Nb	0.3	0.3	0.2	0.2	0.7
La	0.4	0.3	0.5	1.3	1.3
Sample ID	**H08-96-283.8**	**H11-05-39.65**	**H11-05-45.55**	**H11-05-57.1**	**H11-05-58.55**
DDH/Trench	H08-96	H11-05	H11-05	H11-05	H11-05
Lithology	Massive sulfide	Komatiite	Exhalite	Semi-massive sulfide in komatiite	Komatiite
Lab	GeoLabs	Acme	GeoLabs	GeoLabs	GeoLabs
SiO_2	2.49		21.56	18.35	35.07
TiO_2	0.01	0.14	0.01	0.16	0.95
Al_2O_3	0.17	2.63	0.19	2.94	17.53
$Fe_2O_3^T$	67.44	10.07	56.44	33.82	11.29
MgO	0.27	34.79	1.96	10.70	13.87
MnO	0.05	0.12	0.19	0.12	0.64
CaO	2.23	1.09	1.50	0.12	6.94
Na_2O	0.05	bdl	0.07	0.02	2.62
K_2O	0.01	bdl	0.03	bdl	0.46
P_2O_5	bdl	0.01	0.00	0.07	0.70
LOI	24.2		17.7	32.4	8.8
S	30.7	0.1	32.2	14.4	0.1
Ti	66		53	1218	5099
Ni	4100	1999	980	4100	69
Zr	bdl	6	bdl	37	191
Nb	0.1	0.3	0.0	1.3	9.2
La	1.1	0.3	0.5	13.1	87.0

Table 4: continued.

Sample ID	H11-05-61.1	H11-05-62.35	H11-05-62.6	H11-05-62.9	H11-05-68
DDH/Trench	H11-05	H11-05	H11-05	H11-05	H11-05
Lithology	Semi-massive sulfide in komatiite	Komatiite with disseminated sulfide	Massive sulfide	Komatiite	Felsic Volcanic
Lab	Acme	Acme	GeoLabs	Acme	Acme
SiO_2			17.26		
TiO_2	0.02	0.23	0.08	0.42	0.46
Al_2O_3	0.62	4.82	1.78	13.19	14.83
$Fe_2O_3^T$	43.12	13.30	59.27	9.06	7.88
MgO	11.62	20.94	6.96	2.40	2.42
MnO	0.06	0.52	0.25	0.15	0.09
CaO	0.52	6.90	3.24	0.67	5.15
Na_2O	0.01	0.07	0.08	2.72	2.48
K_2O	bdl	bdl	0.02	4.67	2.52
P_2O_5	bdl	0.02	0.01	0.14	0.10
LOI			9.3		
S	22.3	1.6	21.0	0.4	1.9
Ti			447		
Ni	3700	1513	10216	90	178
Zr	44	21	17	187	175
Nb	0.2	0.7	0.4	5.1	5.7
La	0.2	0.8	1.6	9.3	18.2
Sample ID	**H11-08-10.45**	**H11-08-40.4**	**H11-08-52.65**	**H11-08-58.3**	**H11-08-63.9**
DDH/Trench	H11-08	H11-08	H11-08	H11-08	H11-08
Lithology	Komatiite	Komatiite with disseminated sulfide	Exhalite	Exhalite	Exhalite
Lab	GeoLabs	Acme	GeoLabs	GeoLabs	GeoLabs
SiO_2	46.89		7.19	3.57	9.16
TiO_2	0.30	0.13	bdl	0.02	0.01
Al_2O_3	5.58	2.23	0.18	0.39	0.44
$Fe_2O_3^T$	10.08	8.65	76.37	68.58	71.18
MgO	25.86	35.37	0.64	0.41	2.30
MnO	0.15	0.13	0.39	0.83	1.73
CaO	5.87	0.10	2.23	1.26	4.15
Na_2O	0.07	0.01	0.06	0.06	0.06
K_2O	0.02	bdl	0.01	0.02	0.01
P_2O_5	0.02	0.01	0.01	0.01	0.01
LOI	5.6		13.0	25.1	10.2
S	0.2	0.4	52.6	46.4	20.1
Ti	1531		43	103	81
Ni	1390	4011	400	1414	821
Zr	17	16	bdl	bdl	bdl
Nb	0.4	0.3	0.1	0.2	0.2
La	0.4	0.4	1.0	0.5	3.2

Table 4: continued.

Sample ID	H11-08-79.4	H11-11-294.5	H11-11-337.7	H11-11-352.6	H11-11-356.55
DDH/Trench	H11-08	H11-11	H11-11	H11-11	H11-11
Lithology	Felsic Volcanic	Komatiite	Komatiite with disseminated sulfide	Komatiite with disseminated sulfide	Semi-massive sulfide in komatiite
Lab	GeoLabs	GeoLabs	Acme	GeoLabs	GeoLabs
SiO_2	63.19	42.12		24.17	32.55
TiO_2	0.24	0.20	0.11	0.06	0.06
Al_2O_3	8.74	4.11	2.25	1.09	1.50
$Fe_2O_3^T$	14.57	9.67	10.37	21.66	16.82
MgO	0.98	26.21	32.77	27.45	30.29
MnO	1.18	0.12	0.08	0.09	0.05
CaO	4.57	4.66	1.22	1.68	0.59
Na_2O	0.26	bdl	0.01	bdl	bdl
K_2O	1.11	0.01	bdl	0.03	0.03
P_2O_5	0.05	0.01	0.00	0.01	0.01
LOI	5.0	12.5		18.7	16.4
S	4.9	0.0	1.4	9.3	7.6
Ti	1455	1092		286	359
Ni	68	1489	6619	34105	16503
Zr	83	13	4	bdl	6
Nb	3.2	0.3	0.2	0.1	0.2
La	13.5	0.3	0.5	0.4	0.6
Sample ID	**H11-11-367.2**	**H11-11-407**	**H11-11-407**	**H11-13C-265.85**	**H11-13C-282.8**
DDH/Trench	H11-11	H11-11	H11-11	H11-13C	H11-13C
Lithology	Komatiite	Komatiite with disseminated sulfide	Komatiite with disseminated sulfide	Komatiite	Komatiite with disseminated sulfide
Lab	Acme	GeoLabs	Acme	GeoLabs	Acme
SiO_2		43.59		40.20	
TiO_2	0.18	0.50	0.54	0.13	0.18
Al_2O_3	3.29	9.59	9.67	2.65	3.38
$Fe_2O_3^T$	9.75	12.76	12.07	7.06	12.92
MgO	25.39	19.29	18.04	26.66	28.61
MnO	0.16	0.22	0.22	0.10	0.14
CaO	6.45	8.66	8.62	7.03	2.24
Na_2O	0.01	0.40	0.44	bdl	0.02
K_2O	bdl	0.07	0.12	0.01	bdl
P_2O_5	0.01	0.04	0.04	0.00	0.01
LOI		4.9		14.4	
S	0.6	0.0	bdl	0.8	1.5
Ti		3076		730	
Ni	1995	802	842	1814	9333
Zr	2	30	25	8	6
Nb	0.3	0.9	1.0	0.2	0.4
La	0.5	0.8	1.0	0.3	0.4

Table 4: continued.

Sample ID	H11-13C-301.6	H11-13C-329.3	H11-13C-339.1	H11-13C-349.6	H11-13C-357.1
DDH/Trench	H11-13C	H11-13C	H11-13C	H11-13C	H11-13C
Lithology	Komatiite	Komatiite	Komatiite	Felsic Volcanic	Graphitic Argillite
Lab	Acme	Acme	Acme	GeoLabs	GeoLabs
SiO_2				42.73	10.52
TiO_2	0.38	0.28	0.45	0.56	0.08
Al_2O_3	7.33	5.23	7.78	10.15	2.09
$Fe_2O_3^T$	9.32	8.42	10.92	13.33	55.47
MgO	18.01	21.91	21.33	15.53	0.39
MnO	0.20	0.15	0.20	0.26	0.02
CaO	10.12	7.70	8.21	12.44	0.39
Na_2O	0.01	0.01	0.11	0.39	0.06
K_2O	0.57	bdl	bdl	0.08	0.53
P_2O_5	0.03	0.02	0.03	0.05	0.02
LOI				3.0	30.5
S	0.1	0.1	bdl	0.0	47.4
Ti				3092	494
Ni	936	1201	1163	291	50
Zr	22	5	26	39	27
Nb	1.1	0.5	0.9	1.3	1.2
La	1.8	0.8	1.5	1.5	3.3
Sample ID	**H11-13C-376.5**	**H11-13C-378.7**	**H11-13C-387.2**	**H11-16-396.4**	**H11-16-399.1**
DDH/Trench	H11-13C	H11-13C	H11-13C	H11-16	H11-16
Lithology	Exhalite	Exhalite	Exhalite	Komatiite	Graphitic Argillite
Lab	GeoLabs	GeoLabs	GeoLabs	Acme	GeoLabs
SiO_2	9.10	29.77	41.73		33.97
TiO_2	0.01	0.50	0.17	0.34	0.15
Al_2O_3	0.19	17.01	4.64	6.35	3.83
$Fe_2O_3^T$	62.19	32.31	37.44	10.55	34.83
MgO	1.04	2.60	2.43	15.46	0.23
MnO	0.86	1.01	1.47	0.26	0.02
CaO	2.74	7.10	4.61	13.67	0.85
Na_2O	0.06	0.39	0.05	0.01	0.09
K_2O	0.03	0.93	0.03	bdl	1.15
P_2O_5	0.01	0.03	0.05	0.03	0.03
LOI	23.1	4.9	5.9		24.7
S	41.1	1.5	10.6	3.4	30.5
Ti	60	2733	921		849
Ni	51	30	41	849	255
Zr	bdl	144	50	24	41
Nb	0.1	5.9	1.9	0.7	1.7
La	2.2	19.0	8.7	1.4	6.8

Table 4: continued.

Sample ID	H11-16-411.4	H11-16-480.6
DDH/Trench	H11-16	H11-16
Lithology	Exhalite	Graphitic Argillite
Lab	GeoLabs	GeoLabs
SiO_2	86.23	60.43
TiO_2	0.01	0.36
Al_2O_3	0.08	11.78
$Fe_2O_3^T$	10.93	15.10
MgO	1.00	0.61
MnO	0.45	0.07
CaO	1.19	4.91
Na_2O	0.04	0.43
K_2O	0.02	1.52
P_2O_5	0.01	0.08
LOI	-0.8	4.6
S	0.3	6.3
Ti	30	1986
Ni	7	145
Zr	bdl	117
Nb	0.1	4.7
La	1.4	11.7

bdl = below detection limits

Whole rock geochemistry data. Ti, Ni, Zr, Nb, and La are in ppm, all others are in weight %.

Table 5: Stable isotope data for the Hart deposit.

SAMPLE ID	DDH/TRENCH	$\Delta^{33}S_{V\text{-}CDT}$	$\Delta^{34}S_{V\text{-}CDT}$	$\Delta^{33}S$	$\delta^{56/54}Fe_{IRMM\text{-}14}$
		±0.3 (2σ)	±0.3 (2σ)	±0.02 (2σ)	±0.06 (2σ)
H07-10-109.45	H07-10	-3.4	-5.7	-0.51	-0.88
H07-10-32.1	H07-10				0.02
H07-10-65.3	H07-10	1.2	1.1	0.61	-0.33
H07-10-66.35	H07-10	0.1	3.0	-1.37	-2.04
H07-10-73.6	H07-10	-3.4	-5.6	-0.55	-1.80
H07-10-86.85	H07-10	-3.1	-4.9	-0.54	-1.91
H07-33-128.3	H07-33	0.6	1.3	-0.09	0.10
H07-33-128.3	H07-33				0.07
H07-33-158.6	H07-33	-0.1	0.9	-0.54	0.10
H07-33-193.7	H07-33				-0.03
H07-33-234.7	H07-33	-0.5	0.1	-0.51	0.05
H07-33-251.2	H07-33	-0.6	0.0	-0.59	0.10
H07-33-251.2	H07-33				0.12
H07-33-261.3	H07-33	-0.9	-0.7	-0.53	
H07-56-182	H07-56	0.0	1.1	-0.61	-0.08
H07-56-188.9	H07-56	-0.6	0.7	-0.95	-1.63
H07-56-210.6	H07-56	0.5	2.4	-0.70	-2.13
H08-106-75.9	H08-106	0.0	0.3	-0.15	0.04
H08-106-93.65	H08-106	-0.7	-0.6	-0.39	-0.11
H08-106-98.6	H08-106	0.6	2.4	-0.69	
H08-80-103.2	H08-80	-2.5	-4.1	-0.42	-1.60
H08-80-107.5	H08-80	-4.4	-7.6	-0.54	-1.60
H08-80-110.6	H08-80	-2.6	-3.8	-0.67	-1.08
H08-80-112.5	H08-80	-0.5	0.3	-0.66	-1.36
H08-80-114.25	H08-80	-2.4	-3.4	-0.65	-1.47
H08-80-126.45	H08-80	-1.5	-1.6	-0.71	
H08-80-126.45	H08-80				-0.03
H08-80-134.65	H08-80	-2.0	-2.5	-0.66	-1.23
H08-80-134.65	H08-80				-1.30
H08-80-136	H08-80	-2.1	-2.9	-0.63	-1.03
H08-80-139	H08-80	-0.3	0.2	-0.39	-0.47
H08-80-77.85	H08-80	-1.2	-1.5	-0.43	-0.03
H08-80-77.85	H08-80				-0.03
H08-80-97.3	H08-80	-0.4	0.2	-0.56	-0.07
H08-80-97.3	H08-80				-0.06
H08-96-259.6	H08-96	-0.6	0.0	-0.55	-0.03
H08-96-274.4	H08-96	-0.5	0.3	-0.69	-0.46
H08-96-277.8	H08-96	-0.5	0.3	-0.69	-0.66
H08-96-281	H08-96	-0.5	0.3	-0.65	-0.19
H08-96-283.8	H08-96	-1.0	-0.7	-0.67	0.15

Table 5: continued.

SAMPLE ID	DDH/TRENCH	$\Delta^{33}S_{V\text{-}CDT}$	$\Delta^{34}S_{V\text{-}CDT}$	$\Delta^{33}S$	$\delta^{56/54}Fe_{IRMM\text{-}14}$
		±0.3 (2σ)	±0.3 (2σ)	±0.02 (2σ)	±0.06 (2σ)
H11-05-39.65	H11-05	-2.0	-2.8	-0.57	
H11-05-45.55	H11-05	-5.2	-9.0	-0.58	-1.22
H11-05-54.25	H11-05	2.1	5.5	-0.74	-1.40
H11-05-57.1	H11-05	-2.5	-3.7	-0.61	-1.30
H11-05-58.55	H11-05	-3.5	-5.8	-0.56	-0.64
H11-05-61.1	H11-05	-2.2	-3.0	-0.63	-0.28
H11-05-62.35	H11-05				-0.82
H11-05-62.6	H11-05	-2.4	-3.4	-0.63	-0.79
H11-05-62.9	H11-05	-0.9	-0.8	-0.51	-0.93
H11-05-68	H11-05	0.3	1.5	-0.50	-0.37
H11-08-10.45	H11-08	-1.8	-2.8	-0.40	-0.01
H11-08-52.65	H11-08	-6.3	-11.4	-0.46	-2.04
H11-08-58.3	H11-08	-5.3	-9.3	-0.45	-1.75
H11-08-63.9	H11-08	3.2	7.6	-0.66	
H11-08-79.4	H11-08	-1.3	-1.5	-0.49	-0.74
H11-11-294.5	H11-11				0.04
H11-11-337.7	H11-11	-0.2	0.9	-0.64	-0.03
H11-11-352.6	H11-11	-0.1	1.2	-0.72	0.10
H11-11-356.55	H11-11	0.2	1.7	-0.71	0.14
H11-11-367.2	H11-11	0.0	1.2	-0.58	
H11-11-407	H11-11	-0.1	1.0	-0.65	-0.01
H11-13C-265.85	H11-13C	-0.1	0.6	-0.41	0.10
H11-13C-282.8	H11-13C	-0.2	0.9	-0.62	-0.11
H11-13C-301.6	H11-13C	0.4	1.1	-0.14	0.00
H11-13C-329.3	H11-13C	1.0	1.1	0.47	0.02
H11-13C-339.1	H11-13C	0.3	-0.1	0.32	0.01
H11-13C-349.6	H11-13C				-0.07
H11-13C-357.1	H11-13C	0.9	3.5	-0.94	-1.86
H11-13C-363	H11-13C	0.6	2.1	-0.46	-1.36
H11-13C-376.5	H11-13C	-3.4	-5.2	-0.75	-1.90
H11-13C-378.7	H11-13C	0.6	2.6	-0.79	-1.73
H11-13C-387.2	H11-13C	-0.5	-0.3	-0.34	-1.96
H11-13C-389.45	H11-13C	-0.4	0.2	-0.43	-2.08
H11-16-396.4	H11-16	2.1	3.3	0.41	0.00
H11-16-399.1	H11-16	0.6	1.6	-0.19	-1.96
H11-16-411.4	H11-16	-0.1	0.7	-0.44	-0.85
H11-16-425.5	H11-16	-1.4	-1.7	-0.49	-1.45
H11-16-480.6	H11-16	2.3	5.0	-0.28	-1.66
MGH502	MGH502	-6.2	-11.0	-0.53	
MGH600A	MGH600	-2.1	-2.8	-0.66	

Table 5: continued.

SAMPLE ID	DDH/TRENCH	$\Delta^{33}S_{V\text{-}CDT}$	$\Delta^{34}S_{V\text{-}CDT}$	$\Delta^{33}S$	$\delta^{56/54}Fe_{IRMM\text{-}14}$
		±0.3 (2σ)	±0.3 (2σ)	±0.02 (2σ)	±0.06 (2σ)
MGH600B	MGH600	2.1	5.5	-0.73	
MGH600C	MGH600	-2.0	-2.6	-0.61	
MGH600D	MGH600	-2.1	-2.9	-0.62	
MGH600E	MGH600	-1.9	-2.4	-0.62	
MGH600F	MGH600	-1.5	-1.6	-0.64	
MGH600G	MGH600	-1.3	-1.5	-0.59	
MGH601A	MGH601	0.7	1.9	-0.22	
MGH601B	MGH601	-5.8	-10.0	-0.61	
MGH601C	MGH601	-2.3	-3.2	-0.62	
MGH601D	MGH601	-2.7	-4.1	-0.55	

mesh) using an agate puck mill before the pulps were sent to these laboratories for geochemical analysis. At GeoLabs, major element analyses were performed by wavelength dispersive X-ray fluorescence (XRF) using a fused disk method. Total sulfur content was determined by oxidation of sulfur through combustion of the sample in an oxygen-rich environment and SO_2 detection by infrared absorption (LECO elemental analyzer). Trace elements, including the main refractory elements and rare earth elements (REE), were analyzed by inductively coupled plasma mass spectrometry (ICP-MS) following a closed vessel multi-acid digestion. At Acme Labs, concentrations were determined by ICP-MS following a four-acid digestion. One sample (H11-11-407) was analyzed by both labs and showed reproducibility of data between the two laboratories.

3.5.3 Sulfur isotope analysis

Sulfur was extracted from rock powders and converted to Ag_2S in both the SIFIR lab (University of Manitoba) and the Stable Isotope Laboratory of the Department of Earth and Planetary Sciences (McGill University) with a Cr(II) reduction procedure that has been already applied to a range of different types of ore metal sulfides from mafic to ultramafic intrusive systems (Fiorentini et al., 2012b; Hiebert et al., 2013), komatiite-associated Fe-Ni-Cu sulfide mineralization (Konnunaho et al., 2013), volcanic massive sulfide deposits (Sharman et al., 2014), and oxidized intrusion-related gold deposits (Helt et al., 2014). All samples were analyzed at McGill University by first fluorinating the Ag_2S at 225°C in a Ni autoclave under ≈20X stoichiometric excess of F_2 for >9 hours to produce SF_6, which was then purified cryogenically and chromatographically and analyzed on a Thermo Electron MAT 253 mass-spectrometer for multiple sulfur isotope ratios in a dual-inlet mode. The sulfur isotope compositions are reported with respect to the V-CDT scale, on which the $\delta^{34}S$ value of IAEA-S-1 is defined as -0.3‰, and the $\Delta^{33}S$ value is taken to be 0.094‰. Repeat analyses throughout the entire analytical procedure return 2σ uncertainties on $\delta^{34}S$ and $\Delta^{33}S$ values that are <0.3 and <0.02‰, respectively.

3.5.4 Fe ISOTOPE ANALYSIS

Aliquots for Fe isotope analysis and major and trace element analysis were prepared from the remaining material following S isotope analysis by crushing the sample in an agate mortar. The crushed sample was then dissolved in a trace-metal grade HNO_3-HCl acid mixture and evaporated to dryness on a hot plate at 60°C. Complete dissociation and oxidation of Fe was achieved by dissolving this residue in aqua regia and evaporating to dryness on a hot plate again. The dry residue was dissolved in 6N HCl in a heated vessel (40°C), which was agitated by ultrasonication. The solution was then centrifuged to separate, and remove, any C-rich material. Fe was extracted from a volume of solution corresponding to 2500 µg of Fe by Bio-Rad AG-1X8 anion resin, which adsorbs ferric iron to the surface of the resin, in a column. The matrix was then dissolved, and other ions striped from the resin, by passing 20 mL of 6N HCl through the column. Iron was then eluted in a 20 mL bath of 0.12N HCl. This solution was evaporated to dryness and the residue was dissolved with 1% HNO_3 to obtain 5 mL of 500 ppm Fe in solution. Isotopic ratios ($\delta^{56}Fe$ and $\delta^{57}Fe$) were determined with a Thermo Electron Neptune multi-collector inductively-coupled mass-spectrometer (MC-ICP-MS) at PSO in medium-resolution mode, which allows distinction between possible interferences of ArO on ^{56}Fe, ArOH or ^{57}Fe, and ArN on ^{54}Fe (Rouxel et al., 2005). Instrumental bias was corrected using simultaneous measurement of Ni isotopes (^{60}Ni and ^{62}Ni) from an internal standard solution that was introduced into the plasma with the sample. “Sample-standard” bracketing was also used to correct for instrumental mass discrimination and instrumental drift by normalizing the sample to the average value for the standard measured before and after the sample. As the “sample-standard” correction method is prone to matrix effects, the combination of both measurement of Ni isotopes and the “sample-standard” bracketing corrects for this and provides accurate and precise results. Based on duplicated chemical purification and analysis of a reference standard periodically over the life of the lab, the external reproducibility is 0.08‰ for $\delta^{56}Fe$ and 0.11‰ for $\delta^{57}Fe$ values (2σ). Iron isotope values are reported relative to the standard IRMM-14, using the conventional delta notation.

3.6 RESULTS

3.6.1 SULFUR AND IRON ISOTOPES

Isotope results are described separately for lithologies present in the footwall to the komatiite and those hosted within komatiitic flows (Table 5), where the latter have been further subdivided based on the visual estimate of the abundance of sulfide mineralization into barren komatiite (<5% sulfide minerals by volume), disseminated mineralized komatiite (5 – 30%), semi-massive and net-textured sulfide in komatiite (30 – 70%), and massive sulfide in komatiite (>70%).

3.6.1.1 FOOTWALL LITHOLOGIES:

The exhalite shows the largest S isotope variability of any footwall lithology in the Hart area with $\delta^{34}S$ values ranging from -11.4 to 7.6‰, and $\Delta^{33}S$ values ranging from -1.4 to -0.3‰ (Figure 14). The graphitic argillite shows the least variability, with $\delta^{34}S$ values ranging from 1.6 to 5.0‰, and $\Delta^{33}S$ values ranging from -0.9 to -0.2‰. Felsic volcanics have $\delta^{34}S$ values ranging from -5.7 to 1.9‰, and $\Delta^{33}S$ values ranging from -0.5 to -0.2‰. The $\delta^{56}Fe$ values of felsic volcanic rocks range from -0.9 to -0.1‰. Exhalite and graphitic argillite have overlapping ranges of $\delta^{56}Fe$ values, -2.1 to -0.9‰ and -2.0 to -1.7‰, respectively, and show systematically lower $\delta^{56}Fe$ values than the average bulk silicate Earth (Figure 15). The $\delta^{56}Fe$ values of exhalite also show no relationship to the abundance of sulfides.

3.6.1.2 KOMATIITE:

The S isotope compositions of komatiite samples can be generally related to sulfide mineralization, with $\delta^{34}S$ values of mineralized samples ranging from -3.8 to 1.7‰, and $\Delta^{33}S$ values ranging from -0.7 to -0.4‰ (Figure 14b). In general, massive sulfides have the lowest $\delta^{34}S$ and $\Delta^{33}S$ values and samples with disseminated mineralization have negative values close to 0‰, although significant overlap exists. Barren komatiites generally have values close to the mantle range, with $\delta^{34}S$ values ranging from -4.1 to 3.3‰, and $\Delta^{33}S$ values ranging from -0.6 to 0.5‰.

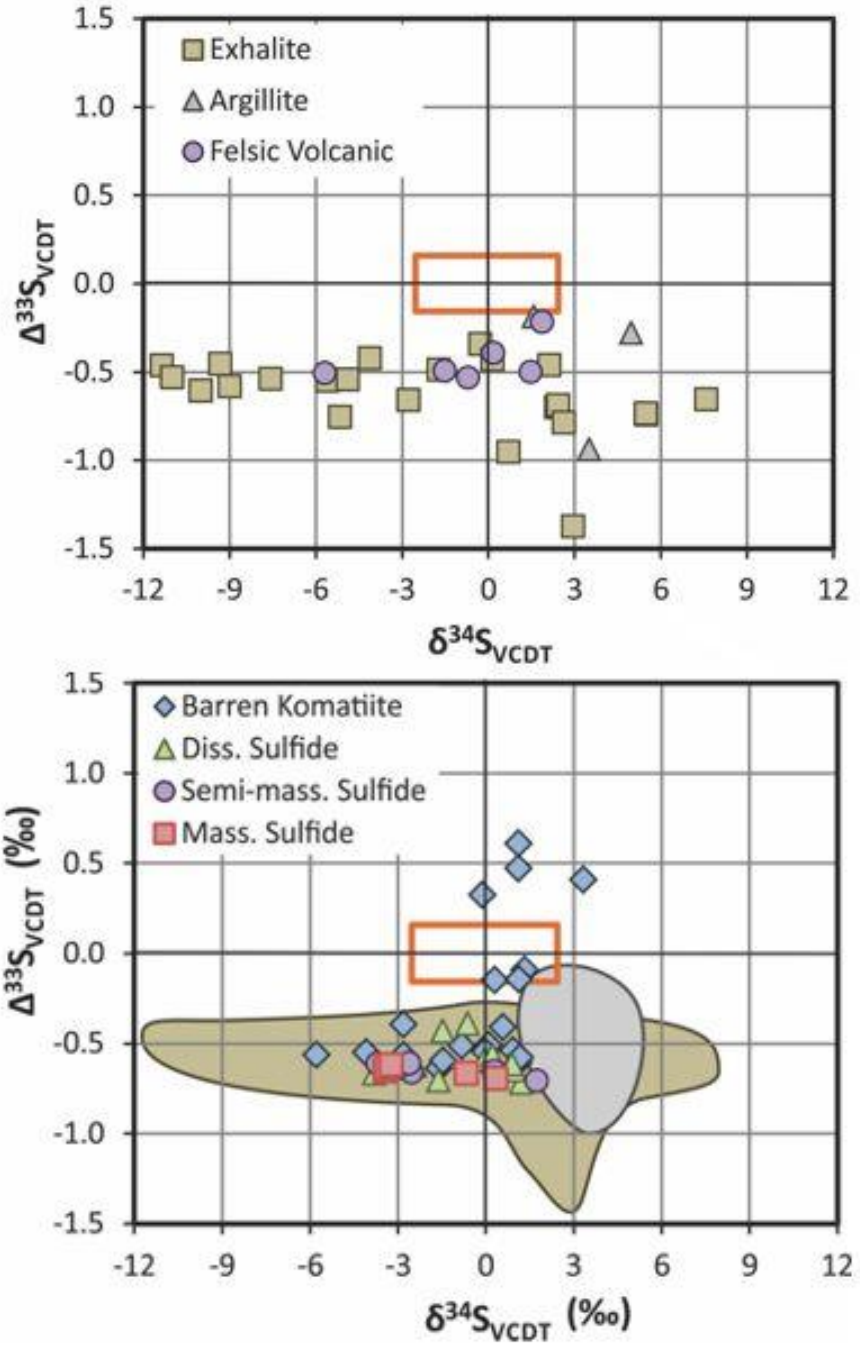

Figure 14: Plot of $\Delta^{33}S$ vs $\delta^{34}S$ values showing the variations in S isotope composition of potential crustal contaminants (a) and komatiite-associated mineralization (b). In (b), exhalite data is represented by the brown field, and graphitic argillite data is represented by the grey field. Orange box represents the range of the mantle values in both (a) and (b) (Bekker et al., 2016).

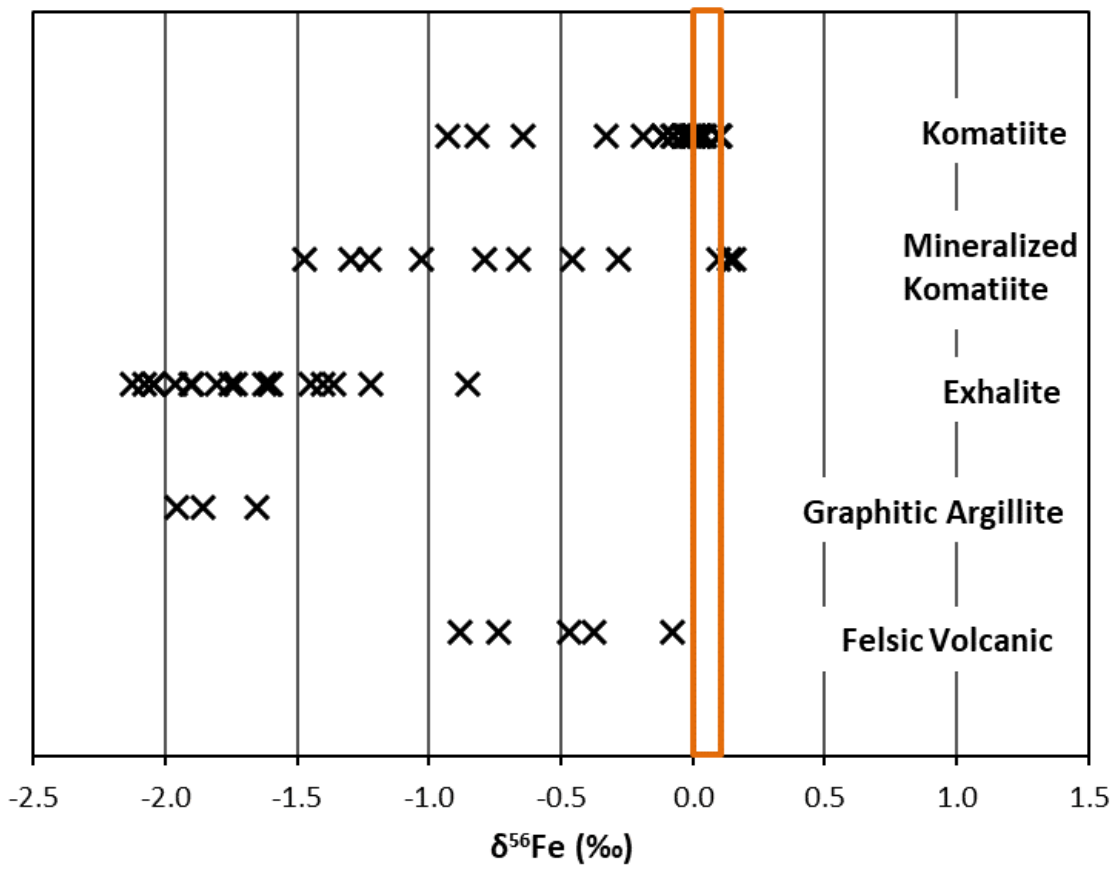

Figure 15: Fe-isotope composition of the lithologies present in the Hart deposit area. Orange rectangle represents the range of the mantle values.

Barren komatiite samples have a narrow range of $\delta^{56}Fe$ values near 0.0‰, similar to near-chondritic Fe isotope composition of the silicate Earth, reflecting minor fractionations during komatiite magma genesis (Dauphas et al., 2010). Mineralized komatiites, however, show significant deviation from mantle values, with $\delta^{56}Fe$ values (-1.5 to 0.2‰) ranging between those of barren komatiite and footwall lithologies (Figure 15). The lowest $\delta^{56}Fe$ values are generally found in massive and semi-massive sulfides in komatiite, whereas disseminated sulfides in komatiite have negative $\delta^{56}Fe$ values close to 0‰, although, as with S isotopes, significant overlap exists.

Samples from the basal flow have $\delta^{34}S$ and $\Delta^{33}S$ values that are lowest close to the mineralization, and trend towards mantle values (0‰) away from the zone of mineralization, both laterally to the west (2100E; Figure 16a), and vertically, towards the top of the flow (Figure 17). To the east of the deposit, komatiite $\delta^{34}S$ values tend to be more positive than those in the mineralized zone. $\Delta^{33}S$ values east of the main zone have a bimodal distribution, with some samples having similar values to the mineralization (approximately -0.5 to -0.6‰), and others having positive $\Delta^{33}S$ values. Although komatiite above the mineralization shows significant overlap with the range of $\delta^{56}Fe$ values observed in mineralization, trends similar to those shown by $\delta^{34}S$ and $\Delta^{33}S$ values are also observed in $\delta^{56}Fe$ data, with values approaching the mantle range both laterally (east and west of the mineralization) and vertically away from the mineralization (Figure 16b).

In the second flow, eastern extension mineralization is characterized by positive $\delta^{34}S$ values and negative $\Delta^{33}S$ values (Figure 16c). These values trend to mantle values laterally to the west (Figure 16c), and vertically, both above and below the mineralization (Figure 17c). Little variability exists in $\delta^{56}Fe$ values for samples from komatiite and mineralization in the second flow, with all values within, or near, the mantle range. In the third flow, $\delta^{34}S$ and $\Delta^{33}S$ values are near 0‰, well within the mantle range (Figure 16d).

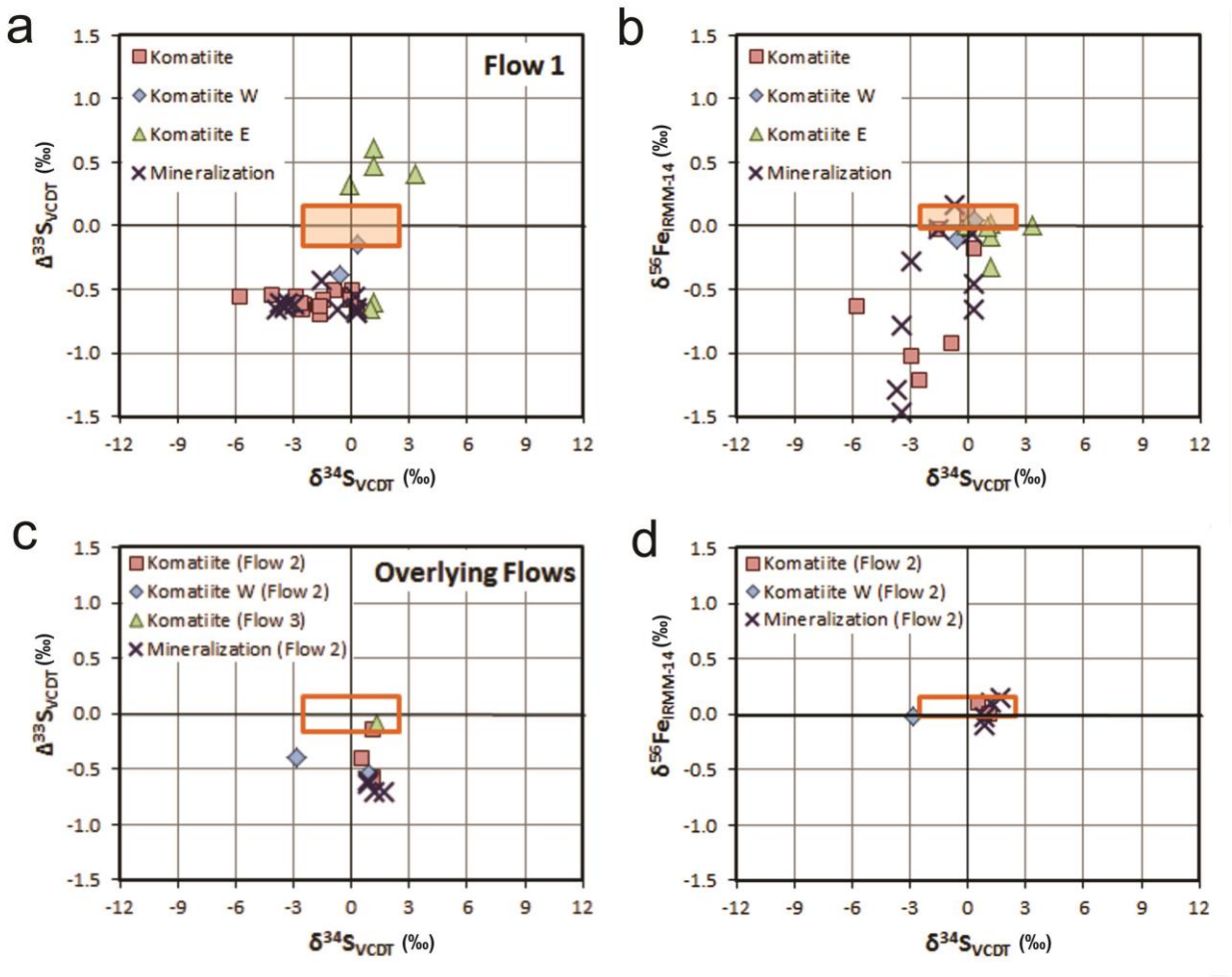

Figure 16: Isotope data for the mineralization and the komatiites (above, east, and west of mineralization) from the different komatiite flows in the Hart area. Mineralization and komatiite data for Flow 1 is from sections 2400E and 2450E; Komatiite E is from sections 2700E and 2900E, and Komatiite W is from section 2100E. Mineralization and komatiite data for the Overlying Flows is from section 2900E; Komatiite W is from sections 2450E and 2700E. See Figure 10 for the location of the sections.

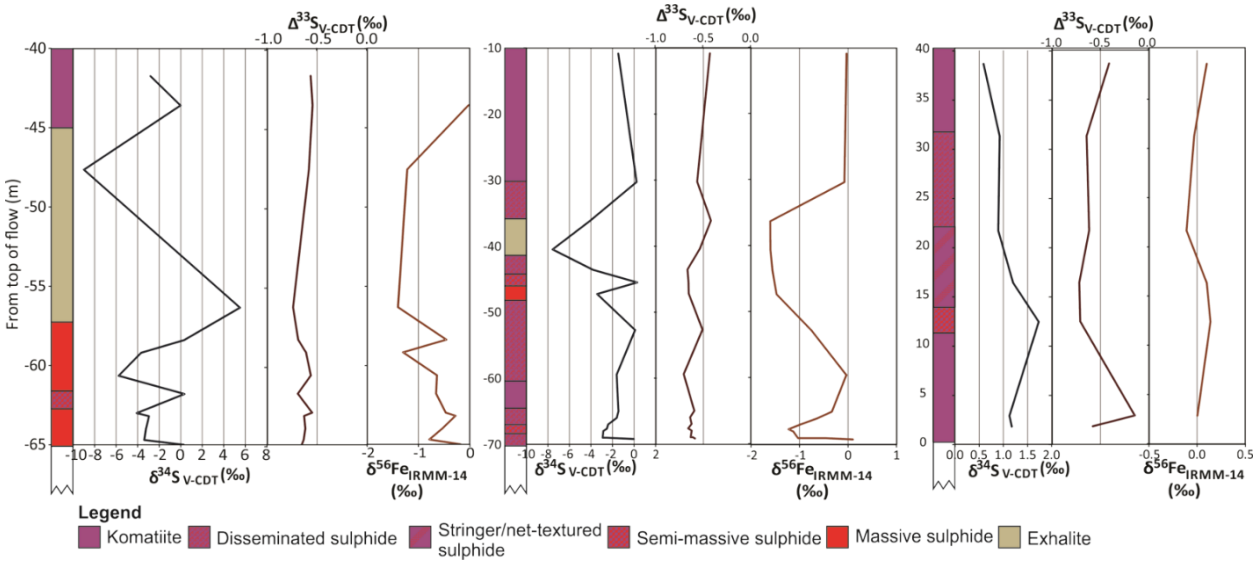

Figure 17: $\delta^{34}S$ and $\delta^{56}Fe$ isotopic profiles through the Main Zone of the basal komatiitic flow along composite sections. **a** 2400E. **b** 2450E, **c** 2900E. Distance from the top of flow is calculated based on the thickness of the flow in sampled drill holes and an approximate dip. See figure 2 for the location of the sections.

3.6.2 Major and trace element geochemistry

The komatiite samples in this study show a wide range of whole-rock compositions that reflects alteration and sulfide accumulation in addition to normal magmatic variability (Table 4). In order to investigate the latter, komatiite compositions were recalculated on a volatile-free basis and only samples with MgO>10%, TiO_2<1.0%, 40%<SiO_2<58%, and S<0.5% were considered. This procedure eliminates samples with composition strongly influenced by sulfides and high degree of alteration as well as those that do not represent true komatiites (Barnes et al., 2007). On a Al_2O_3/(2/3-MgO-FeO) versus TiO_2/(2/3-MgO-FeO) discrimination diagram utilizing mole proportions and designed to be a projection from olivine (Hanski et al., 2001), the Hart komatiite samples plot in both the Al-depleted (Barberton-type komatiites) and Al-undepleted (Munro-type komatiites) fields (Figure 18). Note that Sproule et al. (2005) found Tisdale komatiites, such as those at Hart, to be dominantly Munro-type.

In a review of komatiite-associated ores, Barnes and Fiorentini (2012) compared the range of values for a number of trace-element ratios normalized to the primitive mantle to constrain which of them displays the largest variability in contaminated rocks. For the Abitibi komatiites, ratios of $[Th/Nb]_{MN}$ and $[Zr/Ti]_{MN}$ most consistently showed the signature of crustal contamination (e.g., values >1), when normalized to the primitive mantle values from McDonough and Sun (1995), even though $[Zr/Ti]_{MN}$ has the smallest range of values, and was considered to be the least sensitive of the ratios shown by Barnes and Fiorentini (2012) to indicate contamination. In our study, Th concentrations are commonly below detection limit, so we used La instead, as the $[La/Nb]_{MN}$ ratios have been found to behave similarly to $[Th/Nb]_{MN}$ ratios (Lesher et al., 2001). Most mineralized and barren komatiite samples have $[La/Nb]_{MN}$ and $[Zr/Ti]_{MN}$ ratios above 1, suggesting crustal contamination (Figure 19), although concentrations of both Zr and Ti are low in our samples, potentially resulting in significant errors.

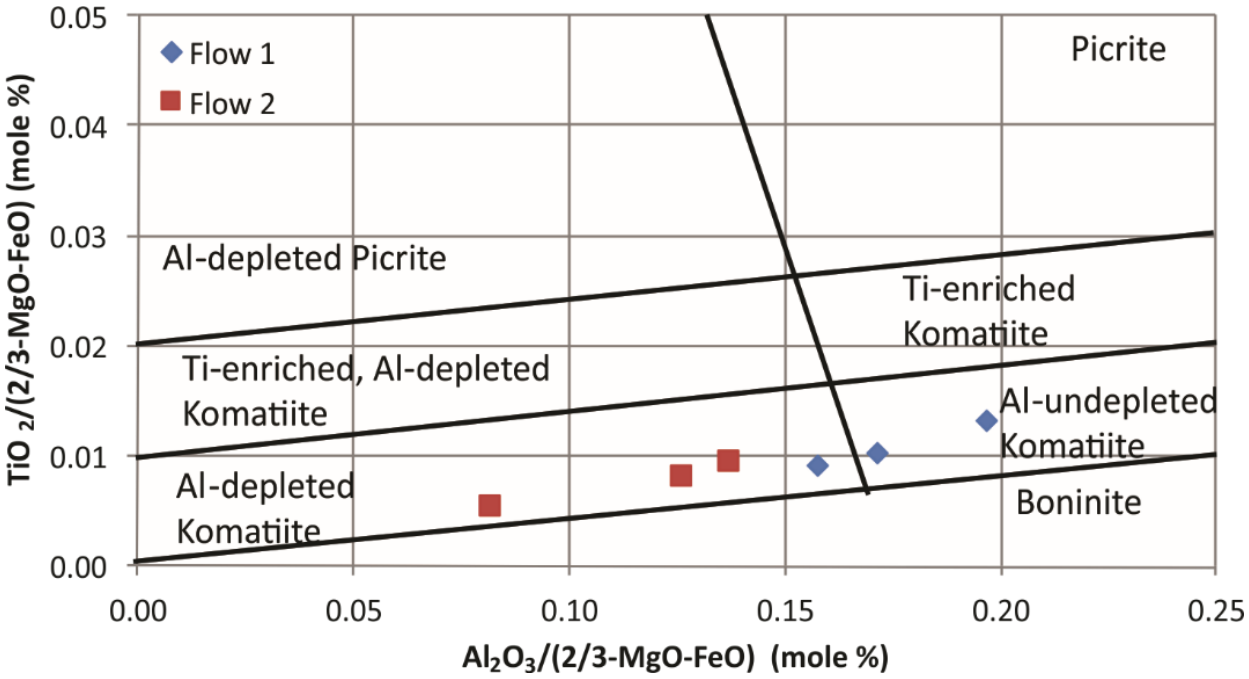

Figure 18: $Al_2O_3/(2/3 - MgO - FeO)$ versus $TiO_2/(2/3 - MgO - FeO)$ discrimination diagram (in mole %) showing chemical affinity of Hart komatiites (after Hanski et al. 2001). Note coexistence of Al-depleted komatiite (Barberton-type) and Al-undepleted komatiite (Munro-type) in the Hart Deposit.

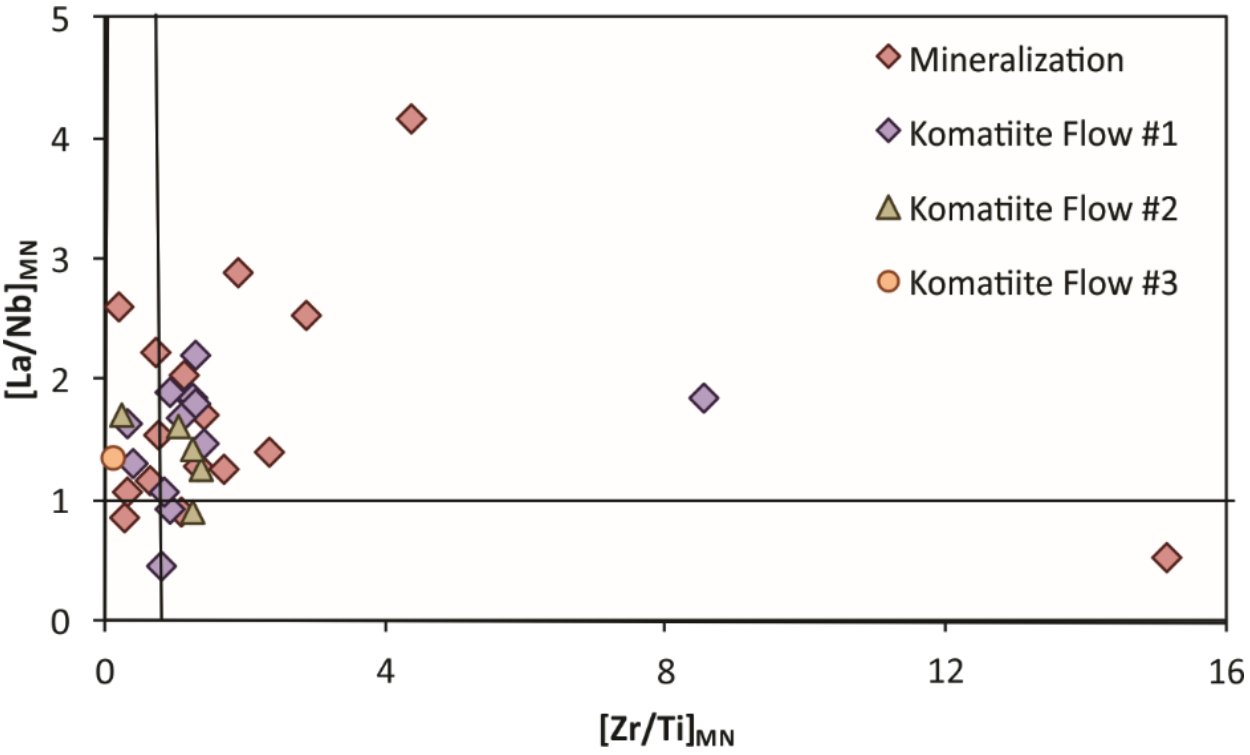

Figure 19: $[La/Nb]_{MN}$ versus $[Zr/Ti]_{MN}$ plot. Values >1 on both axes are interpreted to represent the signature of contamination by crustal material; see text for further details. Mantle values used for normalization are from McDonough and Sun 1995.

3.7 DISCUSSION

Since the $\Delta^{33}S$ and $\delta^{56}Fe$ data are likely to reflect the degree of crustal contamination in the mineralized and barren komatiite samples, these data are compared to the trace element ratios to explore whether any correlation between these two datasets exists (Figure 20). A weak correlation between the trace element ratios and $\delta^{56}Fe$ values (Figures 20a, b), especially for komatiites, for which Fe budget in the bulk samples is not controlled by sulfide abundances, suggests that non-mantle values for both proxies might be related to crustal contamination. However, when compared to $\Delta^{33}S$ values, these trace element ratios exhibit a large range of values, within a limited, and consistently negative, range of $\Delta^{33}S$ values (Figures 20c, d). These consistently non-mantle $\Delta^{33}S$ values formed as a result of crustal contamination, and suggest a small degree of crustal contamination even in samples that do not have $[La/Nb]_{MN}$ and $[Zr/Ti]_{MN}$ ratios above 1.

3.7.1 CONTAMINANT COMPOSITION VS. HIGH-TEMPERATURE FRACTIONATIONS

Prevalent models for the formation of magmatic sulfide deposits suggest that sulfide xenomelt segregates at the base of the magma body during melting and assimilation of the country rock, with an isotopic composition of the original melted material modified by isotope exchange with the magma (Ripley and Li, 2003). Consequently, composition of the contaminant material will have some effect on the isotopic values in the sulfide mineralization. However, fractionation processes during melting, crystallization, and isotope exchange with the silicate melt can also account for some variability in $\delta^{56}Fe$ values. Extremely limited work has been done to assess Fe isotope fractionation between sulfide melts and silicate magmas. Experiments conducted by Schuessler et al. (2007) show that pyrrhotite in equilibrium with a peralkaline rhyolite melt have $\delta^{56}Fe$ values 0.4‰ lower than that of the silicate. However, they suggested that this fractionation factor is dependent on the redox state of the magma, and would likely decrease in more reduced ultramafic magmas (Schuessler et al., 2007). Significant

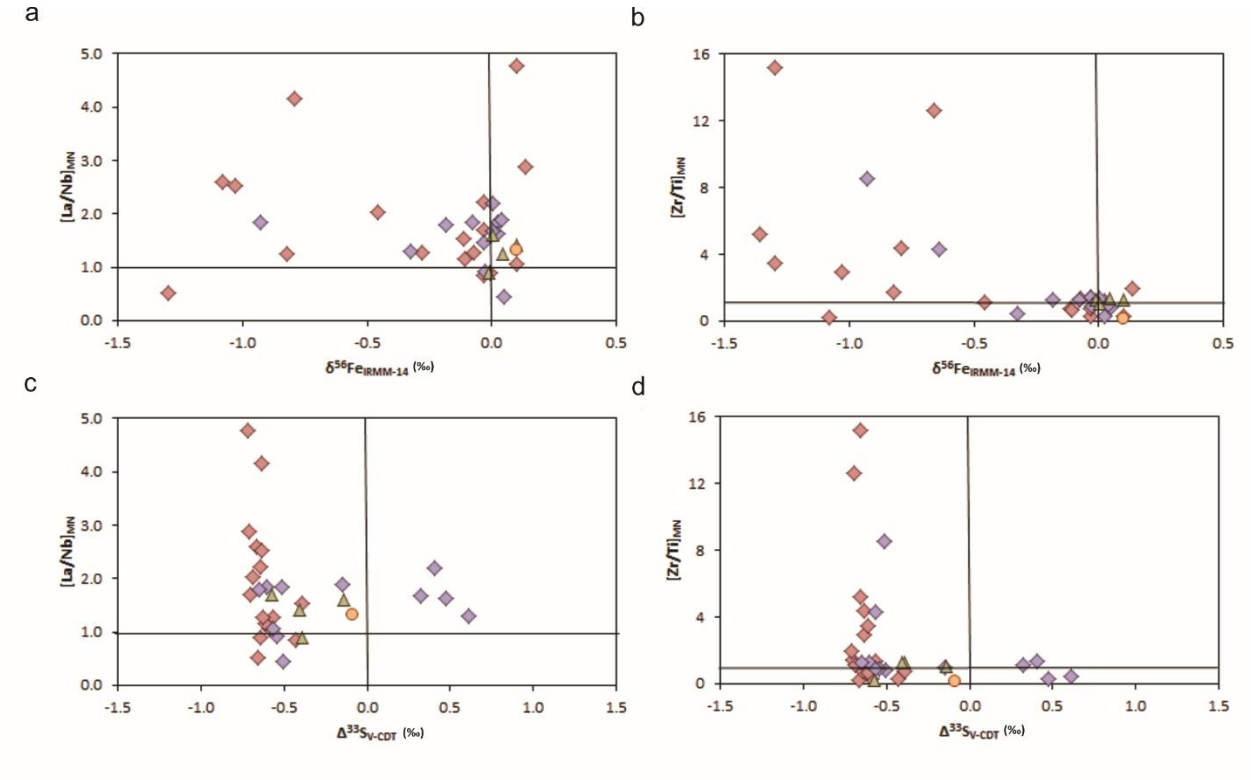

Figure 20: Primitive mantle-normalized trace element ratios versus stable isotope values suggesting contamination with crustal materials for mineralization and some komatiite samples. **a** $[La/Nb]_{MN}$ versus $\delta^{56}Fe$. **b** $[Zr/Ti]_{MN}$ versus $\delta^{56}Fe$. **c** $[La/Nb]_{MN}$ versus $\Delta^{33}S$. **d** $[Zr/Ti]_{MN}$ versus $\Delta^{33}S$. Note that trace element ratios >1 and stable isotope values different from 0‰ are considered to indicate crustal contamination. Legend as in Figure 19.

range of Fe isotope composition has been also reported in komatiite-associated nickel sulfide deposits and Ni-Cu mineralization in mafic to ultramafic intrusions ($\delta^{56}Fe = 0.0 \pm 0.4‰$; Bekker et al., 2009; Fiorentini et al., 2012b; Hofmann et al., 2014).

Crystallization of olivine in basalts has been shown to fractionate Fe isotopes with $\delta^{56}Fe$ values in olivine 0.1 to 0.3‰ lower than in the residual melt (Teng et al., 2008). It is therefore expected that partial melting to produce basaltic magma in the mantle would have a similar effect, with melt $\delta^{56}Fe$ values approximately 0.1‰ higher than those in the residual mantle materials (Williams et al., 2005; Weyer, 2008; Teng et al., 2013). However, a study of Fe isotopes in komatiites has shown that bulk sample $\delta^{56}Fe$ values for komatiite are the same as chondritic values (0.044‰; Dauphas et al., 2010), or slightly lower (-0.66‰; Nebel et al., 2014), suggesting that the high degree of partial melting required to produce komatiite magma minimizes this fractionation effect. Additionally, Dauphas et al. (2010) found no correlation between $\delta^{56}Fe$ values and MgO concentrations, indicating that significant fractionation of Fe isotopes did not occur during crystallization of Mg-rich olivine. This implies that high-temperature magmatic fractionation of Fe isotopes in komatiite is minimal, with only small (<1‰) fractionation between silicate and sulfide melts in this system. We therefore interpret low $\delta^{56}Fe$ values in barren komatiite (down to - 0.9‰) and mineralized komatiite samples (down to -1.5‰) to be due to contamination and isotope exchange with crustal materials, such as exhalite (with $\delta^{56}Fe$ values ranging from -2.1 to -0.9‰) and graphitic argillite (with $\delta^{56}Fe$ values ranging from -2.0 to -1.7‰), and unrelated to intrinsic fractionation within the komatiite system between silicate and sulfide melts at high temperatures. The contamination is more prominent in the mineralized zone due to the crystallization of the first olivine cumulates isolating the sulfide liquid, and the footwall contaminants, from the flowing komatiite above it, and, as the komatiite keeps flowing, the most contaminated komatiite liquid is carried away, while the sulfide melt is trapped in a topographic low beneath the komatiite flow (Lesher and Arndt, 1995).

The potential contaminant that could have acted as dominant sulfur source for the Hart deposit has been previously interpreted to be the exhalite unit due to the relative abundance of S in the exhalite compared to the felsic volcanic rocks, and the location of mineralization where the exhalite unit is significantly thinned or entirely removed by thermomechanical erosion (Houlé et al., 2010b). However, the recent discovery of significant concentrations of sulfides in the graphitic argillite unit provides another viable sulfur source for the formation of this deposit. To distinguish between these two potential sulfur sources, we use $\delta^{34}S$, $\Delta^{33}S$, and $\delta^{56}Fe$ values to constrain the isotopic signatures of these footwall lithologies for comparison to the signatures observed in the komatiite and associated mineralization.

Two isotopically distinct S pools that formed through photochemical reactions in the Archean oxygen-poor atmosphere have been identified: 1) a reduced pool with positive $\Delta^{33}S$ values, and 2) an oxidized pool with negative $\Delta^{33}S$ values (Farquhar et al., 2002; Ono et al., 2003). The reduced pool is inferred to have reacted with Fe^{2+} dissolved in the anoxic seawater and precipitated as disseminated Fe-sulfide in sediments (Ono et al., 2009; Maynard et al., 2013; Marin-Carbonne et al., 2014). The oxidized pool is thought to have been reduced by bacterial sulfate reduction and incorporated into paleosols on the continents (Maynard et al., 2013), or added to the oceans as dissolved sulfate (Farquhar et al., 2002). Once dissolved in the oceans, sulfate was reduced via bacterial metabolism to form pyrite nodules in organic matter-rich sediments during diagenesis, or cycled through submarine hydrothermal systems and was eventually deposited on the ocean floor forming barren massive sulfide lenses distally or volcanogenic massive sulfide deposits proximally to hydrothermal centres (e.g., Bekker et al., 2009). However, the slightly positive $\delta^{34}S$ values of the Archean seawater sulfate could be modified by mass-dependent fractionation, for example via bacterial or thermogenic sulfate reduction. This would produce nodules or layers of sulfides in sediments with consistently negative $\Delta^{33}S$ values, but highly

variable $\delta^{34}S$ values, reflecting S source from dissolved seawater sulfate (cf. Ono et al., 2003; 2009), as seen in the data from the exhalite (Figure 21).

Fe isotope fractionation is thought to be dominantly controlled by redox reactions, with igneous rocks having values between 0.0 and 0.1‰, and subsequent weathering and low-temperature, surface reactions resulting in a range of $\delta^{56}Fe$ values that depends on the extent, and process, of alteration (Rouxel et al., 2003). Circulation of submarine hydrothermal fluids along mid-oceanic ridges results in fluids having negative to 0‰ $\delta^{56}Fe$ values (as low as -0.9‰; Beard et al., 2003; Rouxel et al., 2008; Bennett et al. 2009). As a result, Fe-sulfides that precipitate from these hydrothermal fluids have similarly negative $\delta^{56}Fe$ values as low as -2‰ (Rouxel et al., 2008). Fe oxides and hydroxides that precipitated Fe added to the oceans by hydrothermal fluids form iron formations that tend to have relatively high $\delta^{56}Fe$ values (Dauphas et al., 2004; Rouxel et al., 2005; Planavsky et al., 2012; Moeller et al., 2014), although isotopically light compositions have been also reported in oxide-facies BIF (Bekker et al., 2010; Planavsky et al., 2012). The residual Fe in seawater could then precipitate as sulfide with $\delta^{56}Fe$ < 0‰ (Rouxel et al., 2005; Guilbaud et al., 2011).

The negative $\Delta^{33}S$ values of both the exhalite and graphitic argillite at the Hart deposit suggest that sulfides in both lithologies formed as a result of bacterial reduction of Archean seawater sulfate (Figure 20). The $\Delta^{33}S$ values of the exhalite and graphitic argillite do not provide an adequate means of distinguishing between these potential sulfur sources for the komatiite sulfides. Additionally, the negative values of $\delta^{56}Fe$ in exhalite (average: -1.9 ± 0.06‰) and graphitic argillite (average: -1.8 ± 0.06‰) also do not differentiate between these two lithologies. Notably, the average values of $\delta^{34}S$ are distinct between exhalite (-2.1‰) and graphitic argillite (+3.4‰), although the range of values for the exhalite (-11.4 to +7.6‰) overlaps with that of the graphitic argillite (+1.6 to +5.0‰).

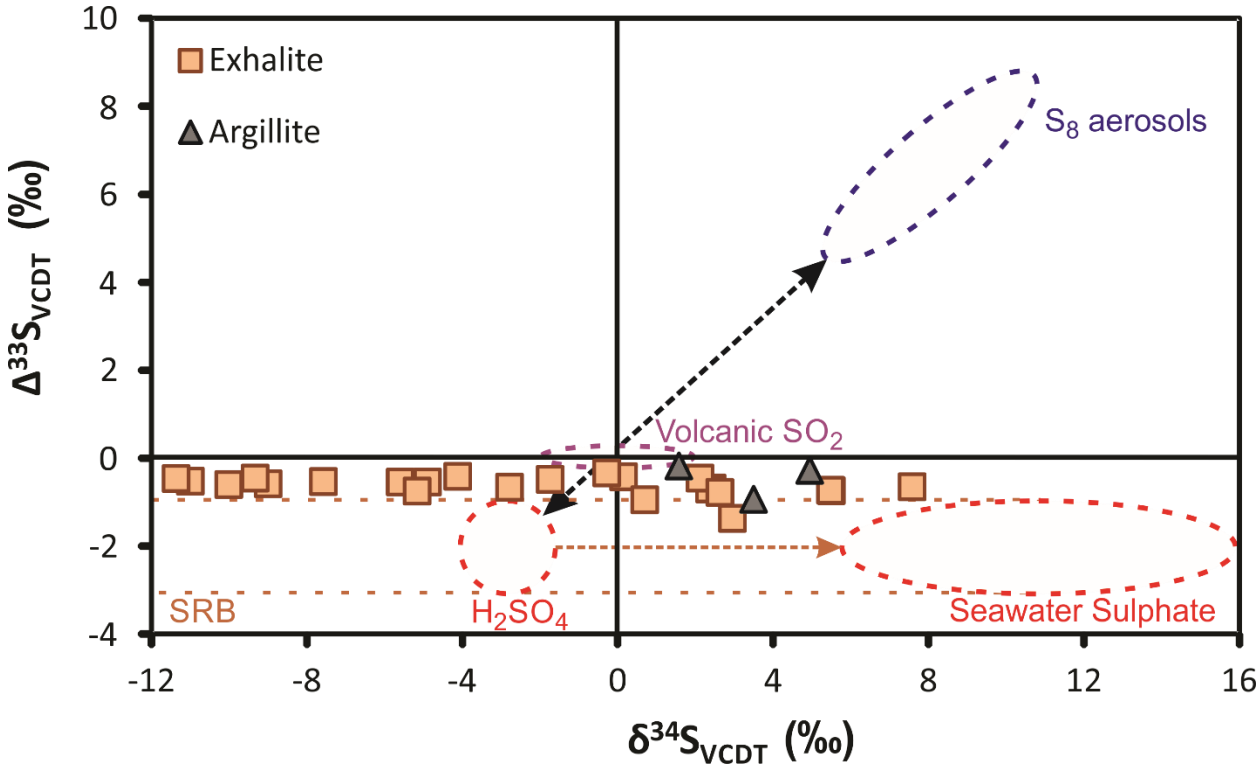

Figure 21: Broadly defined fields of $\Delta^{33}S$ and $\delta^{34}S$ values for the different volcanic, atmospheric, and seawater S pools in the Archean suggesting that sulfides in exhalite and graphitic argillite originated via bacterial reduction of seawater sulfate (SRB). Purple oval represents composition of mantle-derived volcanic sulfur; blue oval and red circle represent composition of S_8 and SO_4^{2-}, respectively, formed by photochemical reactions in the atmosphere and delivered with aerosols to seawater. Orange dashed line represents the most likely range in composition of sulfides formed by sulfate-reducing bacteria that resulted in a horizontal shift in seawater sulfate composition (red oval) to higher $\delta^{34}S$ values (fields are after Ono et al. 2003).

The exhalite is characterized by negative $\Delta^{33}S$ values, negative $\delta^{56}Fe$ values, and $\delta^{34}S$ values that range from positive to negative. The graphitic argillite also has negative $\Delta^{33}S$ and $\delta^{56}Fe$ values, but always has positive $\delta^{34}S$ values. Therefore, consideration of these three isotopic tracers might provide a signature to identify the dominant contaminant that contributed to sulfur saturation in the komatiite at the Hart deposit.

3.7.1.1 Significance of negative $\delta^{56}Fe$ values in exhalite and graphitic argillite

Negative, and highly variable, $\delta^{56}Fe$ values are relatively common in sulfides from Archean organic matter-rich sediments (Rouxel et al., 2005). Precipitation of Fe-sulfides from Fe^{2+} dissolved in an aqueous solution has been shown to produce fractionations between -0.3 and -0.9‰ in the temperature range of 2 to 40°C (Butler et al., 2005), although even larger fractionations (-2.5‰ between pyrite and Fe^{2+}) have been shown by kinetic experiments (Guilbaud et al., 2011). Under hydrothermal conditions, non-equilibrium Fe isotope fractionation between pyrite in hydrothermal chimneys and hydrothermal fluid has been found to be about -0.9‰ (Rouxel et al. 2008). Hence, in order to account for the values observed in this study (-2.0‰ in graphitic argillite and -2.1‰ in exhalite), an additional pathway is likely required to lower the $\delta^{56}Fe$ value of the water prior to precipitation of Fe-sulfide. Two mechanisms have been proposed to produce isotopically light Fe^{2+} in solution, which might be archived in Archean sedimentary rocks: dissimilatory iron reduction (DIR) in pore waters by bacteria (Yamaguchi et al., 2005; Archer and Vance, 2006), and reservoir effects (e.g. Rayleigh fractionation) involving the precipitation of isotopically heavy Fe-oxides (Rouxel et al., 2005; Planavsky et al., 2012). We infer the latter mechanism for the origin of very low Fe isotope values in the graphitic argillite and exhalite in our study due to the presence of iron formation at the same stratigraphic level as the exhalite in the Hart deposit area.

3.7.1.2 Isotopic variations within komatiitic flows

Since we have established typical isotopic signature of the two most likely sulfur sources in the vicinity of the Hart deposit, isotope ratios of the mineralization and associated komatiite might identify which of the footwall lithologies was responsible for providing sulfur to form the deposit. The isotope signatures ($\Delta^{33}S$, $\delta^{34}S$, and $\delta^{56}Fe$) observed in komatiites and the associated mineralization at Hart deposit can be clustered into four main groups, each associated with a unique location (Figure 22).

Barren komatiite of the third flow, which is not associated with significant sulfide mineralization, is characterized by near mantle values of $\delta^{34}S$, $\delta^{56}Fe$, and $\Delta^{33}S$, and trace element concentrations showing no evidence of contamination. In contrast, the main zone of mineralization, in the central part of the basal embayment, is characterized by negative $\Delta^{33}S$, $\delta^{34}S$, and $\delta^{56}Fe$ values. These values are generally lowest where mineralization is most abundant, gradually increasing towards 0‰ above the mineralization and laterally to the west of the main zone (Figs. 16a, b, 17a, b and 22). This isotopic signature is most consistent with the dominant crustal contaminant for the main zone mineralization being the exhalite.

The eastern extension of sulfide mineralization (Figure 22) is characterized by negative $\Delta^{33}S$, positive $\delta^{34}S$, and slightly negative to near zero $\delta^{56}Fe$ values (Figs. 16c, d, 17c and 22). This isotopic signature is more characteristic of the graphitic argillite as the dominant crustal contaminant, once the effect of isotope exchange is taken into account. As no graphitic argillite has been observed between the first and second komatiite flows, it is likely that the second flow completely assimilated an interflow graphitic argillite unit as a result of thermomechanical erosion. Alternatively, this komatiitic flow may have been in direct contact with a graphitic argillite unit upstream from the present location of the mineralization. Both scenarios are plausible, as thick komatiite flows are known to be capable of extensive

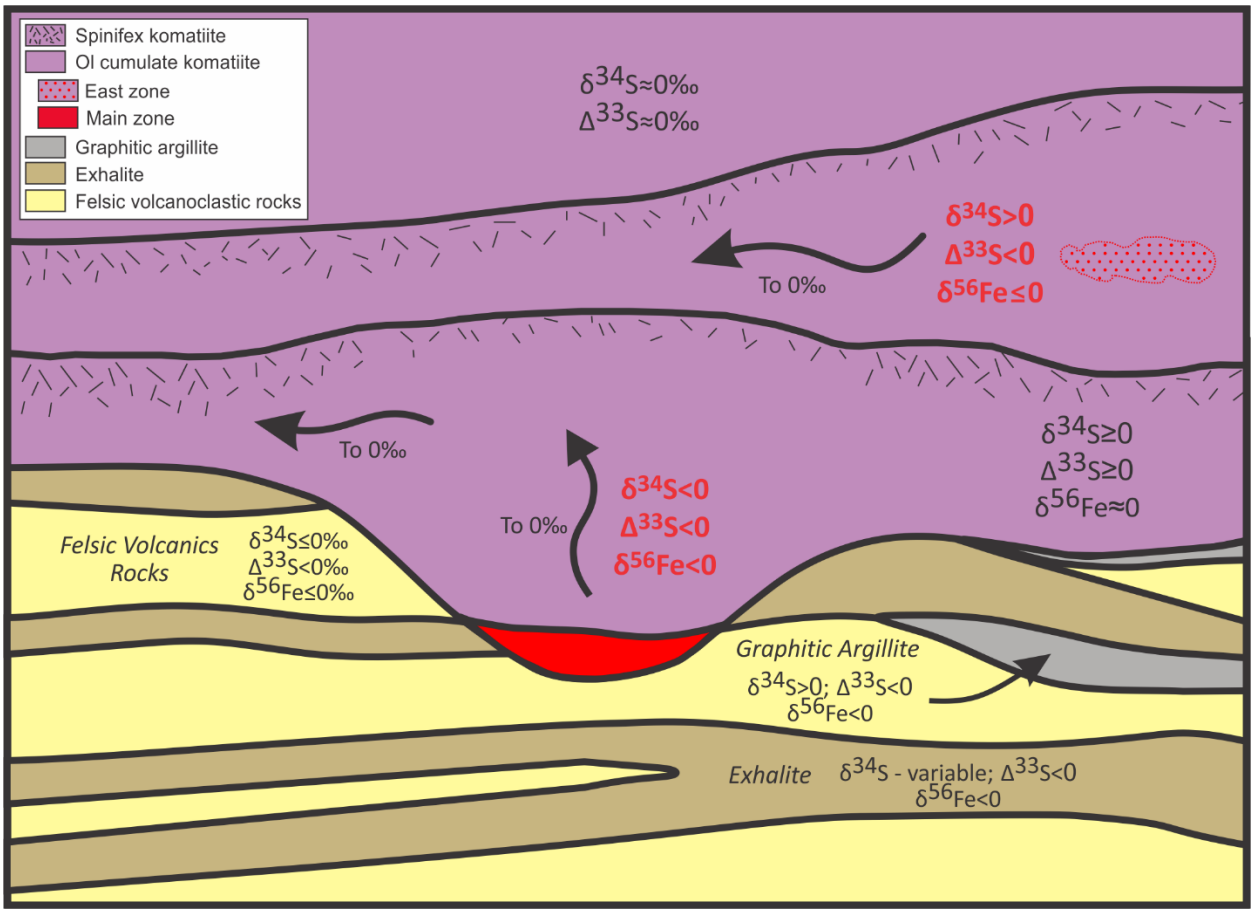

Figure 22: Schematic cross-section through the Hart deposit (facing north), showing general trends in isotopic data.

Geology is based on drill hole logs and correlation among sampled drill holes.

thermomechanical erosion, and mineralization within a komatiitic flow could be deposited relatively far from the site of assimilation (Lesher and Campbell, 1993; Arndt et al., 2008; Barnes et al., 2013).

An additional isotopic signature is present in the barren komatiite of the basal flow east of the main zone (Figure 21), where only trace amounts up to ~3% of sulfides by volume are present. This pattern is characterized by slightly positive $\Delta^{33}S$ and $\delta^{34}S$, and $\delta^{56}Fe$ values near 0‰. Although most of the $\delta^{34}S$ values fall within the expected mantle range of approximately 0 ± 2‰ (Chaussidon et al., 1989; Labidi et al., 2012; 2013; 2015; Bekker et al., 2016), this represents a definite shift from dominantly negative $\delta^{34}S$ values, elsewhere in the basal komatiite flow, to dominantly positive $\delta^{34}S$ values in the eastern area. Considering the positive $\Delta^{33}S$ values, this may be due to local assimilation of early diagenetic sulfide that had been formed through reduced atmospheric sulfur reacting with Fe present in seawater and precipitating as disseminated Fe-sulfide in shale (Marin-Carbonne et al., 2014). This could have resulted in a small amount of assimilated sulfur, insufficient to produce a sulfide xenomelt at the base of the molten komatiite, but sufficient to preserve the signature of this local contaminant when sulfur saturation was reached in the late stages of fractional crystallization of the komatiite lava. Alternatively, this could represent the remnant isotopic signature after the majority of komatiite melt and possible sulfide xenomelt have been flushed downstream. Different isotopic signatures of, and correspondingly S sources for, the basal flow mineralization and the zone immediately east of the mineralization emphasize a local S source for minor amounts of mineralization, which might not have exchanged with the rest of the komatiite flow.

Considering the low sulfur content of komatiite in the area to the east of the basal flow mineralization, it seems likely that only assimilation of organic matter-rich shales with pyrite nodules would result in an economic-grade mineralization, unless massive sulfides deposited from submarine hydrothermal fluids were present in the footwall. Both these lithologies would have negative to near zero $\Delta^{33}S$ values. The

negative $\Delta^{33}S$ signature in mineralization and komatiite therefore does indicate presence of favourable environmental conditions and lithologies in the footwall for generation of economic-grade mineralization in komatiites.

3.7.2 R FACTOR AND ISOTOPE EXCHANGE

Silicate to sulfide mass ratio plays important role in controlling the chemical composition and isotopic ratios in sulfide mineralization (Lesher and Burnham, 2001; Ripley and Li, 2003). Calculations of R factor are based on simple mass-balance equations, and can be expressed as mixing models (Lesher and Burnham, 2001), or isotope exchange equations (Ripley and Li, 2003). As such, we use the following equation from Ripley and Li (2003) for R factor calculations, involving isotopes:

$$\delta_m = \frac{\delta_{sul} + R^0(\delta_{sil} - \Delta\epsilon_{sul,sil})}{1 + R^0} \quad (8)$$

where δ_m is the isotope ratio of the sulfide product after isotope exchange with the silicate melt, δ_{sul} and δ_{sil} are the initial isotope ratios of sulfide and silicate melts, respectively, $\epsilon_{sul,sil}$ represents the sulfide-silicate fractionation factor at the appropriate temperature, and $R^0=(C_{sil}/C_{sul})*R$, where C_{sil} and C_{sul} are S concentrations in initial silicate and sulfide melts, respectively, and R is the silicate to sulfide mass ratio. For high-temperature magmatic processes, $\epsilon_{sul,sil}$ for S isotopes is expected to be close to 0‰ (Ripley and Li, 2003). For Fe isotopes, however, there may exist a small fractionation between sulfide and silicate melts that might be significant for the range of Fe isotope values observed at the Hart deposit. As already discussed above, Schuessler et al. (2007) found a $\delta^{56}Fe$ fractionation factor of 0.38‰ between pyrrhotite and silicates for a peralkaline rhyolite melt. They attributed most of the fractionation to redox reactions and suggested that the fractionation may approach 0‰ in completely reduced magmas. As such, we estimate $\epsilon_{sul,sil}$ = 0.05‰ from the initial to allow for a small fractionation at the high magmatic temperatures and reducing conditions thought to exist in komatiite magma, which has an initial $\delta^{56}Fe$ value of 0.044‰ (Dauphas et al., 2010). R factors were calculated using Ni

concentrations with the magma mixing equation (Lesher and Burnham, 2001). In this case, Ni concentrations were recalculated to 100% sulfide using the method described by Kerr (2003). Since there is a large range of $\delta^{34}S$ values in exhalite, only $\Delta^{33}S$ and $\delta^{56}Fe$ values were used in R factor calculations, as local variations in $\delta^{34}S$ values in the footwall would have a large impact on the average value adopted for the sulfide mineralization, complicating R factor calculations. The similar values of $\Delta^{33}S$ and $\delta^{56}Fe$ for exhalite and graphitic argillite allow the use of a composite value as the initial sulfide value in these calculations. Initial values for Fe and S concentrations in sulfide are based on a mixture of 60% pyrrhotite and 40% pyrite, which reflects the approximate proportions found in the footwall rocks, and concentrations in silicate are based on average Fe and S concentrations in unmineralized komatiite samples, although the initial S concentration of 800 ppm is slightly higher than the initial S concentrations that have been typically suggested for komatiites of ~500 ppm (e.g. Lesher and Burnham, 2001; Arndt et al., 2008). Initial $\Delta^{33}S$ and $\delta^{56}Fe$ values for the komatiite are based on previous work by Bekker et al. (2009). All variables used in R-factor modelling are found in Table 6.

Many studies of komatiite-associated Ni-sulfide deposits have reported a wide range of R factor values from 10 to >500, calculated mainly through the use of Ni, Cu, and PGE concentrations in the ores (Arndt et al. 2008). Estimates of R factor using $\delta^{56}Fe$ and $\Delta^{33}S$ tracers produce values that vary from 5 to 250, with the higher R factor values common to disseminated sulfide and weakly mineralized komatiite relative to massive and semi-massive, sulfide mineralization (Figure 23a). Mineralized samples from the eastern extension generally have $\delta^{56}Fe$ values close to 0‰, compared to the more negative $\delta^{56}Fe$ values for the main zone, suggesting a slightly higher R factor for the eastern extension. R factors calculated from Ni concentrations vary from 5 to 50, and overlap with the estimates from the Fe and S isotope systems (Figure 23b). This study also emphasizes the value of using multiple methods to estimate R factor as proxies such as $\delta^{56}Fe$ values and Ni concentrations are more sensitive to small R factor values, and show a greater range for the mineralization at the Hart deposit. S isotopes (specifically $\Delta^{33}S$ values)

Table 6: Values for variables used in R factor modelling. See text for further details.

	Δ_{SUL}	Δ_{SIL}	Δ	C_{SIL}	C_{SUL}
$\Delta^{33}S$	-0.62	0.00	0.00	800 ppm	43%
$\delta^{56}Fe$	-1.69	0.044	0.05	10.8%	57%

	100% sulfide[1]	**Initial silicate[1]**	**Distribution coefficient[2]**	**Calculated R**
Ni	N/A	1077 ppm	100	N/A
Pt	222 ppb	8.2 ppb	30000	27

[1]From Barnes and Naldrett (1987).

[2]From Lesher and Burnham (2001).

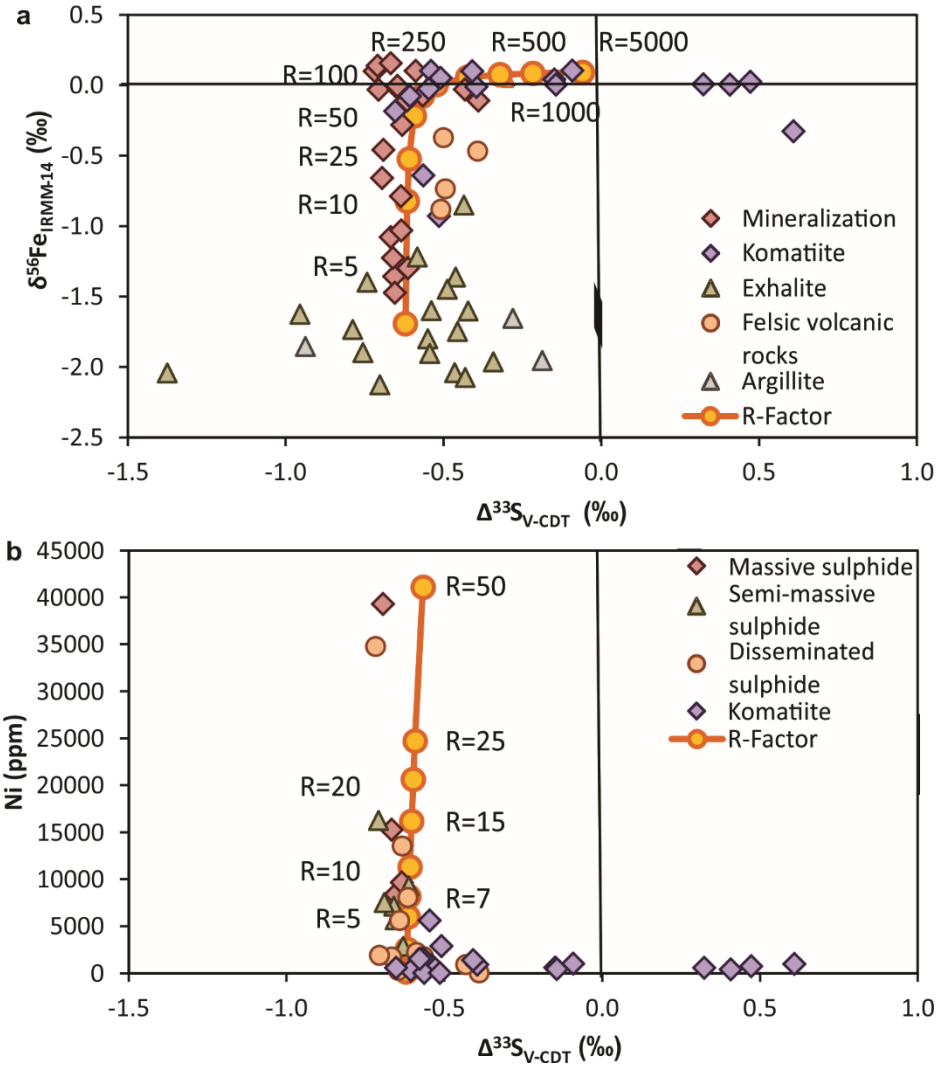

Figure 23: R factor modelling showing range of R factor between 5 and 100 for massive sulfides, semi-massive sulfides, disseminated sulfides, and barren komatiites based on $\delta^{56}Fe$ and $\Delta^{33}S$ values (a), and between 5 and 50 based on Ni concentrations and $\Delta^{33}S$ values (b).

are more sensitive to larger R factor values than those observed in mineralization at the Hart deposit. This resulted in a very limited range of $\Delta^{33}S$ values observed in the mineralized samples, making R factor estimates based on S isotopes alone very difficult in this case. As an independent estimate, average Pt concentration was used to calculate an R factor based on data from Barnes and Naldrett (1987). This calculation yielded an estimate of 27 for the R factor (Table 6), which is within the range of values generated in this study (5 to 50).

These R factor values are somewhat lower than those for most comparable komatiite-associated Ni-sulfide deposits, although still within the known range for these deposits (10 – 1100; Arndt et al., 2008). Magmatic systems with low R factors could still produce significant mineralization in an environment with localized contamination and S saturation, and little to no transport of sulfide xenomelt. Additionally, such low R factor values would require rapid segregation of the sulfide liquid from the komatiite magma, suggesting that flow of the komatiite melt was not vigorous and at most only weakly turbulent (Lesher and Campbell, 1993). These processes could have contributed to a relatively low Ni-tenor in the Hart deposit with only an average of 3.77% Ni in 100% sulfide (Barnes and Naldrett, 1987).

3.8 CONCLUSIONS

Through the use of sulfur and iron isotopes, we can distinguish between the two potential crustal sources of contamination for the komatiitic flow, which could have provided sulfur required for the genesis of the mineralization at the Hart deposit. Both the exhalite and graphitic argillite lithologies in the footwall to the deposit are characterized by negative $\Delta^{33}S$ and $\delta^{56}Fe$ values, suggesting low-temperature, potentially biological processing of both the S and Fe forming the sulfides in these rocks.

The $\Delta^{33}S$ and $\delta^{34}S$ data suggests different sulfur sources for the main and eastern extension mineralized zones of the Hart deposit. The main zone has sulfur likely derived from the exhalite unit, whereas the eastern extension derived its sulfur from the graphitic argillite unit. A minor local crustal sulfur source

with positive $\Delta^{33}S$ and $\delta^{34}S$ values, possibly a disseminated sulfide in shale, also contributed sulfur to the komatiite, but not in large enough amounts to produce economic sulfide mineralization. Samples from the footwall of the deposit analyzed in this study do not match this local source.

$\Delta^{33}S$, $\delta^{34}S$, and $\delta^{56}Fe$ values trend within the flow from the signature of crustal contamination towards mantle values away from the deposits, both laterally and vertically. This trend allows for vectoring towards mineralization within mineralized flows, even from a distance of a few hundred metres from the main mass of mineralization.

R factor calculations, involving $\Delta^{33}S$ and $\delta^{56}Fe$ values, and Pt and Ni concentrations, suggest a low R factor for the Hart deposit, between 5 and 50. This is lower than the estimates of R factor for several other komatiite-associated deposits and suggests that formation of the deposit resulted from a local contamination and rapid segregation of sulfide xenomelt from the komatiite magma.

3.9 Comparative Analysis of the Voisey's Bay and Hart Deposits

The Voisey's Bay and Hart magmas are mantle-derived, and would require the addition of sulfur to produce the massive sulfide deposits associated with them. The deposits were formed by a sulfide xenomelt, derived from the country rocks, interacting with the magma to become enriched in Ni, Cu, and PGE. This resulted in similar sulfide mineralogy in both deposits dominated by pyrrhotite, pentlandite, and chalcopyrite. The country rocks to both deposits became sulfur-bearing by precipitation of sulfides in sediments as a result of the metabolic processes of sulfate-reducing bacteria. Despite the differences in mode of emplacement, intrusive for Voisey's Bay, and extrusive for Hart, both magmas were flowing in the area of the deposits, with flow concentrated in a conduit or channel, providing continuous contact between the sulfur-bearing country rocks and very high temperature magma, promoting the formation of the sulfide xenomelt.

Despite the similarities, several fundamental differences exist between the two deposits including: the original magma composition, the nature of emplacement, the number of potential sulfur sources to the deposits, the age of the deposits, and the isotopic compositions of these sulfur sources. The original composition for the Voisey's Bay magma was high-Al basalt that resulted in a dominantly troctolitic intrusion, whereas the original composition for the Hart magma was komatiitic that resulted in Dunite as the dominant lithology in the flows. The mass of magma interacting with the sulfide xenomelt was also much higher in the Voisey's Bay deposit than the Hart deposit, resulting in $\delta^{56}Fe<0$ in some samples from the Hart deposit reflecting the preservation of a contaminant signature that would be unresolvable at higher mass ratios.

The sulfur source rocks also exhibit considerable differences between the deposits. The Tasiuyak gneiss has a well preserved signal of bacterial sulfate reduction, but had been metamorphosed to granulite facies conditions prior to the emplacement of the Voisey's Bay magma. The exhalite and graphitic argillite in the Hart area show evidence of bacterial sulfate reduction, but this signal is somewhat obscured by mass-independent fractionation by photochemical processes in the Archean anoxic atmosphere. Additionally, the sediments at the Hart deposit were likely unmetamorphosed at the time of emplacement of the Hart komatiite, and were significantly thermomechanically eroded by the komatiite flow. As such, examining the sedimentary sulfur sources in the Hart area, which are much better preserved than the sedimentary sulfur sources in the Voisey's Bay area, can also be useful in larger scale vectoring towards mineralization. Using the environments these rocks formed under narrow down potential areas on regional or camp-scale that are more likely to contain sulfur source rocks, leading to areas of high potential for magmatic sulfide deposits. Additionally, understanding the depositional environment of these rocks can provide useful insight into greenstone belt formation, and paleoenvironmental considerations during the Neoarchean.

3.10 REFERENCES

Archer, C., Vance, D. 2006. Coupled Fe and S isotope evidence for Archean microbial Fe(III) and sulfate reduction. Geology, 42; 153-156.

Arndt, N.T., Lesher, C.M., Barnes, S.J. 2008. Komatiite. Cambridge University Press, New York, 467 p.

Barnes, S.J., Hill, R.E.T., Perring, C.S., Dowling, S.E. 2004. Lithogeochemical exploration for komatiite-associated Ni-sulfide deposits: strategies and limitations. Mineralogy and Petrology, 82; 259-293.

Barnes, S.J., Lesher, C.M., Sproule, R.A. 2007. Geochemistry of komatiites in the Eastern Goldfields superterrane, Western Australia and the Abitibi greenstone belt, Canada, and the implications for the distribution of associated Ni-Cu-PGE deposits. Applied Earth Science, 116; 167-187.

Barnes, S.J., Fiorentini, M.L. 2012. Komatiite magmas and sulfide nickel deposits: a comparison of variably endowed Archean terranes. Economic Geology, 107; 755-780.

Barnes. S.J., Heggie, G.J., Fiorentini, M.L. 2013. Spatial variation in platinum group element concentrations in ore-bearing komatiite at the Long-Victor deposit, Kambalda Dome, Western Australia: enlarging the footprint of nickel sulfide orebodies. Economic Geology, 108; 913-933.

Beard, B.L., Johnson, C.M., Skulan, J.L., Nealson, K.H., Cox, L., Sun, H. 2003. Application of Fe isotopes to tracing the geochemical and biological cycling of Fe. Chemical Geology, 195; 87-117.

Bekker, A., Barley, M.E., Fiorentini, M.L., Rouxel, O.J., Rumble, D., Beresford, S.W. 2009. Atmospheric sulfur in Archean komatiite-hosted nickel deposits; Science, 326; 1086-1089.

Bekker, A., Grokhovskaya, T.L., Hiebert, R., Sharkov, E.V., Bui, T.H., Stadnek, K.R., Chashchin, V.V., Wing, B.A. 2016. Multiple sulfur isotope and mineralogical constraints on the genesis of Ni-Cu-PGE

magmatic sulfide mineralization of the Monchegorsk Igneous Complex, Kola Peninsula, Russia, Mineralium Deposita, 51; 1035-1053.

Bennett, S.A., Rouxel, O., Schmidt, K., Garbe-Schonberg, D., Statham, P.J., German, C.R. 2009. Iron isotope fractionation in a buoyant hydrothermal plume, 5 degrees S Mid-Atlantic Ridge. Geochimica et Cosmochimica Acta, 73; 5619-5634.

Butler, I.B., Archer, C., Vance, D., Oldroyd, A., Rickard, D. 2005. Fe isotope fractionation on FeS formation in ambient aqueous solution. Earth and Planetary Science Letters, 236; 430-442.

Campbell, I.H., Naldrett, A.J. 1979. The influence of silicate:sulfide ratios on the geochemistry of magmatic sulfides. Economic Geology, 75; 1503-1506.

Canfield, D.E., Raiswell, R., Westrich, J.T., Reaves, C.M., Berner, R.A. 1986. The use of chromium reduction in the analysis of reduced inorganic sulfur in sediments and shales. Chemical Geology, 54; 149-155.

Chaussidon, M., Albarede, F., Sheppard, S.M.F. 1989. Sulfur isotope heterogeneity in the mantle from ion microprobe measurements of sulfide inclusions in diamonds. Nature, 330; 242-244.

Dauphas, N., vanZuilen, M., Wadhwa, M., Davis, A.M., Marty, B., Janney, P.E. 2004. Clues from Fe isotope variations on the origin of early archean BIFs from Greenland. Science, 306; 2077-2080.

Dauphas, N. Rouxel, O. 2006. Mass spectrometry and natural variations of iron isotopes. Mass Spectrometry Reviews, 25; 515-550.

Dauphas, N., Teng, F.-Z., Arndt, N.T. 2010. Magnesium and iron isotopes in 2.7 Ga Alexo komatiites: Mantle signatures, no evidence for Soret diffusion, and identification of diffusive transport in zoned olivine. Geochimica et Cosmochimica Acta, 74; 3274-3291.

Farquhar, J., Bao, H., Thiemens, M. 2000. Atmospheric influence of Earth's earliest sulfur cycle. Science, 289; 756-758.

Farquhar, J., Savarino, J., Airieau, S., Thiemens, M.H. 2001. Observation of wavelength-sensitive mass-independent sulfur isotope effects during SO2 photolysis: Implications for the early atmosphere. Journal of Geophysical Research, 106; 32829-32839.

Farquhar, J., Wing, B.A. 2003. Multiple sulfur isotopes and the evolution of the atmosphere. Earth and Planetary Science Letters, 213; 1-13.

Farquhar, J., Wing, B.A., McKeegan, K.D., Harris, J.W., Cartigny, P., Thiemens, M.H. 2002. Mass-independent sulfur of inclusions in diamond and sulfur recycling on early earth. Science, 298; 2369-2372.

Fiorentini, M., Beresford, S., Barley, M., During, P., Bekker, A., Rosengren, N., Cas, R., Hronsky, J. 2012a. District to camp controls on the genesis of komatiite-hosted nickel sulfide deposits, Agnew-Wiluna greenstone belt, Western Australia: Insights from the multiple sulfur isotopes. Economic Geology, 107; 781-796.

Fiorentini, M.L., Bekker, A., Rouxel, O., Wing, B.A., Maier, W., Rumble, D. 2012b. Multiple Sulfur and Iron Isotope Composition of Magmatic Ni-Cu-(PGE) Sulfide Mineralization from Eastern Botswana. Economic Geology, 105; 107–116.

Guilbaud, R., Butler, I.B., Ellam, R.M. 2011. Abiotic Pyrite Formation Produces a Large Fe Isotope Fractionation. Science, 332; 1548-1551.

Habicht, K.S., Gade, M., Thamdrup, B., Berg, P., Canfield, D.E. 2002. Calibration of the sulfate levels in the Archean ocean. Science, 298; 2372-2374.

Hanski, E., Huhma, H., Rastas, P., Kamenetsky, V.S. 2001. The Palaeoproterozoic komatiite-picrite association of Finnish Lapland. Journal of Petrology, 42; 855-876.

Helt, K.M., Williams-Jones, A.E., Clark, J.R., Wing, B.A., Wares, R.P. 2014. Constraints on the genesis of the Archean oxidized, intrusion-related Canadian Malartic gold deposit, Quebec, Canada. Economic Geology, 109; 713–735.

Hiebert, R.S., Bekker, A., Wing, B.A., Rouxel, O.J. 2013. The role of paragneiss assimilation in the origin of the Voisey's Bay Ni-Cu sulfide deposit, Labrador: multiple S and Fe isotope evidence. Economic Geology, 108; 1459-1469.

Hofmann, A., Bekker, A., Dirks, P., Gueguen, B., Rumble, D., Rouxel, O.J. 2014. Comparing orthomagmatic and hydrothermal mineralization models for komatiite-hosted nickel deposits in Zimbabwe using multiple-sulfur, iron, and nickel isotope data. Mineralium Deposita, 49; 75-100.

Houlé, M.G., Lesher, C.M. 2011. Komatiite-associated Ni-Cu-(PGE) deposits, Abitibi greenstone belt, Superior Province, Canada; in Magmatic Ni-Cu and PGE deposits: geology, geochemistry, and genesis. Society of Economic Geologists, Reviews in Economic Geology, 17; 89-121.

Houlé, M.G., Gibson, H.L., Lesher, C.M., Davis, P.C., Cas, R.A.F., Beresford, S.W., Arndt, N.T. 2008. Komatiitic sills and multigenerational peperite at Dundonald Beach, Abitibi greenstone belt, Ontario: volcanic architecture and nickel sulfide distribution. Economic Geology, 103; 1269-1284.

Houlé, M.G., Préfontaine, S., Fowler, A.D., Gibson, H.L. 2009. Endogenous growth in channelized komatiite lava flows: evidence from spinifex-textured sills at Pyke Hill and Serpentine Mountain, western Abitibi greenstone belt, northeastern Ontario, Canada. Bulletin of Volcanology, 71; 881-901.

Houlé, M.G., Lesher, C.M., Gibson, H.L., Ayer, J.A., Hall, L.A.F. 2010a. Localization of komatiite-associated Ni-Cu-(PGE) deposits in the Shaw Dome, Abitibi greenstone belt, Superior Province. In: Abstracts, 11th International Platinum Symposium, 21–24 June 2010, Sudbury, Ontario, Canada, Ontario Geological Survey, Miscellaneous Release—Data 269.

Houlé, M.G., Lesher, C.M., Préfontaine, S., Ayer, J.A., Berger, B.R., Taranovic, V., Davis, P.C., Atkinson, B. 2010b. Stratigraphy and physical volcanology of komatiites and associated Ni-Cu-(PGE) mineralization in the western Abitibi greenstone belt, Timmins area, Ontario: a field trip for the 11th International Platinum Symposium; Ontario Geological Survey, Open File Report 6255, 99p.

Houlé, M.G., Lesher, C.M., Davis, P.C. 2012. Thermomechanical erosion at the Alexo Mine, Abitibi greenstone belt, Ontario: implications for the genesis of komatiite-associated Ni-Cu-(PGE) mineralization. Mineralium Deposita, 47; 105-128.

Jamieson, J.W., Wing, B.A., Farquhar, J., Hannington, M.D. 2013. Neoarchean seawater sulfate concentrations from sulfur isotopes in massive sulfide ore. Nature Geoscience, 6; 61-64.

Johnson, C.M., Beard, B.L., Beukes, N.J., Klein, C., O'Leary, J.M. 2003. Ancient geochemical cycling in the Earth as inferred from Fe isotope studies of banded iron formations from the Transvaal Craton. Contributions to Mineralogy and Petrology, 144; 523-547.

Kerr, A. 2003. The calculation and use of sulfide metal contents in the study of magmatic ore deposits: a methodological analysis. Exploration and Mining Geology, 10; 289-301.

Konnunaho, J.P., Hanski, E.J., Bekker, A., Halkoaho, T.A.A., Hiebert, R.S., Wing, B.A. 2013. The Archean komatiite-hosted, PGE-bearing Ni-Cu sulfide deposit at Vaara, eastern Finland: evidence for assimilation of external sulfur and post-depositional desulfurization. Mineralium Deposita, 48; 967-989.

Labidi, J., Cartigny, P., Birck, J.L., Assayag, N., Bourrand, J.J. 2012. Determination of multiple sulfur isotopes in glasses: A reappraisal of the MORB delta S-34. Chemical Geology, 334; 189-198.

Labidi, J., Cartigny, P., Moreira, M. 2013. Non-chondritic sulfur isotope composition of the terrestrial mantle. Nature, 501; 208-211.

Labidi, J., Cartigny, P., Jackson, M.G. 2015. Multiple sulfur isotope composition of oxidized Samoan melts and the implications of a sulfur isotope 'mantle array' in chemical geodynamics. Earth and Planetary Science Letters, 417; 28-39.

Lesher, C.M. 1989. Komatiite-associated nickel sulfide deposits. *In:* J.A. Whitney and A.J. Naldrett (eds.) Ore Deposition Associated with Magmas. Dordrecht: Society of Economic Geologists, pp. 45-102.

Lesher, C.M., Groves, D.I. 1986 Controls on the formation of komatiite-associated nickel-copper sulfide deposits: geology and metallogenesis of copper deposits; Proceedings of the Twenty-Seventh International Geological Congress, Berlin, Springer Verlag, pp. 43-62.

Lesher, C.M., Campbell, I.H. 1993. Geochemical and fluid dynamic modeling of compositional variations in Archean komatiite-hosted nickel sulfide ores in Western Australia. Economic Geology, 88; 804-816.

Lesher, C.M., Arndt, N.T. 1995. REE and Nd isotope geochemistry, petrogenesis and volcanic evolution of contaminated komatiites at Kambalda, Western Australia. Lithos, 34; 127-157.

Lesher, C.M., Burnham, O.M., Keays, R.R., Barnes, S.J., Hulbert, L. 1999. Geochemical discrimination of barren and mineralized komatiites in dynamic ore-forming magmatic systems. *In:* Keays, R.R., Lesher, C.M., Lightfoot, P.C., and Farrow, C.E.G. (eds.) Dynamic processes in magmatic ore

deposits and their application in mineral exploration, Geological Association of Canada, Short Course Volume 13, pp. 451-477.

Lesher, C.M., Burnham, O.M. 2001. Multicomponent elemental and isotopic mixing in Ni-Cu-(PGE) ores at Kambalda, Western Australia. The Canadian Mineralogist, 39; 421-446.

Lesher, C.M., Burnham, O.M., Keays, R.R. 2001. Trace-element geochemistry and petrogenesis of barren and ore-associated komatiites. The Canadian Mineralogist, 39; 673-696.

Marin-Carbonne, J., Rollion-Bard, C., Bekker, A., Rouxel, O., Agangi, A., Cavalazzi, B., Wohlgemuth-Ueberwasser, C.C. 2014. Coupled Fe and S isotope variations in pyrite nodules from Archean shale. Earth and Planetary Science Letters, 392; 67-79.

Mavrogenes, J.A., O'Neill, H.St.C. 1999. The relative effects of pressure, temperature and oxygen fugacity on the solubility of sulfide in mafic magmas. Geochimica et Cosmochimica Acta, 63; 1173-1180.

Maynard, J.B., Sutton, S.J., Rumble III, D., Bekker, A. 2013. Mass-independently fractionated sulfur in Archean paleosols: a large reservoir of negative $\Delta^{33}S$ anomaly on the early Earth. Chemical Geology, 362; 74-81.

McDonough, W.F., Sun, S.S. 1995. The composition of the Earth. Chemical Geology, 120; 223-253.

Moeller, K., Schoenberg, R., Grenne, T., Thorseth, I.H., Drost, K., Pedersen, R.B. 2014. Comparison of iron isotope variations in modern and Ordovician siliceous Fe oxyhydroxide deposits. Geochimica et Cosmochimica Acta, 126; 422-440.

Nebel, O., Campbell, I.H., Sossi, P.A., Van Kranendonk, M.J. 2014. Hafnium and iron isotopes in early Archean komatiites record a plume-driven convection cycle in the Hadean Earth. Earth and Planetary Science Letters, 397; 111-120.

Ono, S., Eigenbrode, J.L., Pavlov, A.A., Kharecha, P., Rumble III, D., Kasting, J.F., Freeman, K.H. 2003. New insights into Archean sulfur cycle from mass-independent sulfur isotope records from the Hamersley Basin, Australia. Earth and Planetary Science Letters, 213; 15-30.

Ono, S., Beukes, N.J., Rumble, D. 2009. Origin of two distinct multiple-sulfur isotope compositions of pyrite in the 2.5 Ga Klein Naute Formation, Griqualand West Basin, South Africa. Precambrian Research, 169; 48-57.

Penniston-Dorland, S.C., Mathez, E.A., Wing, B.A., Farquhar, J., Kinnaird, J.A. 2012. Multiple sulfur isotope evidence for surface-derived sulfur in the Bushveld Complex: Earth and Planetary Science Letters, 337-338; 236–242.

Planavsky, N., Rouxel, O.J., Bekker, A., Hofmann, A., Little, C.T.S., Lyons, T.W. 2012. Iron isotope composition of some Archean and Proterozoic iron formations. Geochimica et Cosmochimica Acta, 80; 158-169.

Pyke, D.R., Naldrett, A.J., Eckstrand, O.R. 1973. Archean ultramafic flows in Munro Township, Ontario. Geological Society of America Bulletin, 84; 955-978.

Ripley, E.M. 1999. Systematics of sulfur and oxygen isotopes in mafic igneous rocks and Cu-Ni-PGE mineralization; in Dynamic processes in magmatic ore deposits and their application in mineral exploration. Geological Association of Canada, Short Course Notes, v.13, pp. 111-158.

Ripley, E.M., Li, C. 2003. Sulfur isotope exchange and metal enrichment in the formation of magmatic Cu-Ni-(PGE) deposits. Economic Geology 98; 635-641.

Rouxel, O., Dobbek, N., Ludden, J., Fouquet, Y. 2003. Iron isotope fractionation during oceanic crust alteration. Chemical Geology, 202; 155-182.

Rouxel, O.J., Bekker, A., Edwards, K.J. 2005. Iron isotope constraints of the Archean and Paleoproterozoic ocean redox state. Science, 307; 1088-1091.

Rouxel, O.J., Bekker, A., Edwards, K.J. 2006. Response to Comments on "Iron isotope constraints of the Archean and Paleoproterozoic ocean redox state." Science, 311; 177b.

Rouxel, O., Shanks Iii, W.C., Bach, W., Edwards, K.J. 2008. Integrated Fe- and S-isotope study of seafloor hydrothermal vents at East Pacific Rise 9-10°N. Chemical Geology, 252; 214-227.

Sharman, E.R., Taylor, B.E., Minarik, W.G., Dubé, B., Wing, B.A. 2014. Sulfur isotope and trace element data from ore sulfides in the Noranda district (Abitibi, Canada): implications for volcanogenic massive sulfide deposit genesis, Mineralium Deposita, 50; 1-18.

Scheussler, J.A., Schoenberg, R., Behrens, H., von Blanckenburg, F. 2007. The experimental calibration of the iron isotope fractionation factor between pyrrhotite and peralkaline rhyolitic melt. Geochimica et Cosmochimica Acta, 71; 417-433.

Sproule, R.A., Lesher, C.M., Houlé, M.G., Keays, R.R., Ayer, J.A., Thurston, P.C. 2005. Chalcophile element geochemistry and metallogenesis of komatiitic rocks in the Abitibi greenstone belt, Canada. Economic Geology, 100; 1169-119.

Teng. F.-Z., Dauphas, N., Helz, R.T. 2008. Iron isotope fractionation during magmatic differentiation in Kilauea Iki lava lake. Science, 320; 1620-1623.

Teng, F.-Z., Dauphas, N., Huang, S., Marty, B. 2013. Iron isotope systematics of oceanic basalts. Geochimica et Cosmochimica Acta, 107; 12-26.

Thurston, P.C. 2008. Depositional gaps in Abitibi greenstone belt stratigraphy: a key to exploration for syngenetic mineralization. Economic Geology, 103; 1097-1134.

Thurston, P.C., Kamber, B.S., Whitehouse, M. 2012. Archean cherts in banded iron formation: insight into Neoarchean ocean chemistry and depositional processes. Precambrian Research, 214-215; 227-257.

Wendlandt, R.F. 1982. Sulfide saturation of basalt and andesite melts at high pressures and temperatures. American Mineralogist, 67; 877-885.

Weyer, S. 2008. What drives iron isotope fractionation in magma? Science, 320; 1600-1601.

Williams, H.M., Peslier, A.H., McCammon, C., Halliday, A.N., Levasseur, S., Teutsch, N., Burg, J.-P. 2005. Systematic iron isotope variations in mantle rocks and minerals: The effects of partial melting and oxygen fugacity. Earth and Planetary Science Letters, 235; 435-452.

Wing, B.A., Halevy, I. 2014. Intracellular metabolite levels shape sulfur isotope fractionation during microbial sulfate respiration. Proceedings of the National Academy of Sciences, 111; 18116-18125.

Yamaguchi, K.E., Johnson, C.M., Beard, B.L., Ohmoto, H. 2005. Biogeochemical cycling of iron in the Archean-Paleoproterozoic Earth: Constraints from iron isotope variations in sedimentary rocks from the Kaapvaal and Pilbara Cratons. Chemical Geology, 218; 135-169.

CHAPTER 4: DEPOSITIONAL SETTING OF THE LATE ARCHEAN FE OXIDE- AND SULFIDE-BEARING CHERT AND GRAPHITIC ARGILLITE IN THE SHAW DOME, ABITIBI GREENSTONE BELT, CANADA

R.S. Hiebert[1], A. Bekker[2,1], M.G. Houlé[3], B.A. Wing[4, 5], and O.J. Rouxel[6]

[1]University of Manitoba, Winnipeg, Canada

[2]Department of Earth Sciences, University of California, Riverside, CA, 92521, USA

[3]Geological Survey of Canada, Quebec, Canada

[4]McGill University, Montreal, Canada

[5]GEOTOP Research Center, Montreal, Quebec

[6]IFREMER, Centre de Brest, Unité Géosciences Marines, Plouzané, France

4.1 ABSTRACT

Interbedded chert-rich exhalite and graphitic argillite are the only sedimentary rocks deposited in deep-water settings during long-lived hiatuses in mafic to ultramafic volcanism within the Hart area of the Shaw Dome in the Late Archean Abitibi greenstone belt in Canada. The Fe oxide- and sulfide-bearing, but predominantly cherty, exhalite lithological unit in the Hart area can be traced laterally to iron formation elsewhere in the Shaw Dome. Whole-rock as well as Fe and S isotope geochemistry suggest that the exhalite unit was formed as a result of direct precipitation from seawater, distally from hydrothermal centres. Fractionation of Fe isotopes through the precipitation of iron oxyhydroxides in a neutrally buoyant hydrothermal plume removed the heavier isotopes of Fe, resulting in the negative δ^{56}Fe values observed in the exhalite in the Hart area. Archean seawater is generally considered to be anoxic, but moderate Mn enrichments (up to 1.87 weight % MnO) in exhalite along with negative Fe isotope values resulting from partial Fe(II) oxidation suggest the presence of oxygen in the upper part of the water column along the pathway of hydrothermal plumes from their source to the depositional site in the Abitibi greenstone belt. In contrast, the graphitic argillite contains abundant pyrite nodules and bands that exhibit systematic negative Fe isotope values, but does not show Mn enrichment. This unit likely formed in a zone of upwelling of nutrient-rich waters from deeper parts of the basin resulting in high organic productivity. Both exhalite and graphitic argillite have negative Δ^{33}S values, suggesting that sulfur was derived from seawater sulfate, which is consistent with an anoxic atmosphere with sulfate aerosols produced by photochemical reactions. Combined, our data indicates disequilibrium between anoxic atmosphere and partially oxygenated upper part of the water column during periods of volcanic quiescence in the ~2.7 Ga Abitibi greenstone belt supporting the existence of oxidized oases within the Archean ocean.

4.2 INTRODUCTION

It is widely accepted that the Archean atmosphere contained little or no oxygen (Farquhar et al., 2001), with multiple S isotope data constraining the level of oxygen in the Archean atmosphere to less than 10^{-5} PAL (e.g., Farquhar et al., 2000, 2001; Pavlov and Kasting, 2002). At the same time, multiple studies using trace element and stable isotope data indicate the presence of low oxygen levels, locally or episodically in the Archean ocean (e.g., Anbar et al., 2007; Kaufman et al., 2007; Reinhard et al., 2009; Riding et al., 2014; Fralick and Riding, 2015), in highly productive areas of continental margins (e.g., Olson et al., 2013; Planavsky et al., 2014), or in continental settings in association with microbial mats (e.g., Lalonde and Konhauser, 2014). The current view of Archean surface redox conditions is that the anoxic atmosphere was in disequilibrium with locally and/or episodically oxidized continental and nearshore oceanic settings (e.g., Lyons et al., 2014). The extent of these oxidized oases, however, remains uncertain and is still debated (e.g., Lalonde and Konhauser, 2014).

Evidence in support of locally developed oxidizing environments includes Mn enrichment in Archean sedimentary rocks (Maynard, 2014). Mn enrichment occurs under most modern and Phanerozoic marine redox conditions due to the precipitation of Mn-oxyhydroxides, and their formation, even though bacterially mediated, requires presence of at least low levels of oxygen. As such, sedimentary Mn deposits and Mn enrichments in sediments are rare in the Archean sedimentary record (Maynard, 2014).

As previously suggested (Rouxel et al., 2005; von Blanckenburg et al., 2008; Steinhoefel et al., 2009; Tsikos et al., 2010; Planavsky et al., 2012; Busigny et al., 2014; Kurzweil et al., 2016), anoxygenic phototrophic oxidation could have established significant water column Fe concentration gradients – and therefore Fe isotope trends – through ferric Fe removal during upwelling. However, several cases of Archean and early Paleoproterozoic Mn-rich iron formations with highly negative Fe isotope values have

been documented recently (e.g., Rouxel et al., 2005; Tsikos et al., 2010; Planavsky et al., 2012; Haugaard et al., 2017; Mendes et al., 2017; Lantink et al., 2018), potentially indicating an extreme degree of Fe depletion in an expanding hydrothermal plume in association with precipitation of iron oxyhydroxides and, ultimately, Mn oxidation. Recently, Ossa Ossa et al. (2016) found Mn to be present in carbonates, orthosilicates, oxides, phyllosilicates, and pyrite in Mn-rich shales and BIFs of the Mesoarchean Mozaan Group within the Pongola Supergroup in South Africa. However, it still remains unknown whether these rare occurrences of Mn-enrichment reflect short-lived periods of atmospheric oxygenation or localized marine oxygen oases.

The Hart deposit within the Abitibi greenstone belt is a komatiite-associated Ni-Cu-(PGE) magmatic sulfide deposit that has derived much of the sulfur from the underlying metasedimentary rocks (Hiebert et al., 2016). The predominant sulfur source rock has been considered to be sulfur-rich iron formation (Houlé et al., 2010b), but locally it is significantly more silica-rich, and iron oxide-poor, than the typical iron formation leading to it being referred to as a lean iron formation. This unit also contains zones of significant sulfide accumulation as pyrrhotite- and pyrite-rich bands and lenses. Although this unit is regionally interpreted as a true iron formation, the prevalence of silica-rich, and iron oxide-poor, assemblage, as well as the abundance of sulfides in the vicinity of the Hart deposit suggests that some environmental, depositional, or chemical conditions were different than elsewhere along strike. Additionally, Bekker et al. (2010) argued that true iron formation should not contain significant concentrations of sulfides, and that rocks previously classified as “sulfide-facies iron formations” may be actually sulfide-rich shales or barren sulfide (e.g., lacking base-metal mineralization) exhalative deposits formed from hydrothermal fluids either distally from the vent or under low-temperature conditions.

In the Abitibi greenstone belt, periods of widespread sedimentation have been shown to represent long-lived hiatuses in the rapid accumulation of volcanic rocks, during which siliciclastic and chemical

sedimentary rocks slowly accumulated (Thurston et al., 2008). These sedimentary rocks thus provide an insight into seawater composition and redox conditions as well as marine processes at the time of magmatic quiescence in the Archean ocean. In this study, we seek to constrain the depositional environment and diagenetic history of the exhalite and graphitic argillite lithologies within the Hart area of the Shaw Dome in the Abitibi greenstone belt through the comparison with two end-member processes. As iron formations are thought to be related to hydrothermal activity (Isley, 1995; Beukes and Gutzmer, 2008; Bekker et al., 2010), purely hydrothermal deposition of exhalative chert, iron oxides, and sulfides is considered as one end-member. The second end-member would be precipitation from ambient seawater directly unrelated to hydrothermal processes and may or may not be aided by biological activity (e.g., Li et al., 2015). We evaluate these two possible end-members using petrographic analysis of the sedimentary unit as well trace element and rare-earth element (REE) geochemistry to determine the chemical nature of the water column, along with multiple isotopes of sulfur and iron to determine the sources of these elements in the Fe-oxides and Fe-sulfides present in the sedimentary rocks. Additionally, we address the possibility that the chert exhalites and graphitic argillites were deposited during volcanic quiescence in the ca. 2.7 Ga Abitibi greenstone belt within a localized, marine oxidized oasis by studying geochemical proxies that constrain atmospheric and local marine redox conditions.

4.3 Geological Setting

The volcano-sedimentary succession of the Late Archean Abitibi greenstone belt has been previously subdivided into 9 volcanic and sedimentary episodes, in which long-lived hiatuses in the rapid emplacement of volcanic rocks are represented by slowly accumulated sedimentary deposits (Thurston et al., 2008; Houlé and Lesher, 2011; Thurston et al., 2012). Conventionally, the Abitibi greenstone belt has been interpreted to have been developed autochthonously, with the volcanic sequences tectonically stacked upon each other, with only the younger Temiskaming and Porcupine sequences deposited in

transtensional, pull-apart basins (e.g. Thurston and Chivers, 1990). Recently, however, it has been suggested that the volcanic rocks of the Abitibi greenstone belt were formed within a rift environment in which feeder dykes of the younger volcanic units crosscut older units, indicating autochtonous position (Ayer et al., 2002; Ayer et al., 2005; Ketchum et al., 2008; Thurston et al., 2008). Importantly, younger volcanic rocks contain zircon xenocrysts derived from older volcanic rocks suggesting that the volcanic sequences developed on top of each other (Ayer et al., 2002; Ayer et al., 2005; Thurston et al., 2008). In the Shaw Dome, the volcano-sedimentary succession is composed of the following units (Figure 3; Thurston et al., 2008; Houlé and Lesher, 2011; Thurston et al., 2012):

1) massive and pillowed, intermediate volcanic rocks and thin, but laterally extensive, iron formations of the 2734–2724 Ma volcanic sequence (Deloro);
2) felsic to intermediate, volcaniclastic rocks intercalated with komatiitic dikes, sills, lavas, and less extensive iron formations in the lower part of the 2710 – 2704 Ma volcanic sequence (lower Tisdale);
3) intercalated, tholeiitic, mafic, and komatiitic volcanic rocks of the middle part of the 2710 – 2704 Ma volcanic sequence (middle Tisdale); and
4) calc-alkaline, felsic to intermediate volcanic rocks in the upper part of the 2710–2704 Ma volcanic sequence (upper Tisdale; Houlé et al., 2010a, b; Houlé and Lesher, 2011).

Felsic to intermediate, volcanic and sedimentary rocks of the lower Tisdale sequence, overlain by komatiitic and basaltic lava flows of the middle Tisdale sequence outcrop in the Hart area. At the base of the middle Tisdale volcanic package, komatiitic lava flows have thermomechanically eroded a wide (>200 m) channel into its footwall rocks, which are dominantly composed of felsic to intermediate, volcanic and volcaniclastic rocks with lesser amounts of chert, graphitic argillite, and minor iron formation of the regional lower Tisdale volcanic package (Figure 10; Houlé et al., 2010b). The chert and

graphitic argillite appear to be interbedded on a meter-scale at and stratigraphically below the channel in drill cores. For simplicity, the prefix meta- will be omitted in the following description, but all rocks in the study area have been metamorphosed under lower to upper greenschist facies conditions (Thompson, 2005).

4.3.1 Description of Sedimentary Lithologies in the Hart Area

Regionally, the exhalite unit is generally continuous on the scale of several kilometers, and has been mapped and classified as iron formation, although in many locations it is described as a lean or chert-rich iron formation (Houlé et al., 2010b). However, based on the predominance of chert and silica-rich lithologies in the vicinity of the Hart deposit, it has been reclassified as a distal exhalite by Hiebert et al. (2016; Figure 12a), since it is interpreted to have largely been formed through an exhalative process (cf. Ridler, 1971). The exhalite unit typically contains thin laminae of Fe-oxides or sulfides (Figures 12b, c; e.g., sample H11-16-411.4; 86.2% SiO_2, 10.9% Fe_2O_3), but lacks any other sedimentary structures. Locally, the chert or silica-rich lithologies grade into typical banded iron formation (e.g., sample H11-13C-387.2; 41.73% SiO_2, 37.44% Fe_2O_3) or massive sulfide composed of pyrrhotite and pyrite, but these sulfidic lithologies are thought to extend for only a few tens of meters, and cannot be traced between drill holes and outcrops. The sulfides within the exhalite typically contain fine-grained pyrrhotite (0.1 – 0.2 mm in size) that appears to have been locally replaced by pyrite (0.25 – 0.6 mm in size), which still contains inclusions of pyrrhotite (Figure 12d). The sulfides form lenses or are found to be replacing Fe-oxide laminae. The unit also contains minor silicates, such as actinolite and chlorite as replacement minerals, and calcite as a replacement mineral and, possibly, as cement.

The graphitic argillite is only observed in the drill core in the eastern part of the Hart property. Based on visual estimates with optical microscope and geochemical data, it is composed of 35 – 50% graphite by volume (TOC content is up to 17.6 wt.% with the average of 8.5 wt.%) and 10 – 40% sulfide by volume

(TS content is up to 47.4 wt.% with the average of 28.0 wt.%), with variable amounts of metamorphic chlorite, epidote, actinolite, and quartz (10 – 60 wt.% SiO_2; Figures 24a, b). Sulfide in the graphitic argillite takes two forms, large (1 – 1.5 cm in diameter) pyrite nodules and bands (Figure 24c), or finely disseminated pyrite (<0.1 mm in diameter; Figure 24d).

4.4 S AND FE ISOTOPE BACKGROUND

The majority of earlier research attempted to characterize the processes producing the sulfides in sedimentary rocks using $\delta^{34}S$ values, but the range of sulfur isotope values recorded in Archean supracrustal rocks is much smaller than that in Phanerozoic examples, commonly resulting in near-to-mantle $\delta^{34}S$ values (Ripley, 1999). This can lead to a difficulty in identifying the processes responsible for the origin of these sedimentary sulfides. The values of $\delta^{34}S$ are expressed in parts per thousand (‰ or per mil), and are defined as:

$$\delta^{34}S = 1000 * \left(\frac{\frac{^{34}S}{^{32}S}sample}{\frac{^{34}S}{^{32}S}V-CDT} - 1\right) \quad (9)$$

where V-CDT is a reference scale defined by the isotopic composition of IAEA-S-1, a sulfur reference material distributed by the International Atomic Energy Agency (IAEA, Vienna), and calibrated to have $\delta^{34}S_{IAEA\text{-}S\text{-}1} \equiv -0.3‰$ based on the historical Canõn Diablo Troilite reference material (Coplen and Krouse, 1998). A similar formula is used to calculate $\delta^{56}Fe$, with masses 56 and 54 forming the ratio and IRMM-14 used as the reference standard (see recent review by Dauphas et al., 2017).

Under oxygenated Earth's surface conditions, sulfur isotope fractionation is controlled strictly by relative isotope mass differences and, therefore, is a completely mass-dependent process. However, as a result of photochemical reactions in the Archean anoxic atmosphere, atmospherically processed Archean sulfur exhibits widespread mass-independent fractionation that can be characterized by the difference

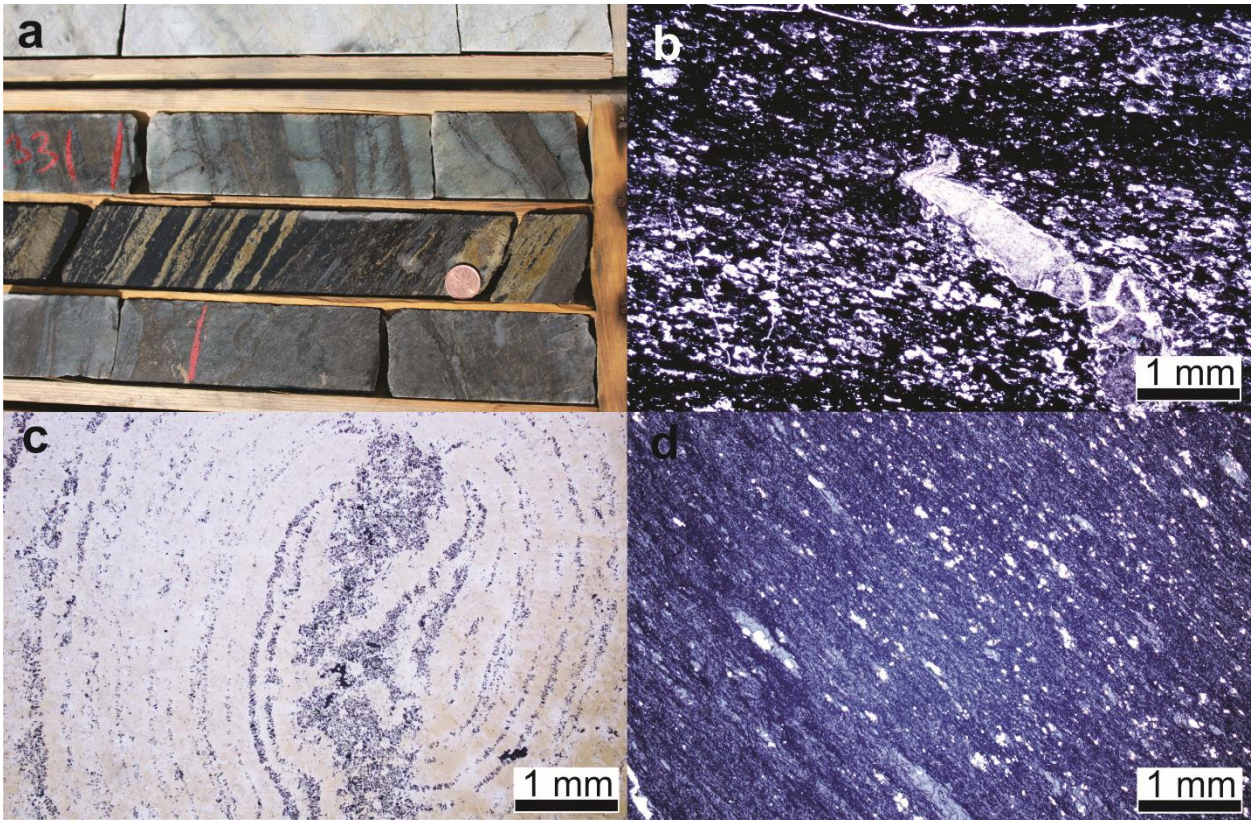

Figure 24: a Core photo of graphitic argillite showing nodules and bands of pyrite intercalated with chert-rich exhalite unit above and below. The coin is 18 mm in diameter. b Photomicrographs of graphitic argillite unit in plane-polarized light showing quartz (white) and chlorite (grey), and opaque graphite and pyrite (sample H11-13C-357.1). c Photomicrograph in reflected-light of pyrite nodule in graphitic argillite showing growth in concentric bands (sample H11-13C-357.1). d Photomicrograph of graphitic argillite unit in reflected-light (sample H11-13C-366.1) showing minor disseminated pyrite (bright grains), opaque mineral (graphite), and silicates (light grey).

between the $\delta^{33}S$ value expected from normal mass-dependent fractionation and the measured $\delta^{33}S$ value (Farquhar and Wing, 2003). It can be calculated using measured $\delta^{33}S$ and $\delta^{34}S$ values (in per mil) as:

$$\Delta^{33}S = \delta^{33}S - \left[\left(\frac{\delta^{34}S}{1000} + 1\right)^{\lambda_{RFL}} - 1\right] \times 1000 \quad (10)$$

where the λ_{RFL} has been defined as the slope of the reference fractionation line for ^{33}S and ^{34}S isotopes equal to 0.515.

Photochemically fractionated sulfur can then be delivered to seawater and ultimately sediments. Two isotopically distinct sulfur pools were formed by the photochemical reactions in the Archean atmosphere: 1) a reduced pool with positive $\Delta^{33}S$ and $\delta^{34}S$ values, and 2) an oxidized pool with negative $\Delta^{33}S$ and $\delta^{34}S$ values (e.g., Farquhar et al., 2002; Ono et al., 2003; Figure 21). The reduced pool is inferred to have been delivered to the Archean ocean as either elemental sulfur (S^0) aerosols or sulfide (S^{2-}), which then reacted with Fe^{2+} dissolved in the anoxic seawater and precipitated as disseminated Fe-sulfide in sediments (Ono et al., 2009; Maynard et al., 2013; Marin-Carbonne et al., 2014). The oxidized sulfur pool, delivered from the atmosphere as sulfate aerosols, is thought to have been either reduced by bacterial metabolism and incorporated into paleosols on the continents (Maynard et al., 2013), or added to seawater as dissolved sulfate (Farquhar et al., 2002). Once delivered to seawater, sulfate was either reduced via bacterial sulfate-reducing metabolism to form eventually pyrite nodules in organic matter-rich sediments during diagenesis, or cycled through submarine hydrothermal systems. Under hydrothermal conditions, seawater sulfate is first precipitated as Ca-sulfate (anhydrite), with a remaining fraction becoming eventually reduced at high temperature and vented at the seafloor as H_2S-rich hydrothermal fluids forming barren massive sulfide lenses distally and base-metal volcanogenic massive sulfide deposits proximally to hydrothermal centers (e.g., Bekker et al. 2009; Jamieson et al.,

2013). A significant fraction of anhydrite is redissolved as aging and cooling oceanic crust is transported away from spreading mid-ocean ridges (Alt, 1995).

Once in aqueous phase either on the land or in the ocean, the near-to-zero to negative $\delta^{34}S$ values of SO_2-derived sulfate could have been further modified by mass-dependent processes; for example, by bacterial or thermochemical seawater sulfate reduction, resulting in nodules or layers of sulfides in sediments with variable $\delta^{34}S$ values, but with consistently negative $\Delta^{33}S$ values (Ono et al., 2003, 2009; Bekker et al., 2009; Marin-Carbonne et al., 2014). Unlike in modern oceans, however, Archean seawater had relatively high iron content, but low sulfate concentrations, less than 80-200 µmol L^{-1} (Habicht et al., 2002; Jamieson et al., 2013), which resulted in small sulfur isotopic fractionations during bacterial sulfate reduction in a closed to semi-closed pore-water system due to much faster sulfate reduction with respect to sulfur transport rates (Brunner and Bernasconi, 2005; Detmers et al., 2001). As a result of nearly complete reduction of seawater sulfate in anoxic, organic matter-rich sediments, Archean pyrite does not exhibit the large variations in $\delta^{34}S$ values seen in modern marine sediments.

Iron isotope fractionation is thought to be dominantly controlled by redox reactions. Igneous rocks typically have $\delta^{56}Fe$ values of ~0.1‰ (e.g., Beard et al., 2003; see also recent review by Dauphas et al., 2017), but redox reactions under surface conditions, as recorded by sedimentary rocks with significant authigenic Fe enrichment (e.g., iron formations and black shales), tend to fractionate Fe in oxidized Fe-mineral species towards positive $\delta^{56}Fe$ values (e.g., Planavsky et al., 2012), and in reduced Fe-mineral species towards negative $\delta^{56}Fe$ values (e.g., Rouxel et al., 2005). During oxidative precipitation from fluids containing dissolved Fe^{2+}, redox reactions will preferentially remove the heavier isotopes of Fe with oxidized phases resulting in residual iron in the fluid having a lower $\delta^{56}Fe$ value. For example, precipitation of magnetite corresponds to a fractionation factor $\Delta^{56}Fe_{Fe(II)aq\text{-}magnetite}$ ~-1.3‰ (Johnson et al., 2005), while precipitation of goethite and ferrihydrite (HFO) results in $\Delta^{56}Fe_{Fe(II)aq\text{-}goethite}$ ~-1‰ (Beard

et al., 2010) and $\Delta^{56}Fe_{Fe(II)aq\text{-}HFO}$ ~-3.2‰, respectively (Wu et al., 2011). The "reservoir" effects during partial Fe^{2+} oxidation have been well demonstrated in biotic and abiotic experimental studies (e.g., Balci et al., 2006; Croal et al., 2004) and in modern redox-stratified aqueous environments (Busigny et al., 2014; Rouxel et al., 2008, 2018). Dissimilatory Fe^{3+} reduction (DIR), which is known to produce isotopically light Fe in diagenetic environments (Crosby et al., 2007; Tangalos et al., 2010; Percak-Dennett et al., 2011), may also produce a Fe^{2+}pool with negative $\delta^{56}Fe$ values. A clear distinction between these two mechanisms (i.e., partial Fe^{2+} oxidation versus partial Fe^{2+} reduction) as the source of isotopically light Fe^{2+} has been generally difficult to draw, even in modern marine or diagenetic environments (Severmann et al., 2008; Chever et al., 2015). Both low and high-temperature alteration of oceanic crust by seawater leads to the preferential release of more soluble Fe^{2+}, resulting in seafloor hydrothermal fluids having $\delta^{56}Fe \leq 0$‰ (Rouxel et al., 2003; Rouxel et al., 2008). As pyrite is often precipitated through a mackinawite ($FeS_{0.9}$) precursor, it preferentially incorporates the lighter isotopes of Fe, resulting in $\delta^{56}Fe$ values of the sulfide to be 0.3 to 0.9‰ lower than residual dissolved Fe^{2+} (Butler et al., 2005; Guilbaud et al., 2011). Further (i.e., partial) conversion to pyrite might also result in additional fractionation, resulting in final values of $\delta^{56}Fe$ that are 1.7 to 3.0‰ lower than the initial dissolved Fe^{2+}. Therefore, Fe delivered to the oceans by hydrothermal fluids, and any Fe-sulfides precipitated from these fluids, typically have slightly negative $\delta^{56}Fe$ values, although heavier values of the hydrothermal Fe flux are expected in the case of extensive Fe-sulfide precipitation in hydrothermal plume environments (Bennett et al., 2009; Rouxel et al., 2016; Lough et al., 2017). There are several notable exceptions of Fe-oxide iron formations of Archean and Paleoproterozoic age with negative Fe isotope values that are typically Mn-enriched and largely deposited in shallow-water settings (e.g., Rouxel et al., 2005; Tsikos et al., 2010; Planavsky et al., 2012; Haugaard et al., 2017; Mendes et al., 2017; Lantink et al., 2018). Their iron isotope values are considered to be the result of reservoir effects (e.g. Rayleigh distillation) associated with the earlier removal of Fe-oxides and oxyhydroxides resulting in

negative $\delta^{56}Fe$ values of the residual Fe in the spreading hydrothermal plume distally from the hydrothermal vents (Planavsky et al., 2012).

4.5 Material Analyzed and Analytical Methods

4.5.1 Sampling Methodology

All samples (n=27) for this project were selected from drill cores and surface trenches produced by Northern Sun Mining Corp. (Table 7). Sampling of drill core and surface trenches was conducted to obtain a wide range of lithologies from the exhalite and graphitic argillite units. Bulk rock samples were used for analysis to limit the impact of metamorphism on the results, and no samples were taken near known faults or shear zones to avoid potential large scale element mobility. Samples were analyzed by the same methods for whole rock lithogeochemistry, S and Fe isotopes as in the previous chapter.

4.5.2 Major and Trace Element Geochemistry

Samples were analyzed for major, trace, and rare-earth elements in two laboratories: The Ontario Geological Survey Geoscience Laboratories (Geo Labs; Sudbury, Ontario) and the Acme Laboratories (Acme Labs; Vancouver, British Columbia). All the materials were crushed at the Stable Isotopes for Innovative Research (SIFIR) laboratory at the University of Manitoba to a fine powder (200 mesh) using an agate puck mill before the pulps were sent to these laboratories for geochemical analysis. At Geo Labs, major elements were determined by mixing sample powder with a borate flux and heating to create a glass bead, which was analyzed by X-ray fluorescence (XRF), and trace, including rare-earth, elements were measured on an inductively coupled plasma-mass spectrometer (ICP-MS) after digestion in a closed vessel using multi-acid technique. At Acme Labs, samples were prepared via a lithium borate fusion and were analyzed for major elements by ICP-ES, and for trace elements by ICP-MS. In both labs, total C and S were determined by oxidation through combustion of the sample in an oxygen-rich environment and detection of CO_2 and SO_2 by infrared absorption (LECO elemental analyzer). Both labs

use duplicate analyses of samples and certified reference materials to confirm the precision and accuracy of data.

4.5.3 Bulk Rock S Isotope Analysis

Sulfur was extracted from rock powders and converted to Ag_2S in both the SIFIR lab (University of Manitoba) and the Stable Isotope Laboratory of the Department of Earth and Planetary Sciences (McGill University) with a Cr(II) reduction procedure that has been already applied to a range of different types of ore metal sulfides from mafic to ultramafic intrusive systems (Fiorentini et al., 2012b; Hiebert et al., 2013), komatiite-associated Fe-Ni-Cu sulfide mineralization (Konnunaho et al., 2013), volcanic massive sulfide deposits (Sharman et al., 2014), and oxidized intrusion-related gold deposits (Helt et al., 2014). All samples were analyzed at McGill University by first fluorinating the Ag_2S at 225°C in a Ni autoclave under ≈20X stoichiometric excess of F_2 for >9 hours to produce SF_6, which was then purified cryogenically and chromatographically and analyzed on a Thermo Electron MAT 253 mass-spectrometer for multiple sulfur isotope ratios in a dual-inlet mode. The sulfur isotope compositions are reported with respect to the V-CDT scale, on which the $\delta^{34}S$ value of IAEA-S-1 is defined as -0.3‰, and the $\Delta^{33}S$ value is taken to be 0.094‰ (Table 8). Repeat analyses throughout the entire analytical procedure return 2σ uncertainties on $\delta^{34}S$ and $\Delta^{33}S$ values that are <0.3 and <0.02‰, respectively.

4.5.4 Bulk Rock Fe Isotope Analysis

Aliquots for Fe isotope analysis and major and trace element analysis were prepared from the remaining material following S isotope analysis by crushing the sample in an agate mortar. The crushed sample was then dissolved in a trace-metal grade HNO_3-HCl acid mixture and evaporated to dryness on a hot plate at 60°C. Complete dissociation and oxidation of Fe was achieved by dissolving this residue in aqua regia and evaporating to dryness on a hot plate again. The dry residue was dissolved in 6N HCl in a heated vessel (40°C), which was agitated by ultrasonication. The solution was then centrifuged to separate, and

remove, any C-rich material. Fe was extracted from a volume of solution corresponding to 2500 µg of Fe by Bio-Rad AG-1X8 anion resin, which adsorbs ferric iron to the surface of the resin, in a column. The matrix was then dissolved, and other ions striped from the resin, by passing 20 mL of 6N HCl through the column. Iron was then eluted in a 20 mL bath of 0.12N HCl. This solution was evaporated to dryness and the residue was dissolved with 1% HNO_3 to obtain 5 mL of 500 ppm Fe in solution. Isotopic ratios ($\delta^{56}Fe$ and $\delta^{57}Fe$) were determined with a Thermo Electron Neptune multi-collector inductively-coupled mass-spectrometer (MC-ICP-MS) at PSO in medium-resolution mode, which allows distinction between possible interferences of ArO on ^{56}Fe, ArOH or ^{57}Fe, and ArN on ^{54}Fe (Rouxel et al., 2005). Instrumental bias was corrected using simultaneous measurement of Ni isotopes (^{60}Ni and ^{62}Ni) from an internal standard solution that was introduced into the plasma with the sample. "Sample-standard" bracketing was also used to correct for instrumental mass discrimination and instrumental drift by normalizing the sample to the average value for the standard measured before and after the sample. As the "sample-standard" correction method is prone to matrix effects, the combination of both measurement of Ni isotopes and the "sample-standard" bracketing corrects for this and provides accurate and precise results. Based on duplicated chemical purification and analysis of a reference standard periodically over the life of the lab, the external reproducibility is 0.08‰ for $\delta^{56}Fe$ and 0.11‰ for $\delta^{57}Fe$ values (2σ). Iron isotope values are reported relative to the standard IRMM-14, using the conventional delta notation (Table 8).

4.5.5 Microbeam Analysis

Two samples were selected for analysis on a Cameca SX100 electron microprobe at the University of Manitoba. These samples (H11-13C-387.2 and H11-08-63.9) were analyzed using energy dispersive x-ray spectroscopy (EDS) to identify the host of Mn in exhalite.

Table 7: Whole rock geochemistry data for sedimentary rocks in the Hart area.

Sample ID			H07-10-66.35	H07-10-73.6	H07-10-86.85	H07-56-188.9	H07-56-210.6	H08-106-98.6	H08-80-103.2
DDH			H07-10	H07-10	H07-10	H07-56	H07-56	H08-106	H08-80
Lithology	MDL (GeoLabs)	MDL (Acme)	Exhalite	Exhalite	Exhalite	Exhalite	Exhalite	Exhalite	Exhalite
SiO2	0.04	0.01	11.02	4.14	27.19	5.25	1.66	11.83	25.43
TiO2	0.01	0.01	0.02					0.01	0.01
Al2O3	0.02	0.01	0.6	0.25	0.11	0.40	0.12	0.22	0.33
Fe2O3T	0.01	0.04	53.3	64.08	53.50	55.37	67.03	65.42	48.62
MgO	0.01	0.01	0.07	0.8	2.13	1.02	0.77	3.40	1.57
MnO	0.002	0.01	0.02	0.83	1.37	0.22	0.75	0.45	0.24
CaO	0.006	0.01	0.08	5.46	5.14	7.09	3.48	2.58	1.76
Na2O	0.02	0.01	0.01	<0.01	<0.01	0.03	<0.01	0.03	0.03
K2O	0.01	0.01	0.17	0.06	<0.01	0.16	0.03	<0.01	0.03
P2O5	0.002	0.01	<0.01	0.03	<0.01	<0.01	0.04	<0.01	<0.01
LOI	0.05	0.01	34.6	24.3	10.50	24.90	26.00	16.00	21.50
CO2	0.03	0.02	0.15	1.11	1.23	1.68	0.89	0.03	0.32
S	0.01	0.02	38.48	36.99	18.58	36.03	37.66	26.34	27.90
Li	0.4								
Be	0.04	1	<1	<1	<1	<1	<1	1	3
Sc	1.1	1	1	12	1	<1	12	3	<1
Ti	7								
V	0.8	8	<8	<8	<8	<8	10	<8	<8
Cr	3								
Co	0.13	0.2	51.7	41.3	16.0	93.0	71.7	93.5	73.6
Ni	1.6	0.1	119.1	40.7	42.6	109.6	140.4	149.6	3172.6
Cu	1.4	0.1	33.2	18.2	13.5	47.9	25.4	209.3	428.6
Zn	7	1	386	43	14	14	8	5	9
Ga	0.04	0.5	<0.5	<0.5	<0.5	<0.5	<0.5	<0.5	<0.5
Rb	0.23	0.1	3.5	3.3	0.3	8.2	1.7	0.5	1.5
Sr	0.6	0.5	1.5	25.8	14.4	75.8	17.1	2.4	3.0
Y	0.05	0.1	0.2	4.9	4.0	2.5	2.3	7.3	5.2
Zr	6	0.1	106.1	33.1	44.7	63.1	44.5	32.4	66.4
Nb	0.028	0.1	0.1	<0.1	<0.1	<0.1	<0.1	<0.1	<0.1
Mo	0.08	0.1	1.5	2.2	0.5	2.1	0.6	6.3	0.6
Cd	0.013	0.1	0.2	<0.1	<0.1	<0.1	<0.1	<0.1	<0.1
In	0.0018								
Sn	0.16	1	<1	<1	<1	<1	<1	<1	<1
Sb	0.04	0.1	1.4	0.8	0.3	0.4	2.2	<0.1	0.1
Cs	0.013	0.1	0.2	1.5	<0.1	2.2	0.9	0.3	0.5
Ba	0.8	1	32	6	5	20	6	3	5
La	0.04	0.1	0.4	2.1	0.9	2.0	0.8	2.8	3.1
Ce	0.12	0.1	0.5	3.4	1.4	3.3	1.1	4.3	4.8
Pr	0.014	0.02	0.12	0.47	0.20	0.37	0.16	0.52	0.59
Nd	0.06	0.3	0.4	1.8	0.7	1.6	0.6	2.3	2
Sm	0.012	0.05	<0.05	0.33	0.17	0.21	0.06	0.44	0.41
Eu	0.0031	0.02	0.02	0.24	0.14	0.09	0.10	0.35	0.33
Gd	0.009	0.05	0.08	0.45	0.30	0.35	0.20	0.55	0.52
Tb	0.0023	0.01	<0.01	0.05	0.03	0.06	0.01	0.08	0.07
Dy	0.009	0.05	0.07	0.42	0.29	0.33	0.22	0.68	0.42
Ho	0.0025	0.02	<0.02	0.09	0.08	0.07	0.04	0.15	0.1
Er	0.007	0.03	0.04	0.39	0.26	0.21	0.14	0.47	0.37
Tm	0.0019	0.01	<0.01	0.03	0.04	0.02	<0.01	0.06	0.04
Yb	0.009	0.05	0.05	0.3	0.24	0.12	0.11	0.46	0.34
Lu	0.002	0.01	<0.01	0.03	0.03	0.02	<0.01	0.07	0.04
Hf	0.14	0.1	2.3	0.8	0.9	1.4	1.0	0.7	1.5
Ta	0.023	0.1	<0.1	<0.1	<0.1	<0.1	<0.1	<0.1	<0.1
W	0.05	0.5	<0.5	0.5	0.5	<0.5	<0.5	<0.5	<0.5
Tl	0.005	0.1	2.6	0.2	0.1	<0.1	0.3	0.1	<0.1
Pb	0.6	0.1	7.9	3.3	1.3	10.9	3.6	4.2	3.7
Bi	0.15	0.1	0.8	1.4	<0.1	0.7	0.7	1	0.3
Th	0.018	0.2	<0.2	<0.2	<0.2	<0.2	<0.2	<0.2	<0.2
U	0.011	0.1	<0.1	<0.1	<0.1	<0.1	<0.1	<0.1	<0.1

Table 7: continued.

Sample ID	H08-80-107.5	H11-05-45.55	H11-05-54.25	H11-08-52.65	H11-08-52.66	H11-08-58.3	H11-08-63.9	H11-13C-363	H11-13C-376.5
DDH	H08-80	H11-05	H11-05	H11-08	H11-08	H11-08	H11-08	H11-13C	H11-13C
Lithology	Exhalite	Exhalite	Exhalite	Exhalite	Exhalite	Exhalite	Exhalite	Exhalite	Exhalite
SiO2	84.35	21.56	5.01	7.19	5.73	3.57	9.16	52.01	9.10
TiO2	0.01	0.01		<0.01		0.02	0.01	0.01	0.01
Al2O3	0.47	0.19	0.26	0.18	0.15	0.39	0.44	0.21	0.19
Fe2O3T	9.59	56.44	71.69	76.37	58.6	68.58	71.18	35.11	62.19
MgO	0.71	1.96	2.27	0.64	0.53	0.41	2.30	2.04	1.04
MnO	0.12	0.19	0.17	0.39	0.32	0.83	1.73	1.87	0.86
CaO	1.25	1.50	0.97	2.23	1.85	1.26	4.15	6.22	2.74
Na2O	0.08	0.07	<0.01	0.06	0.01	0.06	0.06	0.03	0.06
K2O	0.06	0.03	<0.01	0.01	<0.01	0.02	0.01	0.07	0.03
P2O5	0.02	0.00	<0.01	0.01	<0.01	0.01	0.01	<0.01	0.01
LOI	3.2	17.7	19.00	13.0	32.7	25.1	10.2	2.40	23.10
CO2	0.15	0.23	0.09	3.95	0.13	0.49	3.30	1.49	10.70
S	6.46	32.2	28.71	10.6	40.05	0.04	20.1	1.84	0.78
Li		0.4		0.4		0.4	0.4		0.4
Be	1.0	0.2	<1	0.1	<1	0.1	0.3	2.0	0.4
Sc	1.0	1.1	1	1.1	<1	1.1	1.1	<1	1.1
Ti		53		43		103	81		60
V	<8	16.9	<8	1.8	<8	2.5	3.1	<8	4.6
Cr		11		4		3	3		3
Co	3.7	130.5	98.4	96.9	93.3	187.0	5.6	4.4	52.0
Ni	261.3	980.4	3985.8	399.8	366.8	1414.0	820.8	7.1	50.7
Cu	702.7	450.1	552.9	93.0	88.6	182.6	171.4	6.6	13.4
Zn	124	11	9	10	6	10	55	3	14
Ga	<0.5	0.48	<0.5	0.35	<0.5	0.54	0.84	<0.5	0.40
Rb	2.1	0.9	<0.1	0.2	<0.1	0.6	0.2	2.4	2.1
Sr	12.1	3.7	2.5	14.3	14.9	6.2	10.4	16.4	14.0
Y	2	8.3	3.5	1.9	1.7	1.1	3.7	8.5	4.8
Zr	3.9	6.0	22.4	6.0	2.3	6.0	6.0	2.9	6.0
Nb	0.30	0.04	<0.1	0.05	<0.1	0.17	0.18	0.1	0.13
Mo	0.3	0.16	0.6	0.79	0.4	1.24	0.76	0.6	1.82
Cd	0.3	0.04	<0.1	0.03	<0.1	0.04	0.07	<0.1	0.09
In		0.0091		0.0040		0.0042	0.0101		0.0049
Sn	<1	0.16	<1	0.16	<1	0.16	0.16	<1	0.16
Sb	<0.1	0.21	0.2	0.33	0.1	0.44	0.14	0.10	1.90
Cs	0.20	0.32	<0.1	0.06	<0.1	0.25	0.05	1.20	1.09
Ba	14	5	5	31	36	4	2	6	5
La	0.7	0.5	1.1	1.0	1.5	0.5	3.2	2.9	2.2
Ce	1.6	1.3	1.2	1.6	1.7	0.9	3.9	4.3	3.5
Pr	0.25	0.21	0.18	0.19	0.22	0.11	0.41	0.50	0.41
Nd	0.80	1.25	0.70	0.72	0.80	0.55	1.54	2.20	1.70
Sm	0.14	0.37	0.13	0.16	0.11	0.12	0.24	0.39	0.34
Eu	0.07	0.12	0.08	0.16	0.13	0.09	0.26	0.49	0.31
Gd	0.21	0.59	0.20	0.19	0.17	0.13	0.27	0.75	0.47
Tb	0.02	0.10	0.02	0.03	0.02	0.02	0.04	0.09	0.07
Dy	0.19	0.72	0.24	0.19	0.18	0.12	0.28	0.75	0.48
Ho	0.05	0.18	0.05	0.04	0.03	0.03	0.06	0.18	0.11
Er	0.17	0.59	0.20	0.15	0.12	0.08	0.21	0.60	0.38
Tm	0.02	0.09	0.03	0.02	0.01	0.02	0.03	0.08	0.05
Yb	0.25	0.58	0.20	0.14	0.13	0.09	0.20	0.59	0.36
Lu	0.02	0.09	0.03	0.02	<0.01	0.01	0.04	0.08	0.06
Hf	<0.1	<0.14	0.5	<0.14	<0.1	<0.14	<0.14	<0.1	<0.14
Ta	<0.1	0.02	<0.1	0.02	<0.1	0.02	0.02	<0.1	0.02
W	<0.5	0.06	0.7	0.07	<0.5	0.12	0.30	1.9	0.18
Tl	<0.1	0.04	<0.1	0.05	<0.1	0.10	0.03	<0.1	0.17
Pb	4.6	6.0	7.8	4.1	3.8	4.3	4.0	0.7	5.8
Bi	0.10	0.42	0.40	1.20	1.10	0.16	0.17	<0.1	0.15
Th	<0.2	0.05	<0.2	0.03	<0.2	0.06	0.07	<0.2	0.08
U	<0.1	0.03	<0.1	0.09	<0.1	0.08	0.11	<0.1	0.13

Table 7: continued.

Sample ID	H11-13C-378.7	H11-13C-387.2	H11-13C-389.45	H11-16-411.4	H11-13C-357.1	H11-16-399.1	H11-16-425.5	H11-16-480.6
DDH	H11-13C	H11-13C	H11-13C	H11-16	H11-13C	H11-16	H11-16	H11-16
Lithology	Exhalite	Exhalite	Exhalite	Exhalite	Graphitic Argillite	Graphitic Argillite	Exhalite	Graphitic Argillite
SiO2	29.77	41.73	6.91	86.23	10.52	33.97	7.15	60.43
TiO2	0.50	0.17	0.02	0.01	0.08	0.15	0.02	0.36
Al2O3	17.01	4.64	0.57	0.08	2.09	3.83	0.34	11.78
Fe2O3T	32.31	37.44	64.87	10.93	55.47	34.83	58.2	15.10
MgO	2.60	2.43	2.88	1.00	0.39	0.23	1.60	0.61
MnO	1.01	1.47	1.80	0.45	0.02	0.02	1.76	0.07
CaO	7.10	4.61	6.08	1.19	0.39	0.85	14.76	4.91
Na2O	0.39	0.05	<0.01	0.04	0.06	0.09	0.06	0.43
K2O	0.93	0.03	<0.01	0.02	0.53	1.15	0.13	1.52
P2O5	0.03	0.05	<0.01	0.01	0.02	0.03	<0.01	0.08
LOI	4.90	5.90	9.90	<0.05	30.50	24.70	6.40	4.60
CO2	0.48	4.12	2.49	7.22	2.31	17.60	3.71	5.74
S	30.30	0.79	21.30	0.01	47.40	30.50	11.13	6.25
Li	12.7	1.6		0.8	2.9	2.1		9.5
Be	1.6	0.3	<1	0.3	0.3	0.5	1.0	0.6
Sc	12.4	4.3	<1	1.1	1.9	5.7	<1	9.8
Ti	2733	921		30	494	849		1986
V	88.1	22.3	<8	2.4	12.1	42.0	<8	53.8
Cr	98	20		3	9	57		62
Co	3.0	4.4	4.3	1.2	89.6	168.0	3.4	37.8
Ni	30.1	41.0	67.1	6.9	49.5	254.8	42.8	144.8
Cu	2.1	14.2	32.8	3.5	29.1	205.3	14.7	72.0
Zn	142	41	12	17	206	734	17	8
Ga	20.32	5.49	<0.5	0.67	3.07	5.09	0.7	13.63
Rb	20.54	1.47	0.5	0.76	12.30	21.94	4.80	43.88
Sr	33.9	16.8	47.0	20.0	9.0	17.0	159.3	85.0
Y	19.36	8.43	5.30	1.22	3.83	10.15	5.30	16.15
Zr	144	50	16	6	27	41	5	117
Nb	5.94	1.95	<0.1	0.10	1.16	1.73	<0.1	4.68
Mo	0.51	2.46	0.60	0.16	4.69	10.90	0.80	1.65
Cd	0.09	0.10	0.10	0.02	0.29	1.15	0.10	0.03
In	0.06	0.05		0.00	0.03	0.10		0.14
Sn	2.00	0.53	<1	0.16	0.20	1.16	<1	2.26
Sb	0.37	0.19	0.30	0.09	2.85	9.19	0.30	0.93
Cs	1.77	0.53	0.20	0.31	0.35	0.50	1.80	0.78
Ba	221.0	4.1	3.0	8.5	63.2	82.5	21.0	158.9
La	18.98	8.7	2.2	1.4	3.3	6.8	2.7	11.7
Ce	35.1	16.5	2.7	2.3	7.3	15.5	3.4	24.9
Pr	4.07	1.96	0.31	0.25	0.93	2.04	0.38	3.12
Nd	14.87	7.70	1.20	1.01	3.65	8.44	1.80	12.45
Sm	2.58	1.46	0.18	0.17	0.72	1.72	0.21	2.76
Eu	1.71	0.66	0.21	0.09	0.29	0.88	0.24	0.72
Gd	2.57	1.30	0.35	0.16	0.69	1.62	0.46	2.79
Tb	0.43	0.19	0.06	0.02	0.11	0.26	0.06	0.44
Dy	2.88	1.19	0.38	0.11	0.67	1.68	0.41	2.73
Ho	0.59	0.25	0.11	0.02	0.14	0.36	0.11	0.55
Er	1.72	0.79	0.39	0.08	0.40	1.09	0.38	1.64
Tm	0.24	0.11	0.05	0.01	0.05	0.16	0.05	0.24
Yb	1.55	0.73	0.32	0.08	0.38	1.07	0.31	1.60
Lu	0.24	0.11	0.06	0.0	0.05	0.17	0.05	0.24
Hf	3.66	1.26	0.40	<0.14	0.66	1.11	0.10	2.90
Ta	0.51	0.15	0.10	0.02	0.09	0.15	<0.1	0.38
W	3.05	3.00	<0.5	0.14	0.55	1.77	0.70	0.63
Tl	5.26	0.29	0.2	0.01	7.70	3.04	<0.1	1.61
Pb	0.8	1.9	4.0	0.6	8.3	47.7	2.9	6.7
Bi	0.15	0.15	<0.1	0.18	0.16	4.62	<0.1	0.39
Th	2.58	1.09	<0.2	0.04	0.65	1.38	<0.2	2.08
U	0.77	0.43	0.1	0.10	0.36	0.47	0.2	0.59

Whole rock geochemistry data. Oxides and S in weight %, all others in ppm; MDL = Minimum detection limit

Table 8: Stable isotope data for sedimentary rocks in the Hart area.

SAMPLE ID	DDH/TRENCH	LITHOLOGY/ COMMENT	$\Delta^{33}S_{V\text{-}CDT}$	$\Delta^{34}S_{V\text{-}CDT}$	$\Delta^{33}S$	$\delta^{56/54}Fe_{IRM\text{-}14}$
			±0.3 (2σ)	±0.3 (2σ)	±0.02 (2σ)	±0.06 (2σ)
H07-10-66.35	H07-10	Exhalite	0.1	3.0	-1.37	-2.04
H07-10-73.6	H07-10	Exhalite	-3.4	-5.6	-0.55	-1.80
H07-10-86.85	H07-10	Exhalite	-3.1	-4.9	-0.54	-1.91
H07-56-188.9	H07-56	Exhalite	-0.6	0.7	-0.95	-1.63
H07-56-210.6	H07-56	Exhalite	0.5	2.4	-0.70	-2.13
H08-106-98.6	H08-106	Exhalite	0.6	2.4	-0.69	
H08-80-103.2	H08-80	Exhalite	-2.5	-4.1	-0.42	-1.60
H08-80-107.5	H08-80	Exhalite	-4.4	-7.6	-0.54	-1.60
H11-05-45.55	H11-05	Exhalite	-5.2	-9.0	-0.58	-1.22
H11-05-54.25	H11-05	Exhalite	2.1	5.5	-0.74	-1.40
H11-08-52.65	H11-08	Exhalite	-6.3	-11.4	-0.46	-2.04
H11-08-58.3	H11-08	Exhalite	-5.3	-9.3	-0.45	-1.75
H11-08-63.9	H11-08	Exhalite	3.2	7.6	-0.66	
H11-13C-363	H11-13C	Exhalite	0.6	2.1	-0.46	-1.36
H11-13C-376.5	H11-13C	Exhalite	-3.4	-5.2	-0.75	-1.90
H11-13C-378.7	H11-13C	Exhalite	0.6	2.6	-0.79	-1.73
H11-13C-387.2	H11-13C	Exhalite	-0.5	-0.3	-0.34	-1.96
H11-13C-389.45	H11-13C	Exhalite	-0.4	0.2	-0.43	-2.08
H11-16-411.4	H11-16	Exhalite	-0.1	0.7	-0.44	-0.85
H11-16-425.5	H11-16	Exhalite	-1.4	-1.7	-0.49	-1.45
MGH502	MGH502	Exhalite	-6.2	-11.0	-0.53	
MGH600A	MGH600	Exhalite	-2.1	-2.8	-0.66	
MGH600B	MGH600	Exhalite	2.1	5.5	-0.73	
MGH601B	MGH601	Exhalite	-5.8	-10.0	-0.61	
H11-13C-357.1	H11-13C	Graphitic Argillite	0.9	3.5	-0.94	-1.86
H11-16-399.1	H11-16	Graphitic Argillite	0.6	1.6	-0.19	-1.96
H11-16-480.6	H11-16	Graphitic Argillite	2.3	5.0	-0.28	-1.66

4.6 RESULTS

4.6.1 MAJOR AND TRACE ELEMENT GEOCHEMISTRY

Major element variations generally reflect the lithology and dominant mineralogy, with chert-rich and iron oxide-rich varieties having high SiO_2 and Fe_2O_3 contents (Table 7). Some samples have compositions controlled by the abundance of pyrrhotite and pyrite, with high Fe_2O_3 and SO_2, but low SiO_2. In general, low concentrations of TiO_2 and Al_2O_3 are found in all samples of exhalite, with the exception of high Al_2O_3 (17.01 wt.%) found in a sample of silicate-rich iron formation with high sulfide content. Notably, all exhalite samples are enriched in MnO above the crustal levels of ~0.1 wt. % (Rudnick and Gao, 2014) with values as high as 1.87 wt.%. Graphitic argillite samples have extremely variable compositions depending on the abundance of graphite, pyrite, and silicate minerals.

Several trace element concentrations, and rare earth element patterns and anomalies in chemical sediments, including cherts and iron formations, have been used to describe the composition and redox state of the ancient water column in recent publications (e.g., Bolhar et al., 2004; Barrie, 2005; Kato et al., 2006; Frei et al., 2008; Bekker et al., 2014; Planavsky et al., 2010; Thurston et al., 2012). Graphitic argillite samples from the Hart area typically have low, but variable, Zn concentration, with the range of values from 3 to 734 ppm. Mo concentrations of 0.3 to 10.9 ppm are also comparable to data for shales of similar age (Scott et al., 2008). Importantly, almost all samples have Mo concentrations above average crustal levels of 1 to 2 ppm (Rudnick and Gao, 2014). In addition, concentrations of U are also very low compared to crustal average: 0.03 to 0.77 ppm (with the average of 0.22 ppm) for exhalite, and 0.36 to 0.59 ppm (with the average of 0.47 ppm) for graphitic argillite, which is below various estimates for average crustal levels of 1.5 to 2.8 ppm (see Rudnick and Gao, 2014).

The abundances of rare earth elements have been normalized to the Post-Archean average Australian Shale (PAAS) as it is the most commonly used reference for normalizing similar lithologies, allowing for

easy comparison to previous work (Figure 25; refer to Table 9 for data and formulas used to calculate anomalies). The exhalite has generally positive anomalies for Eu and Y (Figure 25b). A significant positive Eu anomaly (Eu/Eu*; see Table 9 for method of calculation of REE anomalies), ranging from 1.2 to 8.1, is found in all exhalite samples. Exhalite samples have a wide range of Ce anomalies, both positive and negative, with values ranging from 0.41 to 1.30, with positive Ce anomalies not created as an artifact of a positive La anomaly influencing the calculation (Figure 25a; Table 9). Values for Y/Ho ratio have a wide range from 32.6 to 70.0, but are generally superchondritic, similar to those found in seawater (Bolhar et al., 2004). The rare earth element (REE) patterns also show a general heavy-REE (HREE; Figure 26b) enrichment as indicated by normalized Pr/Yb and Gd/Yb ratios ranging from 0.12 to 0.99 and 0.51 to 1.76, respectively, similar to modern hydrogenous chemical sediments (Table 7; Bau, 1999).

The graphitic argillites lack significant anomalies for Ce and Y, but have positive Eu anomalies (1.28 to 2.55; see Figure 26). Values for Y/Ho have a narrow range from 27.3 to 29.0 and are lower than those for modern seawater and close to those of chondrites (~26), indicating limited uptake of REE from seawater. The rare earth element (REE) data for graphitic argillites also shows a predominantly flat pattern (Figure 26b), with only weak HREE enrichment as shown by normalized Pr/Yb and Gd/Yb values ranging from 0.92 to 1.09 and 0.61 to 0.78, respectively (Table 9).

4.6.2 Petrography and SEM

High Mn concentrations within the exhalite unit were further investigated to determine the mineral host of Mn. The EDS analyses of exhalite samples found that Mn was hosted predominantly in carbonates, chlorite, and actinolite (Figure 27). No significant Mn enrichment was observed in sulfides and oxides. The presence of Mn in carbonates and metamorphic silicates, without significant enrichments in sulfides and oxides, suggests that Mn was not likely to have been hosted in the oxyhydroxides during early

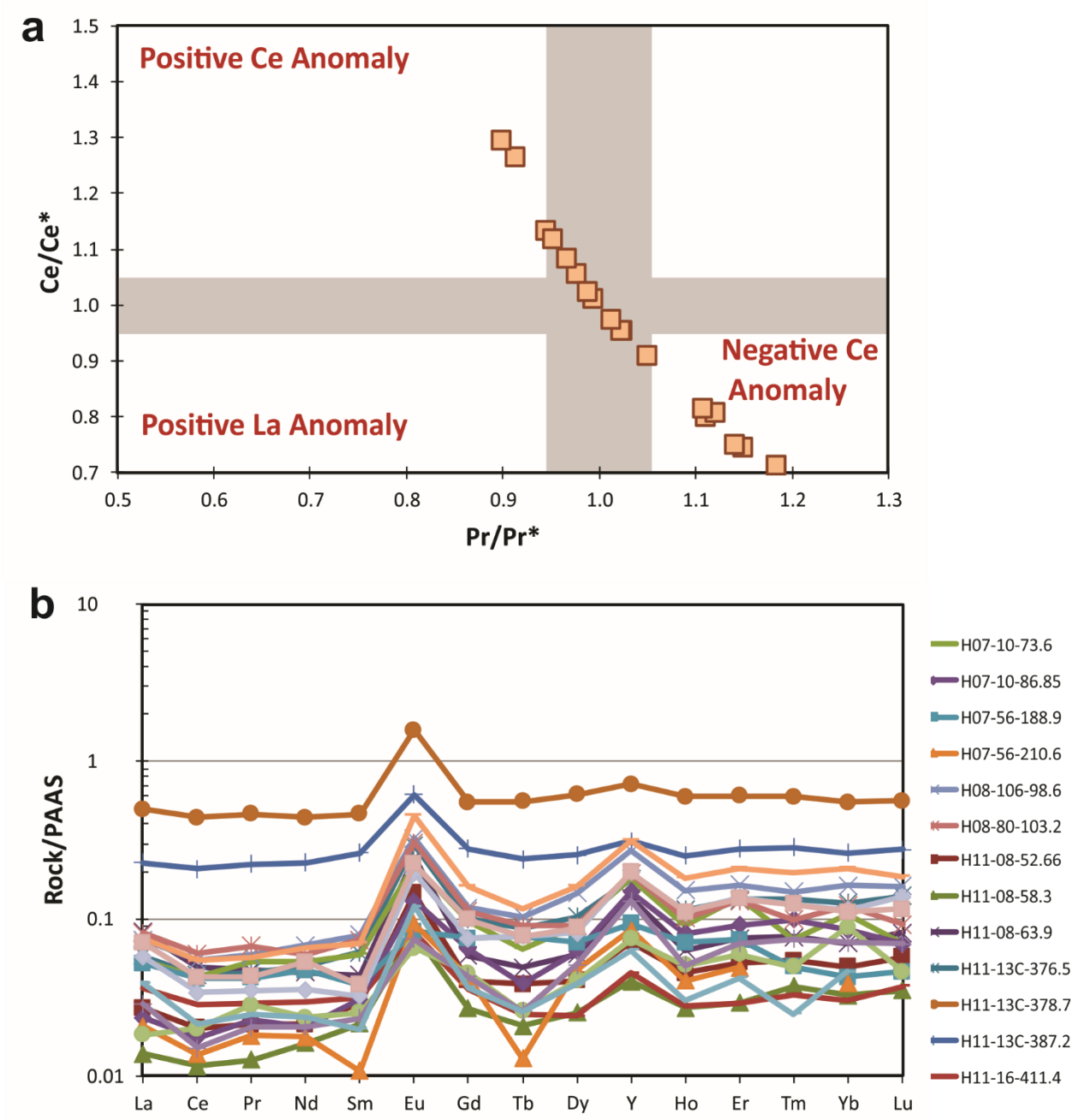

Figure 25: a) Ce and La anomalies, grey field represents non-anomalous values, and b) rare earth element patterns of exhalite samples.

Table 9: Calculated REE anomalies in the sedimentary rocks of the Hart area.

		H11-05-45.55	H11-08-52.66	H11-08-58.3	H11-08-63.9	H11-13C-376.5	H11-13C-378.7	H11-13C-387.2	H11-16-411.4
Anomaly	Formula used to Calculate Anomaly	Exhalite	Exhalite	Exhalite	Exhalite	Exhalite	Exhalite	Exhalite	Exhalite
La	La/(3Pr - 2Nd)*	-5.566	1.272	2.476	1.656	1.565	0.980	1.070	1.362
Ce	Ce/(2Pr - Nd)*	1.469	0.954	1.264	1.011	1.054	0.910	0.953	1.024
Pr	Pr/(1/2Ce + 1/2Nd)*	0.905	1.024	0.913	0.994	0.976	1.050	1.023	0.989
Eu	Eu/(2/3Sm + 1/3Tb)*	1.205	4.546	3.856	5.335	4.171	3.214	2.406	2.817
Gd	Gd/(2Tb - Dy)*	1.171	1.122	1.632	1.503	1.386	1.124	1.237	1.399
Y/Ho		45.760	42.953	40.000	58.347	42.933	32.598	33.720	43.885
Gd/Yb*		0.625	0.817	0.822	0.831	0.794	1.003	1.067	1.182
Pr/Yb*		0.117	0.429	0.389	0.668	0.364	0.838	0.849	0.954
		H07-10-66.35	H07-10-73.6	H07-10-86.85	H07-56-188.9	H07-56-210.6	H08-106-98.6	H08-80-103.2	H08-80-107.5
Anomaly	Formula used to Calculate Anomaly	Exhalite	Exhalite	Exhalite	Exhalite	Exhalite	Exhalite	Exhalite	Exhalite
La	La/(3Pr - 2Nd)*	0.610	1.028	0.884	1.672	1.104	1.789	0.984	0.486
Ce	Ce/(2Pr - Nd)*	0.408	0.801	0.713	1.132	0.745	1.082	0.808	0.609
Pr	Pr/(1/2Ce + 1/2Nd)*	1.503	1.111	1.185	0.945	1.150	0.966	1.120	1.296
Eu	Eu/(2/3Sm + 1/3Tb)*		3.634	3.891	1.636	8.047	3.715	3.851	2.549
Gd	Gd/(2Tb - Dy)*		2.447	4.139	0.889	-2.027	1.922	1.224	4.067
Y/Ho			54.444	50.000	35.714	57.500	48.667	52.000	40.000
Gd/Yb*		0.968	0.908	0.756	1.765	1.100	0.724	0.926	0.508
Pr/Yb*		0.766	0.500	0.266	0.985	0.465	0.361	0.554	0.319
		H11-05-54.25	H11-08-52.66	H11-13C-363	H11-13C-389.45	H11-16-425.5	H11-13C-357.1	H11-16-399.1	H11-16-480.6
Anomaly	Formula used to Calculate Anomaly	Exhalite	Exhalite	Exhalite	Exhalite	Exhalite	Graphitic Argillite	Graphitic Argillite	Graphitic Argillite
La	La/(3Pr - 2Nd)*	1.450	1.425	1.894	1.668	3.085	0.867	0.915	0.940
Ce	Ce/(2Pr - Nd)*	0.749	0.814	1.117	0.974	1.295	0.895	0.916	0.920
Pr	Pr/(1/2Ce + 1/2Nd)*	1.141	1.108	0.952	1.013	0.898	1.054	1.041	1.040
Eu	Eu/(2/3Sm + 1/3Tb)*	3.058	5.520	5.309	4.110	4.363	2.013	2.550	1.280
Gd	Gd/(2Tb - Dy)*	107.961	2.760	2.226	1.017	1.464	1.062	1.082	1.087
Y/Ho		70.000	56.667	47.222	48.182	48.182	27.338	27.740	29.021
Gd/Yb*		0.605	0.791	0.769	0.662	0.898	1.090	0.915	1.036
Pr/Yb*		0.287	0.540	0.271	0.309	0.391	0.776	0.608	0.613

***Calculated using PAAS-normalized values**

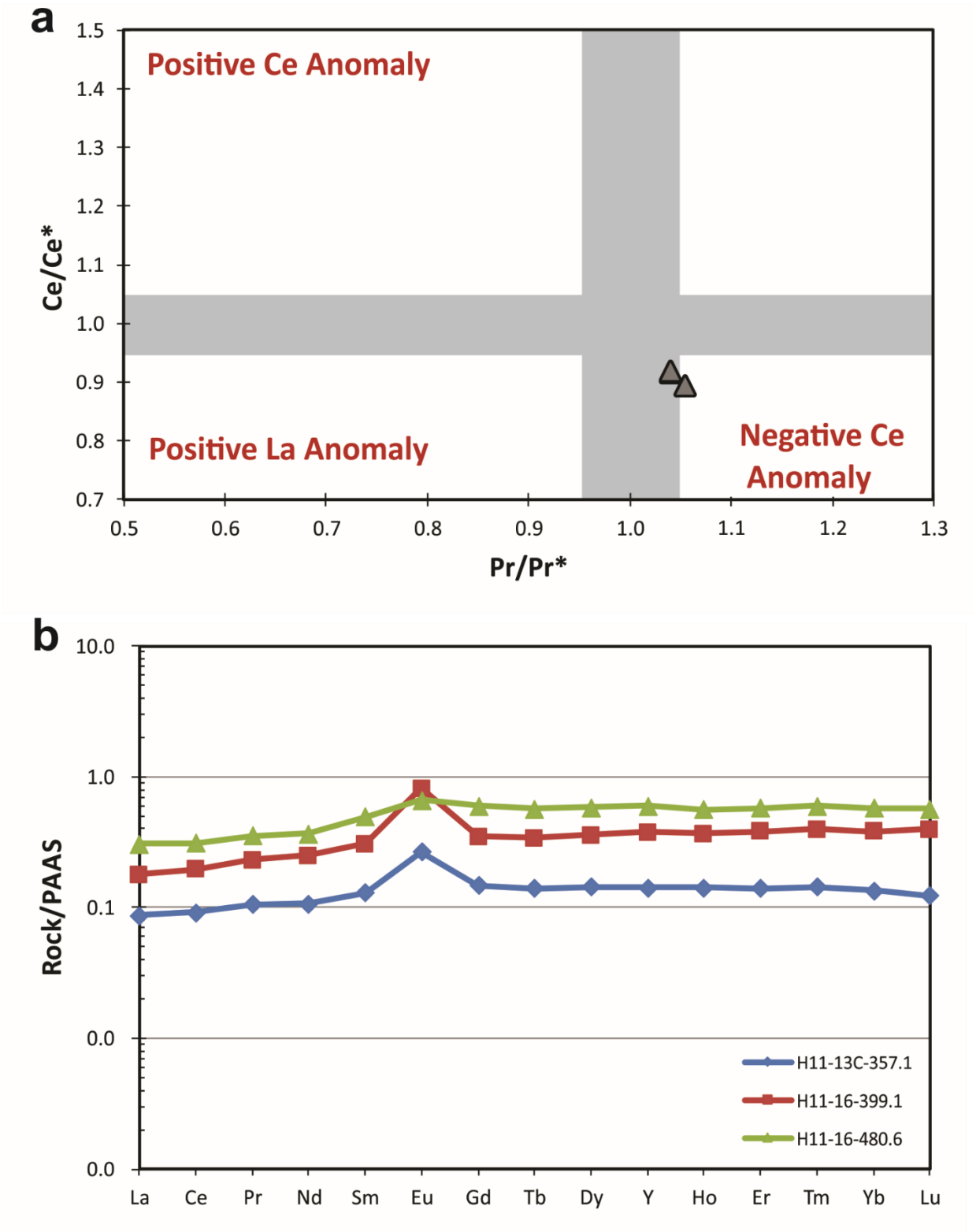

Figure 26: a) Ce and La anomalies, grey field represents non-anomalous values, and b) rare earth element patterns of graphitic argillite samples.

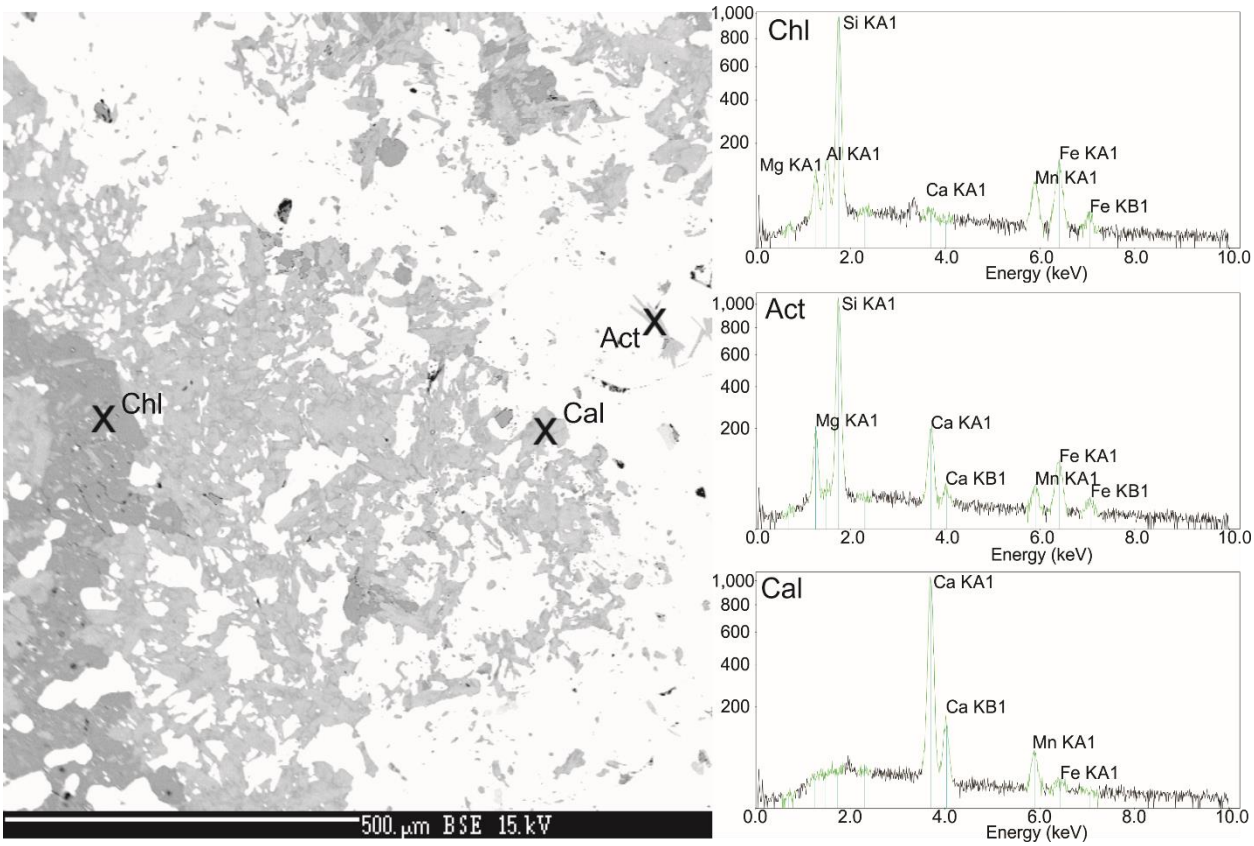

Figure 27: Back-scattered electron image of exhalite sample H11-08-63.9 showing the Mn-bearing minerals and the EDS spectra. Chl: chlorite, Act: actinolite, Cal: calcite. White minerals on image are denser Fe-oxide and sulfide minerals.

diagenesis, but may have been adsorbed to the surface of clay minerals and later incorporated into diagenetic carbonates.

4.6.3 Stable Isotopes

Sulfur isotope data have been used as a tracer of biological activity in modern and ancient aqueous environments, and, in the case of Archean rocks, also contain a record of atmospheric reactions (e.g., Farquhar et al., 2000; Ono et al., 2003, 2009). On a plot of $\delta^{34}S$ against $\delta^{33}S$ values for sediments from the Hart area, the data forms a trend offset from, but generally parallel to the terrestrial fractionation line (TFL) that follows mass-dependent fractionation (Figure 28a). The offset from the TFL is due to non-mass dependent fractionation in the Archean atmosphere (Farquhar et al., 2000), and the magnitude and consistency of this offset is expressed on a plot of $\delta^{34}S$ against $\Delta^{33}S$, where values along the TFL would plot with $\Delta^{33}S = 0‰$ (Figure 28b).

Exhalite samples have a large range of $\delta^{34}S$ values, -11.4 to +7.6‰ (n=24), and an average value of -2.1‰ (Figure 28b; Table 8). The $\Delta^{33}S$ values have a much smaller, and consistently negative, range from -1.37 to -0.34‰, with an average value of -0.62‰.

Graphitic argillite samples have much more restricted range of $\delta^{34}S$ values than the exhalite, with the range of +1.6 to +5.0‰ (n=3). This positive range, although overlapping with that of the exhalite, has a positive average value of +3.4‰, significantly different from that of the exhalite. The $\Delta^{33}S$ values of the graphitic argillite have a small, and consistently negative, range, similar to that of the exhalite, -0.94 to -0.19‰, with an average value of -0.47‰ (Figure 28b). This suggests that sulfur in sulfides in the graphitic argillite was likely derived from the same sulfate source as the exhalite sulfides.

The bulk-rock $\delta^{56}Fe$ values of both the exhalite and graphitic argillite are systematically negative. The exhalite exhibits a range of -2.13 to -0.85‰ (n=18), with an average value of -1.69‰. The graphitic argillite exhibits a range of -1.96 to -1.66‰ (n=3), with an average value of -1.82‰ (Figure 29).

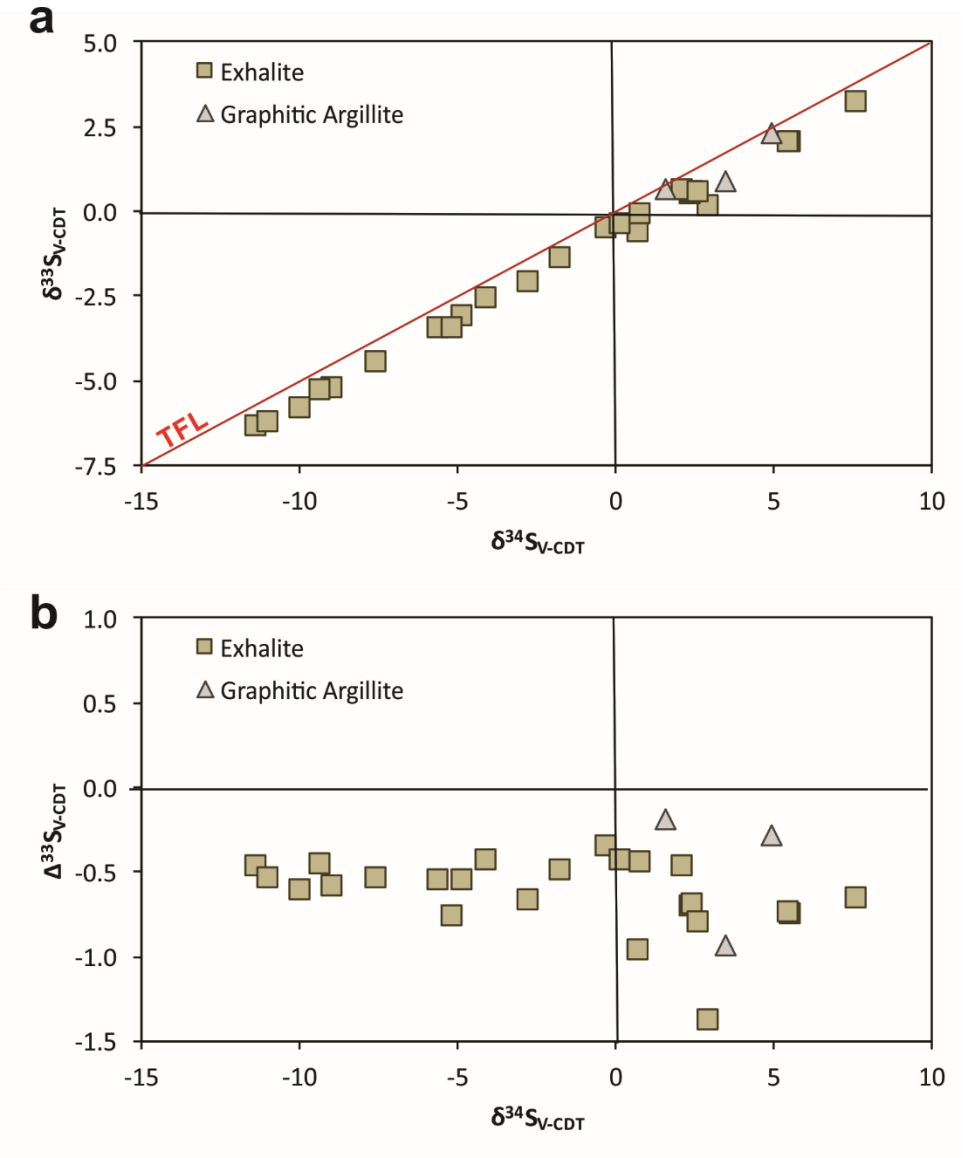

Figure 28: Sulfur isotope signatures of the Hart area exhalite and graphitic argillite. Red line in (a) indicates terrestrial fractionation line. Terrestrial fractionation line would correspond to $\Delta^{33}S=0$ jn (b).

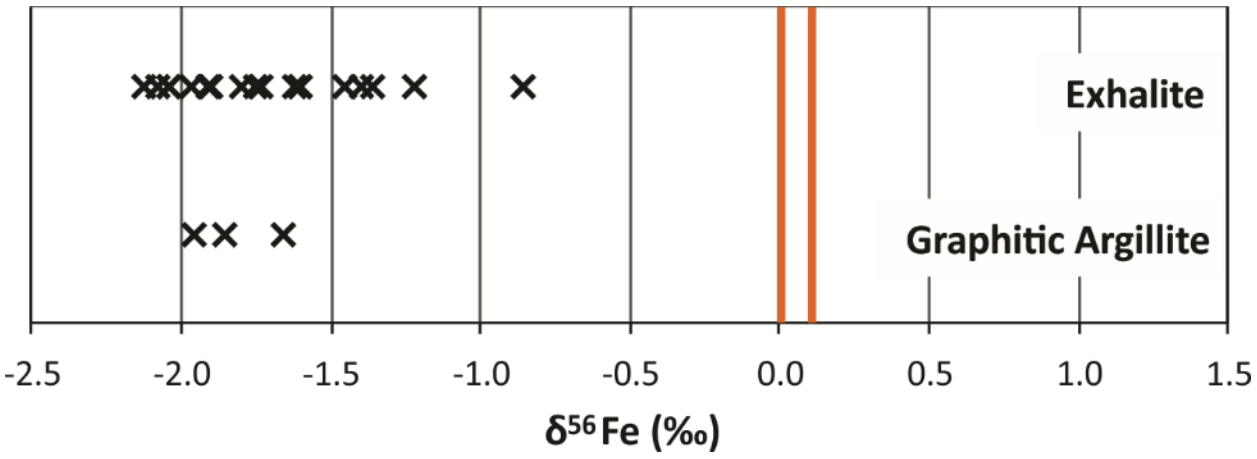

Figure 29: Fe-isotope composition of the lithologies present in the Hart deposit area. Orange represents the minimum and maximum values of the mantle range (Beard et al., 2003).

Considering that co-existing Fe-bearing minerals in such samples may have distinctly different $\delta^{56}Fe$ values, it is important to relate bulk-rock $\delta^{56}Fe$ signature and mineralogy. For example, the various proportions of isotopically light pyrite (or isotopically heavy Fe-oxides) and lithogenic components with $\delta^{56}Fe$ = 0.09‰ may produce a significant range in bulk $\delta^{56}Fe$ values (e.g., Duan et al., 2010; Severmann et al., 2008; Rouxel et al. 2016). As shown in Figure 30, there is no significant correlation between $\delta^{56}Fe$ values and S concentration, suggesting that variations in $\delta^{56}Fe$ are not a result of mixing between isotopically light pyrite and lithogenic components.

4.7 Discussion

4.7.1 Environmental Implications of Major and Trace Element Data

Generally low TiO_2 and Al_2O_3 concentrations in the exhalite unit indicate low detrital input (cf. Slack et al., 2007), and, when plotted against each other (Figure 31a), show no apparent trend. Similarly, Zr versus TiO_2 plot shows no apparent trend (Figure 31b). The trends found within the graphitic argillite data, however, show the expected pattern for detrital contribution to sediments (Figures 31a and b; cf. Pecoits et al., 2009). When recalculated to elemental weight percent, ratios of Fe/Ti and Al/(Al+Fe+Mn) can be used to show a continuum between the exhalite and graphitic argillite units, suggesting precipitation from a mixture of hydrothermal fluids and seawater for exhalite, and some influence of hydrothermal fluids on the predominantly detrital material in the graphitic argillite (Figure 31c; cf. Bonatti et al., 1972; Böstrom et al., 1969; Böstrom, 1973; Pecoits et al., 2009).

The trace element concentrations and ratios, and rare-earth element anomalies in the Hart area sediments provide insight into the composition and redox state of the water column at their depositional site (e.g., Bolhar et al., 2004; Kato et al., 2006; Frei et al., 2008; Bekker et al., 2010; Planavsky et al., 2010; Thurston et al., 2012). When compared to data for Precambrian shales (Robbins et al., 2013; Scott et al., 2008; 2013), the low Zn and Mo concentrations in graphitic argillites from the

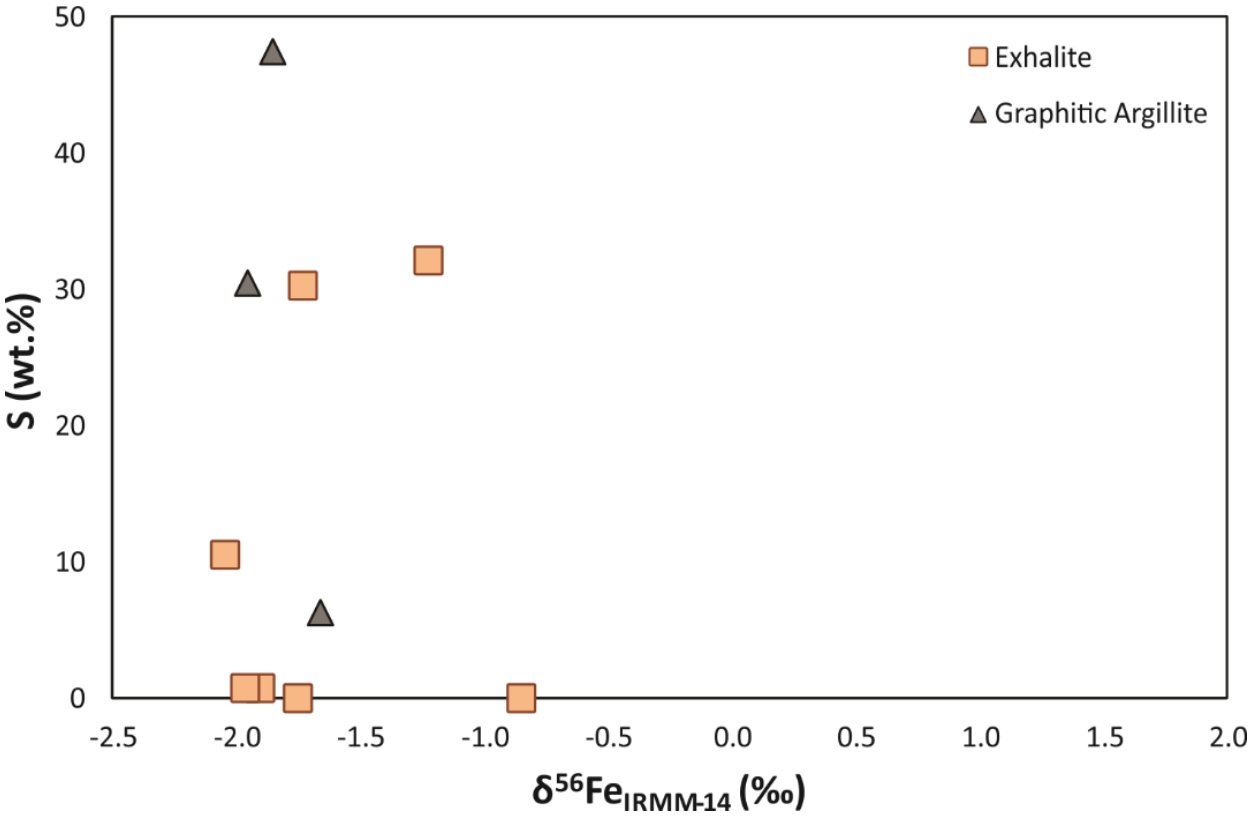

Figure 30: Plot of S concentration vs $\delta^{56}Fe$ shows no correlation, indicating that Fe isotope values are not controlled by sulfide content.

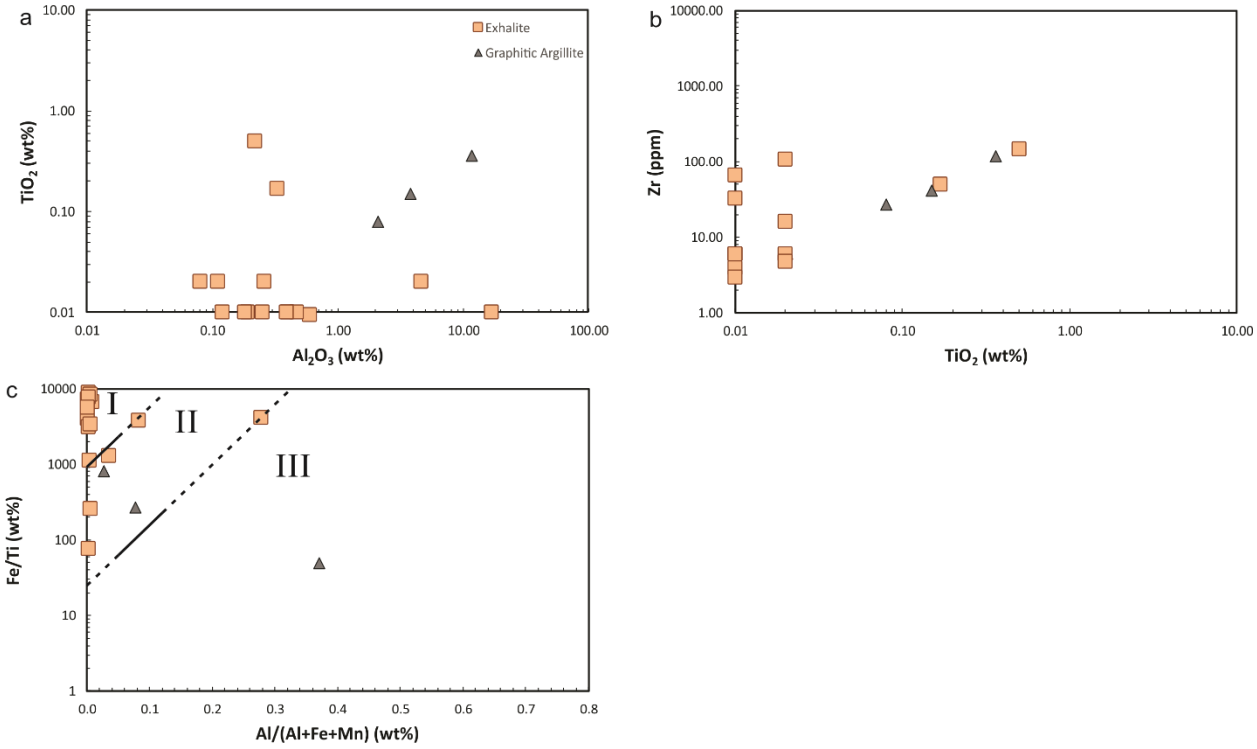

Figure 31: Diagrams designed to test the significance of detrital input on sedimentary rocks. A positive correlation in (a) and (b) indicates some compositional control by detrital material on the graphitic argillite. In (c), plotting in zone I indicates a dominantly hydrothermal source for sediments, plotting in zone II indicates some influence of a hydrothermal source mixed with detrital material, and plotting in zone III indicates a dominantly detrital source. Fields from Pecoits et al. (2009).

Hart area, and the ratio of Zn (ppm)/Al_2O_3 (wt.%) fall within the range of values compiled by Scott et al. (2008, 2013) for organic-rich shales deposited in the anoxic Archean oceans.

Partin et al. (2013a, b) evaluated U concentrations and authigenic U enrichment (U_{auth}=U – Th/3) in the Archean, prior to the rise of atmospheric oxygen, for both iron formations and black shales. In the Archean iron formations, before the rise of atmospheric oxygen between ca. 2.45 and 2.32 Ga (e.g., Bekker et al., 2004; Gumsley et al., 2017), very low U concentrations and U_{auth} enrichments were found (Partin et al., 2013a), and in the Hart exhalites U concentrations are comparable to the typical values found in the similar Archean deposits (Barrie, 2005; Partin et al., 2013a). In the Archean black shales, Partin et al. (2013b) found average U concentration and U_{auth} enrichment of 3.8 ppm and 0.9 ppm, respectively. Graphitic argillites from the Hart area have U concentrations well below the average value for the Archean shale (Partin et al., 2013b). Low, pre-GOE (Great Oxidation Event) levels are also observed in our samples for other trace elements such as Co (cf. Swanner et al., 2014), and Cr (cf. Konhauser et al., 2011). Combined, this trace element dataset suggests deposition under a generally anoxic water column, although the rapid precipitation of Fe in modern hydrothermal settings (e.g., in distal part of hydrothermal plume where seafloor microbial mats grow) would be also consistent with such signatures (Rouxel et al., 2016, 2018). However, Mn concentrations in exhalite samples are anomalously high for anoxic environments. The possible link between Mn enrichment and localized oxygenated oases in the Archean ocean, proposed in previous studies (cf. Olson et al., 2013; Ossa Ossa et al., 2016; Planavsky et al., 2014), is discussed in more detail below.

Positive La, Gd, and Y anomalies have been observed in the modern seawater and have been explained by REE complexation on particle surfaces (e.g., Bolhar et al., 2004). The positive Eu anomalies are common in Archean sediments, and have been interpreted to represent strong influence of high-temperature, hydrothermal, anoxic fluids on seawater composition during that time (e.g., Bau and

Dulski, 1996; Bolhar et al., 2004; Slack et al., 2007; Bekker et al., 2010, 2014; Planavsky et al., 2010). By analogy, positive Eu anomalies of the Hart area exhalite indicate influence of hydrothermal fluids on seawater composition at the depositional site and, potentially, relative proximity to high-temperature hydrothermal vents. The rare-earth element (REE) patterns of the Hart area exhalites also show a general heavy-REE (HREE; Figure 25b) enrichment as indicated by normalized Pr/Yb and Gd/Yb values ranging from 0.27 to 0.99 and 0.51 to 1.76, respectively (Table 9). These Pr/Yb values overlap with higher values within the range reported for Abitibi BIFs by Thurston et al. (2012), which were interpreted to characterize BIFs formed in shallower water than those with lower Pr/Yb ratios (Kamber, 2010; Thurston et al., 2012). Combined, these REE characteristics of the Hart area exhalites record seawater composition dominated by high-temperature hydrothermal flux.

In modern environments, negative Ce anomalies are generated under oxidizing conditions in river waters and seawater, but are dominantly produced by Ce scavenging onto Fe-Mn nodules and crusts in deep, oxygenated ocean waters (Bau and Dulski, 1996; Bau, 1999; Slack et al., 2007). As the deep seawater was unlikely to have been oxygenated during the Archean, fractionation may have occurred locally in environments where REE were scavenged by Fe-Mn particles. The presence of small, true positive and negative Ce anomalies in the exhalite samples could suggest redox cycling of REE coupled to formation and dissolution of Fe-Mn oxyhydroxides. Following the model of German et al. (1991) and Slack et al. (2007), Fe-Mn-rich particles generated in local, shallow oxidized environments (and producing negative Ce anomalies in the upper part of the water column) would have been dissolved below the redoxcline in deeper waters, returning the Ce back to the seawater and erasing any negative Ce anomaly, or even producing a positive Ce anomaly. Whether a similar mechanism could operate in hydrothermal plume-influenced environments remains, however, poorly constrained.

The near-chondritic values of Y/Ho for the graphitic argillite are lower than those for the modern seawater and the Hart area exhalites, suggesting that their REE composition is dominated by a detrital signal. Positive Eu anomalies however suggest that significant hydrothermal flux continued during deposition of the graphitic argillite.

4.7.2 Formation of the Graphitic Argillite Unit

The negative $\delta^{56}Fe$ values in the graphitic argillite unit are surprising considering the high abundance of detrital/lithogenic material. As mentioned above, the lack of correlation between S and $\delta^{56}Fe$ values suggests that the range of $\delta^{56}Fe$ values is not solely explained by the contribution of isotopically light Fe-sulfides (i.e., mixing between lithogenic and sulfide components). This likely implies that the Fe incorporated into sulfides and other authigenic (including silicate minerals) phases was derived from water masses with isotopically light Fe as is also envisioned for the exhalite deposits except that there was stronger influence of hydrothermal plumes on water masses from which Fe-oxyhydroxides precipitated to form the exhalite. The abundance of carbon in graphitic argillite unit suggests deposition in an area of high organic productivity, possibly in a zone of upwelling from deeper part of the ocean basin. Low P concentrations, which are lower than expected for modern sediments deposited in areas of high biological productivity, are common to Archean organic matter-rich shales (e.g., Reinhard et al., 2017), suggesting that upwelling zones before the GOE did not receive large amounts of P from deep oceans (Bjerrum and Canfield, 2002).

4.7.3 Formation of the Exhalite Unit

The exhalite unit in the Hart area has many characteristics that distinguish it from typical iron formation. The chert-rich nature with generally low Fe-oxide abundances and abnormally high sulfide and manganese contents suggest that the processes involved in the genesis of the exhalite unit may also differ from those for typical iron formations.

As described by Klein (2005), Beukes and Gutzmer (2008), and Bekker et al. (2010), the general model for the genesis of iron formation can be summarized as follows:

- Dissolution of Fe from the oceanic crust by hydrothermal fluids and its delivery to the oceans.
- Precipitation of Fe-oxyhydroxides, following oxidation of Fe indirectly by oxygenic photosynthesis or directly by anoxygenic photosynthesis, siderite, or Fe-rich clays from ambient waters.
- Development of chert hardgrounds via infilling of pores or sediment replacement during early diagenesis at the sediment-water interface when delivery of iron and deposition of iron compounds slowed or stopped.

This sequence of events typically produced a combination of geochemical characteristics in iron formations such as: high Y/Ho ratio and positive Eu anomaly, which reflect transport and precipitation from aqueous solutions with a strong hydrothermal input (Bolhar et al., 2004), slight HREE enrichment (Bolhar et al., 2004; Planavsky et al., 2010), and positive δ^{56}Fe values reflecting oxidation of Fe prior to deposition (Rouxel et al., 2005; Bekker et al., 2010; Planavsky et al., 2012). Iron formations should also have little to no synsedimentary sulfide present since iron formations reflect ferruginous rather than euxinic water column conditions (Bekker et al., 2010).

The geochemistry and petrography of the exhalite unit in the Hart area suggests a somewhat different genesis. The negative, and highly variable, δ^{56}Fe values from all samples, including those that resemble typical iron formation, are more commonly associated with sulfides from Archean organic matter-rich sediments or carbonate-facies iron formations than oxide-facies iron formations (e.g., Dauphas et al., 2017). Previous studies of Fe isotope fractionation have shown that precipitation of Fe-sulfides from Fe^{2+} dissolved in an aqueous solution produces fractionations between -0.3 and -0.9‰ in the temperature

range of 2 to 40°C (Butler et al., 2005). Under hydrothermal conditions, non-equilibrium Fe isotope fractionation between pyrite in hydrothermal chimneys or Fe-sulfides in buoyant hydrothermal plume and hydrothermal fluid has been found to be about -0.9‰ (Rouxel et al., 2008; Bennett et al., 2009; Rouxel et al., 2016). This suggests that the observed $\delta^{56}Fe$ values of -2.0‰ in graphitic argillite and -2.1‰ in exhalite were formed as a result of an additional pathway to decrease the $\delta^{56}Fe$ value of the water prior to precipitation of Fe-oxides in the exhalite unit, and are unlikely to have been formed just by equilibrium or kinetic isotope fractionation during mineral precipitation in an open aqueous system. Two mechanisms have been proposed to produce isotopically light Fe^{2+} in solution, which could be recorded by Archean sedimentary rocks: 1) dissimilatory iron reduction in pore waters by bacteria (Yamaguchi et al., 2005; Archer and Vance, 2006; Heinman et al., 2010), and 2) reservoir effect resulting in Rayleigh-type fractionation due to the early precipitation of isotopically heavy Fe-oxides (Rouxel et al., 2005; Planavsky et al., 2012). A similar model based on Rayleigh fractionation of Si isotopes was proposed by van den Boorn et al. (2010) to explain isotopic patterns in some Archean cherts.

On a plot of Mn/Fe versus $\delta^{56}Fe$ (Figure 32), no significant correlation is observed within the Hart data alone. However, when plotted with data from other Archean and early Paleoproterozoic iron formations (e.g., Tsikos et al., 2010; Planavsky et al., 2012, 2014), the exhalite data fits to a general pattern with Mn-enriched samples (Mn/Fe > 0.01) having essentially negative $\delta^{56}Fe$ values, and Mn-depleted samples (Mn/Fe < 0.001) having positive $\delta^{56}Fe$ values. The apparent dichotomy in $\delta^{56}Fe$ values between Mn-enriched and Mn-depleted samples is observed throughout several Archean to Paleoproterozoic units and is also observed in modern seafloor hydrothermal deposits (Rouxel et al., 2018). Although mechanisms for separation of Mn and Fe and for Fe isotope fractionation could have differed between pre-GOE and post-GOE deposits, the observed relationships between Mn/Fe and $\delta^{56}Fe$ values might be attributed to the increasing oxidation potential of the water column, leading to significant oxidation of Fe first and then Mn. An increase in oxidation potential could explain why Mn/Fe ratios negatively

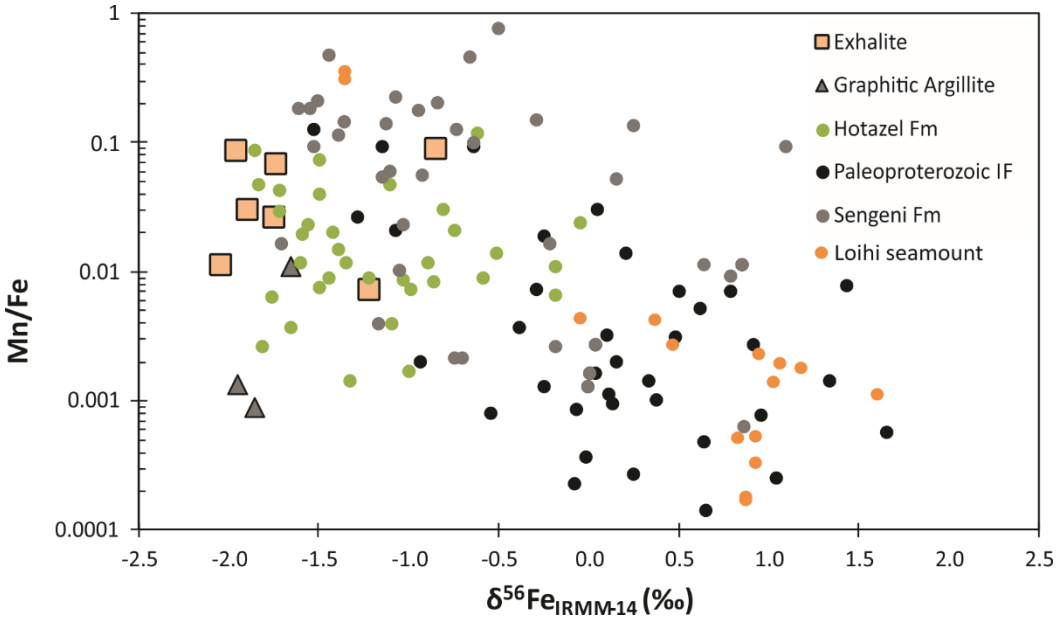

Figure 32: Exhalite data from this study broadly follows he same negative correlation trend as observed from several iron formations through time, including the Hotazel Formation, Botswana (Tsikos et al., 2010), the Senqeni Formation, South Africa (Planavsky et al., 2014), and a collection of well preserved Archean and Paleoproterozoic iron formation compiled by Planavsky et al. (2012).

correlate with $\delta^{56}Fe$ values, which might reflect extensive precipitation of isotopically heavy Fe-oxides in less oxidized settings. This process has been invoked for modern Fe-rich hydrothermal systems associated with volcanic seamounts such as Loihi (Rouxel et al., 2018). Additionally, although Eu anomalies are relatively large, the observed Eu anomalies in the Hart area are lower than the highest values recorded for BIFs and cherts from the Abitibi greenstone belt (as high as 31 in Thurston et al., 2012). As these Eu anomalies are generally attributed to the influence of hydrothermal input (e.g., Bolhar et al., 2004), the exhalite in the Hart area likely formed distally from the hydrothermal source relative to some of the BIFs sampled by Thurston et al. (2012).

Applying this model to the Hart deposit exhalite unit (Figure 33) would suggest that both Fe-oxides and Fe-sulfides formed in distal hydrothermal plume environments, after significant iron depletion from solution. Precipitation of a relatively small amount of Fe-rich minerals with highly negative Fe isotope values, along with deposition of a small amount of clay minerals enriched in Mn-oxyhydroxides and Mn-oxides that were later reacted with organic matter to form Mn-carbonates, was followed by formation of chert hardgrounds developed in pores at or below the sediment-water interface and as a replacement of sediments. The observed positive anomalies for La, Gd, and high Y/Ho ratios all suggest precipitation from seawater, whereas both positive and negative Ce anomalies, pronounced positive Eu anomaly, high Fe/Ti, and low Al/(Al+Fe+Mn) ratios together suggest variable redox conditions in a deep-water setting straddling the redoxcline with strong hydrothermal input at the time of deposition (cf. Bolhar et al., 2004; Pecoits et al., 2009).

Petrographic evidence suggests that, following precipitation of chert, locally Fe-rich laminae were replaced by sulfides, as indicated by variable magnetite and pyrrhotite contents along laminae over 5 – 10 mm length. However, individual grains of magnetite do not show textures suggesting replacement by sulfides. This could suggest that sulfides replaced the primary Fe-oxyhydroxides prior to transformation

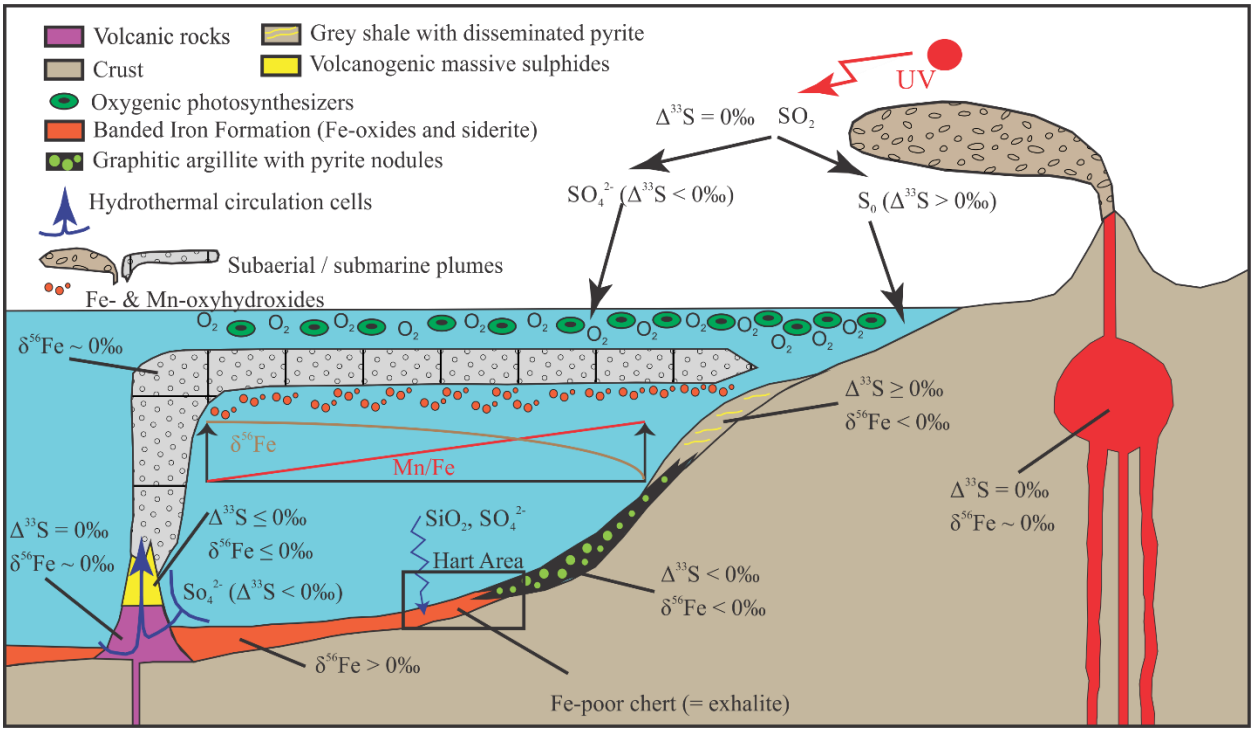

Figure 33: Cartoon cross-section showing the location of the Hart area within the basin during deposition. Iron formations were deposited deeper in the basin, with heavier Fe-isotope values, and the Hart exhalite and graphitic argillite formed in shallower water in a zone of upwelling (based on the models of Klein 2005; Beukes and Gutzmer 2008; and Bekker et al., 2010).

of Fe-oxyhydroxides to magnetite during late diagenesis or metamorphism. The negative $\Delta^{33}S$ values and variable $\delta^{34}S$ values indicate that sulfides were formed through reduction, potentially bacterial, of sulfate likely derived from a nearly homogenous seawater reservoir. Considering the sign of the MIF anomaly, such sulfate reservoir was likely derived from sulfate formed via photochemical reactions in the Archean oxygen-free atmosphere (Ono et al., 2003). The formation of the sulfide phase in these Fe-rich laminae should have been limited by the availability of H_2S, not Fe, and as such, pyrrhotite formed instead of pyrite, as is the case in modern environments where availability of S is the limiting factor (Kao et al., 2004; Larrasoana et al., 2007). Importantly, the pyrrhotite, or amorphous Fe monosulfide precursor to pyrrhotite, did not form at the same time as the exhalite precipitated, but are diagenetic products that must have crystallized before or at approximately the same time as chert precipitated, occluding permeability and porosity and halting bacterial sulfate reduction. Subsequent reaction, and recrystallization, of pyrrhotite to form pyrite could have occurred anaerobically under conditions of increased S availability or Fe-loss (Qian et al., 2011).

4.8 Conclusions and Basin Scale Implications

The low concentrations of Zn, U, and U_{auth}, and non-zero $\Delta^{33}S$ values all suggest that exhalite deposition in the Hart area of the Neoarchean Abitibi greenstone belt took place prior to the rise of atmospheric oxygen (cf. Farquhar et al., 2003; Scott et al., 2008, 2013; Partin et al., 2013a, b; Gumsley et al., 2017). However, Mn enrichment and highly negative Fe isotope values in both the exhalite and graphitic argillite require presence of oxygen at least in the upper part of the water column throughout the spreading path of the hydrothermal plume in a deep-water setting. Trace element data and $\delta^{56}Fe$ values indicate that the exhalite formed with the significant influence of a hydrothermal fluid on water composition, although distally from the hydrothermal source with the regionally mapped BIF occurring more proximal to the hydrothermal source.

The presence of the interbedded exhalite and graphitic argillite suggests that these rocks were deposited in a relatively deep-water environment, as shown by their fine-grain size and absence of sedimentary structures indicative of deposition above the fair-weather and storm-wave base, possibly at the upslope transition from iron formation to black shales in the basinal profile proposed by Klein (2005), Beukes and Gutzmer (2008), and Bekker et al. (2010), representing shallower water depth than the stratigraphically equivalent BIFs elsewhere in the region. Fractionation of Fe isotopes during precipitation of Fe-oxyhydroxides could have resulted in the heavier isotopes being removed via deposition of iron formations in deeper parts of the basin, as represented by iron formations mapped at the correlative stratigraphic level elsewhere in the Shaw Dome (Houlé et al., 2010b; Figure 34). The basin margins sustained high organic productivity, as indicated by the abundance of carbon in the graphitic argillite. Due to deposition of the exhalite distally to the hydrothermal centres, the iron formation and exhalite in the Hart area are unusually chert-rich, with lower concentration of Fe-oxides, Fe-carbonates, and Fe-silicates than in typical iron formations. Early diagenetic bacterial sulfate reduction at the depositional site of exhalite led to the formation of significant amounts of sulfides, however, the limited availability of sulfur with respect to iron during deposition of the exhalite unit could have resulted in the formation of pyrrhotite instead of pyrite as the primary sulfide mineral. Our study indicates spatial and temporal variability of seawater redox conditions and chemical composition in Archean deep-water settings at ~2.7 Ga, during a time when atmosphere stayed persistently anoxic.

4.9 REFERENCES

Alt, J.C. 1995. Sulfur isotopic profile through the oceanic crust: Sulfur mobility and seawater-crustal sulfur exchange during hydrothermal alteration. Geology, 23; 585-588.

Anbar, A.D., Duan, Y., Lyons, T.W., Arnold, G.L., Kendall, B., Creaser, R.A., Kaufman, A.J., Gordon, G.W., Scott, C., Garvin, J., Buick, R. 2007. A whiff of oxygen before the great oxidation event? Science, 317; 1906-1906.

Archer, C., Vance, D. 2006. Coupled Fe and S isotope evidence for Archean microbial Fe(III) and sulfate reduction. Geology, 42; 153-156.

Ayer, J., Amelin, Y., Corfu, F., Kamo, S., Ketchum, J., Kwok, K., Trowell, N. 2002. Evolution of the southern Abitibi greenstone belt based on U–Pb geochronology: autochthonous volcanic construction followed by plutonism, regional deformation and sedimentation. Precambrian Research, 115; 63-95.

Ayer, J.A., Thurston, P.C., Bateman, R., Dubé, B., Gibson, H.L., Hamilton, M.A., Hathway, B., Hocker, S.M., Houlé, M.G., Hudak, G., Ispolatov, V.O., Lafrance, B., Lesher, C.M., MacDonald, P.J., Péloquin, A.S., Piercey, S.J., Reed, L.E., Thompson, P.H. 2005. Overview of results from the Greenstone Architecture Project: Discover Abitibi Initiative; Ontario Geological Survey, Open File Report 6154, 146 p.

Balci, N., Bullen, T.D., Witte-Lien, K., Shanks, W.C., Motelica, M., Mandernack, K.W. 2006. Iron isotope fractionation during microbially stimulated Fe(II) oxidation and Fe(III) precipitation. Geochimica et Cosmochimica Acta, 70; 622-639.

Barrie, C.T. 2005. Geochemistry of exhalites and graphitic argillites near VMS and gold deposits: Ontario Geological Survey Miscellaneous Release Data 173, 126 p.

Bau, M. 1999. Scavenging of dissolved yttrium and rare earths by precipitation iron oxyhydroxide: Experimental evidence for Ce oxidation, Y-Ho fractionation, and lanthanide tetrad effect. Geochimica et Cosmochimica Acta, 63; 67-77.

Bau, M., Dulski, P. 1996. Distribution of yttrium and rare-earth elements in the Penge and Kuruman iron-formations, Transvaal Supergroup, South Africa. Precambrian Research, 79; 37-55.

Beard, B., Handler, R.M., Scherer, M.M., Wu, L., Czaja, A.D., Heimann, A., Johnson, C.M. 2010. Iron isotope fractionation between aqueous ferrous iron and goethite. Earth and Planetary Science Letters, 295; 241-250.

Beard, B.L., Johnson, C.M., Skulan, J.L., Nealson, K.H., Cox, L., Sun, H. 2003. Application of Fe isotopes to tracing the geochemical and biological cycling of Fe. Chemical Geology, 195; 87-117.

Bekker, A., Holland, H.D., Wang, P.-L., Rumble III, D., Stein, H.J., Hannah, J.L., Coetzee, L., Beukes, N.J. 2004. Dating the rise of atmospheric oxygen. Nature, 427; 117-120.

Bekker, A., Barley, M.E., Fiorentini, M.L., Rouxel, O.J., Rumble, D., Beresford, S.W. 2009. Atmospheric sulfur in Archean komatiite-hosted nickel deposits. Science, 326; 1086-1089.

Bekker, A., Slack, J.F., Planavsky, N., Krapež, B., Hofmann, A., Konhauser, K.O., Rouxel, O.J. 2010. Iron formation: the sedimentary product of a complex interplay among mantle, tectonic, oceanic, and biospheric processes. Economic Geology, 105; 467-508.

Bennett, S.A., Rouxel, O., Schmidt, K., Garbe-Schonberg, D., Statham, P.J., German, C.R. 2009. Iron isotope fractionation in a buoyant hydrothermal plume, 5 degrees S Mid-Atlantic Ridge. Geochimica et Cosmochimica Acta, 73; 5619-5634.

Beukes, N.J., Gutzmer, J. 2008. Origin and paleoenvironmental significance of major iron formations at the Archean–Paleoproterozoic boundary; in Banded iron formation-related high-grade iron ore, Society of Economic Geologists, Reviews in Economic Geology, 15; 5-47.

Bjerrum, C.J., Canfield, D.E. 2002. Ocean productivity before about 1.9 Gyr ago limited by phosphorus adsorption onto iron oxides. Nature, 417; 159-162.

Bolhar, R., Kamber, B.S., Moorbath, S., Fedo, C.M., Whitehouse, M.J. 2004. Characterization of early Archaean chemical sediments by trace element signatures. Earth and Planetary Science Letters, 222; 43-60.

Bonatti, E., Kraemer, T, Rydell, H.S. 1972. Classification and genesis of submarine iron-manganese deposits. *In:* Ferromanganese deposits on the ocean floor. IDOE, Columbia Univ. N.Y. pp.149–166.

Böstrom, K., Peterson, M.N.A., Joensuu, O., Fisher, D.E. 1969. Aluminum-poor ferromanganoan sediments on active oceanic ridges. Journal of Geophysical Research, 74; 3261.

Böstrom, K., Kraemer, T., Gartner, S. 1973. Provenance and accumulation rates of opaline silica, Al, Ti, Fe, Mn, Cu, Ni and Co in Pacific pelagic sediments. Chemical Geology, 11; 123-148.

Brunner, B., Bernasconi, S.M. 2005. A revised isotope fractionation model for dissimilatory sulfate reduction in sulfate reducing bacteria. Geochimica et Cosmochimica Acta, 69; 4759-4771.

Busigny, V., Planavsky, N.J., Jezequel, D., Crowe, S., Louvat, P., Moureau, J., Viollier, E., Lyons, T.W. 2014. Iron isotopes in an Archean ocean analogue. Geochimica et Cosmochimica Acta, 133; 443-462.

Butler, I.B., Archer, C., Vance, D., Oldroyd, A., Rickard, D. 2005. Fe isotope fractionation on FeS formation in ambient aqueous solution. Earth and Planetary Science Letters, 236; 430-442.

Chever, F., Rouxel, O., Croot, P.L., Ponzevera, E., Wuttig, K., Auro, M. 2015. Total dissolvable and dissolved iron isotopes in the water column of the Peru upwelling regime. Geochimica et Cosmochimica Acta, 162; 66–82.

Coplen, T.B., Krouse, H.R. 1998. Sulphur isotope data consistency improved. Nature, 392; 32.

Croal, L.R., Johnson, C.M., Beard, B.L., Newman, D.K. 2004. Iron isotope fractionation by Fe(II)-oxidizing photoautotrophic bacteria. Geochimica et Cosmochimica Acta, 68; 1227-1242.

Crosby, H.A., Roden, E.E., Johnson, C.M., Beard, B.L. 2007. The mechanisms of iron isotope fractionation produced during dissimilatory Fe(III) reduction by Shewanella putrefaciens and Geobacter sulfurreducens. Geobiology, 5; 169-189.

Dauphas, N., John, S., Rouxel, O. 2017. Iron Isotope Systematics. Reviews in Mineralogy & Geochemistry, 82; 415 - 510.

Detmers, J., Bruchert, V., Habicht, K.S., Kuever, J. 2001. Diversity of sulfur isotope fractionation by sulfate-reducing prokaryotes. Applied and Environmental Microbiology, 67; 888-894.

Duan, Y., Severmann, S., Anbar, A.D., Lyons, T.W., Gordon, G.W., Sageman, B.B. 2010. Isotopic evidence for Fe cycling and repartitioning in ancient oxygen-deficient settings: Examples from black shales of the mid-to-late Devonian Appalachian basin. Earth and Planetary Science Letters, 290; 244-253.

Farquhar, J., Wing, B.A. 2003. Multiple sulfur isotopes and the evolution of the atmosphere. Earth and Planetary Science Letters, 213; 1-13.

Farquhar, J., Bao, H., Thiemens, M. 2000. Atmospheric influence of Earth's earliest sulfur cycle. Science, 289; 756-758.

Farquhar, J., Savarino, J., Airieau, S., Thiemens, M.H. 2001. Observation of wavelength-sensitive mass-independent sulfur isotope effects during SO_2 photolysis: Implications for the early atmosphere. Journal of Geophysical Research, 106; 32829-32839.

Farquhar, J., Wing, B.A., McKeegan, K.D., Harris, J.W., Cartigny, P., Thiemens, M.H. 2002. Mass-independent sulfur of inclusions in diamond and sulfur recycling on early earth. Science, 298; 2369-2372.

Fralick, P., Riding, R. 2015. Steep Rock Lake: Sedimentology and geochemistry of an Archean carbonate platform. Earth-Science Reviews, 151; 132-175.

Frei, R., Dahl, P.S., Duke, E.F., Frei, K.M., Hansen, T.R., Frandsson, M.M., Jensen, L.A. 2008. Trace element and isotopic characterization of Neoarchean and Paleoproterozoic iron formation in the Black Hills (South Dakota, USA): Assessment of chemical change during 2.9-1.9 Ga deposition bracketing the 2.4-2.2 Ga first rise of atmospheric oxygen. Precambrian Research, 162; 441-474.

German, C.R., Holliday, B.P., Elderfield, H. 1991. Redox cycling of rare earth elements in the suboxic zone of the Black Sea. Geochimica et Cosmochimica Acta, 55; 3553-3558.

Guilbaud, R., Butler, I.B., Ellam, R.M. 2011. Abiotic Pyrite Formation Produces a Large Fe Isotope Fractionation. Science, 332; 1548-1551.

Gumsley, A.P., Chamberlain, K.R., Bleeker, W., Söderlund, U., de Kock, M.O., Larsson, E.R., Bekker, A. 2017. Timing and tempo of the great oxidation event. PNAS, 114; 1811-1816.

Habicht, K.S., Gade, M., Thamdrup, B., Berg, P., Canfield, D.E. 2002. Calibration of the sulfate levels in the Archean ocean. Science, 298; 2372-2374.

Haugaard, R., Ootes, L., Konhauser, K. 2017. Neoarchaean banded iron formation within a ~2620 Ma turbidite-dominated deep water basin, Slave craton, NW Canada. Precambrian Research, 292; 130-151.

Heimann, A., Johnson, C.M., Beard, B.L., Valley, J.W., Roden, E.E., Spicuzza, M.J., Beukes, N.J. 2010. Fe, C, and O isotope compositions of banded iron formation carbonates demonstrate a major role for dissimilatory iron reduction in similar to 2.5 Ga marine environments. Earth and Planetary Science Letters, 294; 8-18.

Hiebert, R.S., Bekker, A., Wing, B.A., Rouxel, O.J. 2013. The role of paragneiss assimilation in the origin of the Voisey's Bay Ni-Cu sulfide deposit, Labrador: multiple S and Fe isotope evidence. Economic Geology, 108; 1459-1469.

Hiebert, R.S., Bekker, A., Houlé, M.G., Wing, B.A., Rouxel, O.J. 2016. Tracing sources of crustal contamination using multiple S and Fe isotopes in the Hart komatiite-associated Ni-Cu-(PGE) sulphide deposit, Abitibi greenstone belt, Ontario, Canada. Mineralium Deposita, 51; 919-935.

Houlé, M.G., Lesher, C.M. 2011. Komatiite-associated Ni-Cu-(PGE) deposits, Abitibi greenstone belt, Superior Province, Canada; in Magmatic Ni-Cu and PGE deposits: geology, geochemistry, and genesis. Society of Economic Geologists, Reviews in Economic Geology, 17; 89-121.

Houlé, M.G., Lesher, C.M., Gibson, H.L., Ayer, J.A., Hall, L.A.F. 2010a. Localization of komatiite-associated Ni-Cu-(PGE) deposits in the Shaw Dome, Abitibi greenstone belt, Superior Province. In: Abstracts, 11th International Platinum Symposium, 21–24 June 2010, Sudbury, Ontario, Canada, Ontario Geological Survey, Miscellaneous Release—Data 269.

Houlé, M.G., Lesher, C.M., Préfontaine, S., Ayer, J.A., Berger, B.R., Taranovic, V., Davis, P.C., Atkinson, B. 2010b. Stratigraphy and physical volcanology of komatiites and associated Ni-Cu-(PGE)

mineralization in the western Abitibi greenstone belt, Timmins area, Ontario: a field trip for the 11th International Platinum Symposium; Ontario Geological Survey, Open File Report 6255, 99p.

Isley, A. 1995. Hydrothermal plumes and the delivery of iron to banded iron formations. Journal of Geology, 103; 169-185.

Jamieson, J.W., Wing, B.A., Farquhar, J., Hannington, M.D. 2013. Neoarchean seawater sulphate concentrations from sulphur isotopes in massive sulphide ore. Nature Geoscience, 6; 61-64.

Johnston, D.T., Farquhar, J., Wing, B.A., Kaufman, A.J., Canfield, D.E., Habicht, K.S. 2005. Multiple sulfur isotope fractionations in biological systems: A case study with sulfate reducers and sulfur disproportionators. American Journal of Science, 305; 645-660.

Kamber, B.S. 2010. Archean mafic-ultramafic volcanic landmasses and their effect on ocean-atmosphere chemistry. Chemical Geology, 274; 19-28.

Kao, S.-J., Horng, C.-S., Roberts, A.P., Liu, K.-K. 2004. Carbon-sulfur-iron relationships in sedimentary rocks from southwestern Taiwan: influence of geochemical environment on greigite and pyrrhotite formation. Chemical Geology, 203; 153-168.

Kaufman, A.J., Johnston, D.T., Farquhar, J., Masterson, A.L., Lyons, T.W., Bates, S., Anbar, A.D., Arnold, G.L., Garvin, J., Buick, R. 2007. Late Archean biospheric oxygenation and atmospheric evolution. Science, 317; 1900-1903.

Kato, Y., Yamaguchi, K.E., Ohmoto, H. 2006. Rare earth elements in Precambrian banded iron formations: Secular changes of Ce and Eu anomalies and evolution of atmospheric oxygen. Geological Society of America Memoir, 198; 269-289.

Ketchum, J.W.F., Ayer, J.A., Van Breemen, O. 2008. Pericontinental Crustal Growth of the southwestern Abitibi Subprovince, Canada: U-Pb, Hf, and Nd Isotopic Evidence. Economic Geology, 103; 1151-1184.

Klein, C. 2005. Some Precambrian banded iron-formations (BIFs) from around the world: Their age, geologic setting, mineralogy, metamorphism, geochemistry, and origin. American Mineralogist, 90; 1473-1499.

Konhauser, K.O., Lalonde, S.V., Planavsky, N.J., Pecoits, E., Lyons, T.W., Mojzsis, S.J., Rouxel, O.J., Barley, M.E., Rosiere, C., Fralick, P.W., Kum, L.R., Bekker, A. 2011. Aerobic bacterial pyrite oxidation and acid rock drainage during the Great Oxidation Event. Nature, 478; 369-373.

Kurzweil, F., Wille, M., Gantert, N., Beukes, N.J., Schoenberg, R. 2016. Manganese oxide shuttling in pre-GOE oceans – evidence from molybdenum and iron isotopes. Earth and Planetary Science Letters, 452; 69-78.

Lalonde, S.V., Konhauser, K.O. 2015. Benthic perspective on Earth's oldest evidence for oxygenic photosynthesis. Proceedings of the National Academy of Sciences, 112; 995-1000.

Lantink, M.L., Oonk, P.B.H., Floor, G.H., Tsikos, H., Mason, P.R.D. 2018. Fe isotopes of a 2.4 Ga hematite-rich IF constrain marine redox conditions around the GOE. Precambrian Research, 305; 218-235.

Larrasoana J.C., Roberts, A.P., Musgrave, R.J., Gracia, E., Pinero, E., Vega, M., Martinez-Ruiz, F. 2007. Diagenetic formation of greigite and pyrrhotite in gas hydrate marine sedimentary systems. Earth and Planetary Science Letters, 261; 350-366.

Li, W.Q., Beard, B.L., Johnson, C.M. 2015. Biologically recycled continental iron is a major component in banded iron formations. Proceedings of the National Academy of Sciences of the United States of America, 112; 8193-8198.

Lough, A.J.M., Klar, J.K., Homoky, W.B., Comer-Warner, S.A., Milton, J.A., Connelly, D.P., James, R.H., Mills, R.A. 2017. Opposing authigenic controls on the isotopic signature of dissolved iron in hydrothermal plumes. Geochimica et Cosmochimica Acta, 202; 1-20.

Lyons, T.W., Reinhard, C.T., Planavsky, N.J. 2014. The rise of oxygen in Earth's early ocean and atmosphere. Nature, 506; 307-315.

Marin-Carbonne, J., Rollion-Bard, C., Bekker, A., Rouxel, O., Agangi, A., Cavalazzi, B., Wohlgemuth-Ueberwasser, C.C. 2014. Coupled Fe and S isotope variations in pyrite nodules from Archean shale. Earth and Planetary Science Letters, 392; 67-79.

Maynard, J.B., 2010. The chemistry of manganese ores through time: a signal of increasing diversity of earth-surface environments. Economic Geology, 105; 535–552.

Maynard, J.B., Sutton, S.J., Rumble III, D., Bekker, A. 2013. Mass-independently fractionated sulfur in Archean paleosols: a large reservoir of negative $\Delta^{33}S$ anomaly on the early Earth. Chemical Geology, 362; 74-81.

Mendes, M., Lobato, L.M., Kunzmann, M., Halverson, G.P., Rosiere, C.A. 2017. Iron isotope and REE+Y composition of the Caue banded iron formation and related iron ores of the Quadrilaero Ferrifero, Brazil. Mineralium Deposita, 52; 159-180.

Olson, S.L., Kump, L.R., Kasting, J.F. 2013. Quantifying the areal extent and dissolved oxygen concentrations of Archean oxygen oases. Chemical Geology, 362; 35-43.

Ono, S., Eigenbrode, J.L., Pavlov, A.A., Kharecha, P., Rumble III, D., Kasting, J.F., Freeman, K.H. 2003. New insights into Archean sulfur cycle from mass-independent sulfur isotope records from the Hamersley Basin, Australia. Earth and Planetary Science Letters, 213; 15-30.

Ono, S., Beukes, N.J., Rumble, D. 2009. Origin of two distinct multiple-sulfur isotope compositions of pyrite in the 2.5 Ga Klein Naute Formation, Griqualand West Basin, South Africa. Precambrian Research, 169; 48-57.

Ossa Ossa, F., Hofmann, A., Vidal, O., Kramers, J.D., Belyanin, G., Cavalazzi, B. 2016. Unusual manganese enrichment in the Mesoarchean Mozaan Group, Pongola Supergroup, South Africa. Precambrian Research, 281; 414-433.

Partin, C.A., Bekker, A., Planavsky, N.J., Scott, C.T., Gill, B.C., Podkovyrov, V., Maslov, A., Konhauser, K.O., Lalonde, S.V., Love, G.D., Poulton, S.W., Lyons, T.W. 2013a. Large-scale fluctualtions in Precambrian atmospheric and oceanic oxygen levels from the record of U in shales. Earth and Planetary Science Letters, 369-370; 284-293.

Partin, C.A., Lalonde, S.V., Planavsky, N.J., Bekker, A., Rouxel, O.J., Lyons, T.W., Konhauser, K.O. 2013b. Uranium in iron formations and the rise of atmospheric oxygen. Chemical Geology, 362; 82-90.

Pavlov, A.A., Kasting, J.F. 2002. Mass-Independent Fractionation of Sulfur Isotopes in Archean Sediments: Strong Evidence for an Anoxic Archean Atmosphere. Astrobiology, 2; 27-41.

Pecoits, S., Gingras, M.K., Barley, M.E., Kappler, A., Posth, N.R., Konhauser, K.O. 2009. Petrography and geochemistry of the Dales Gorge banded iron formation: Paragenetic sequence, source and implications for palaeo-ocean chemistry. Precambrian Research, 172; 163-187.

Percak-Dennett, E.M., Beard, B.L., Xu, H., Konishi, H., Johnson, C.M., Roden, E.E. 2011. Iron isotope fractionation during microbial dissimilatory iron oxide reduction in simulated Archaean seawater. Geobiology, 9; 205–220.

Planavsky, N., Bekker, A., Rouxel, O.J., Kamber, B., Hofmann, A., Knudsen, A., Lyons, T.W. 2010. Rare Earth Element and yttrium compositions of Archean and Paleoproterozoic Fe formations

revisited: New perspectives on the significance and mechanisms of deposition. Geochimica et Cosmochimica Acta, 74; 6387-6405.

Planavsky, N., Rouxel, O.J., Bekker, A., Hofmann, A., Little, C.T.S., Lyons, T.W. 2012. Iron isotope composition of some Archean and Proterozoic iron formations. Geochimica et Cosmochimica Acta, 80; 158-169.

Planavsky, N.J., Reinhard, C.T., Wang, X., Thomson, D., McGoldrick, P., Rainbird, R.H., Johnson, T., Fischer, W.W., Lyons, W. 2014. Low Mid-Proterozoic atmospheric oxygen levels and the delayed rise of animals. Science, 346; 635-638.

Qian, G., Xia, F., Brugger, J., Skinner, W.M., Bei, J., Chen, G., Pring, A. 2011. Replacement of pyrrhotite by pyrite and marcasite under hydrothermal conditions up to 220°C: An experimental study of reaction textures and mechanisms. American Mineralogist, 96; 1878-1893.

Reinhard, C.T., Raiswell, R., Scott, C., Anbar, A.D., Lyons, T.W., 2009. A late Archean sulfidic sea stimulated by early oxidative weathering of the continents. Science, 326; 713-716.

Riding, R., Fralick, P., Liang, L. 2014. Identification of an Archean marine oxygen oasis. Precambrian Research, 251; 232-237.

Ridler, R.H. 1971. Analysis of Archean volcanic basins in the Canadian Shield using the exhalite concept. Bulletin of the Canadian Institute of Mining and Metallurgy, 64; 20.

Ripley, E.M. 1999. Systematics of sulphur and oxygen isotopes in mafic igneous rocks and Cu-Ni-PGE mineralization; in Dynamic processes in magmatic ore deposits and their application in mineral exploration. Geological Association of Canada, Short Course Notes, v.13, pp.111-158.

Robbins, L.J., Lalonde, S.V., Saito, M.A., Planavsky, N.J., Mloszewska, A.M., Pecoits, E., Scott, C., Dupont, C.L., Kappler, A., Konhauser, K.O. 2013. Authigenic iron oxide proies for marine zinc over geological time and implications for eukaryotic metallome evolution. Geobiology, 11; 295-306.

Rouxel, O., Dobbek, N., Ludden, J., Fouquet, Y. 2003. Iron isotope fractionation during oceanic crust alteration. Chemical Geology, 202; 155-182.

Rouxel, O.J., Bekker, A., Edwards, K.J. 2005. Iron isotope constraints of the Archean and Paleoproterozoic ocean redox state. Science, 307; 1088-1091.

Rouxel, O., Shanks III, W.C., Bach, W. and Edwards, K.J. 2008a. Integrated Fe- and S-isotope study of seafloor hydrothermal vents at East Pacific Rise 9-10°N. Chemical Geology, 252; 214-227

Rouxel, O., Sholkovitz, E., Charette, M., Edwards, K.J. 2008b. Iron isotope fractionation in subterranean estuaries. Geochimica et Cosmochimica Acta, 72; 3413-3430.

Rouxel, O., Toner, B.M., Manganini, S.J., German, C.R. 2016. Geochemistry and iron isotope systematics of hydrothermal plume fall-out at East Pacific Rise 9 degrees 50 ' N. Chemical Geology, 441 ; 212-234.

Rouxel, O., Toner, B., Germain, Y., Glazer, B. 2018. Geochemical and iron isotopic insights into hydrothermal iron oxyhydroxide deposit formation at Loihi Seamount. Geochimica et Cosmochimica Acta, 220; 449-482.

Rudnick, R.L., Gao, S. 2014. Composition of the Continental Crust. Treatise on Geochemistry (Second Edition) 4, 1-51.

Scott, C., Lyons, T.W., Bekker, A., Shen, Y., Poulton, S.W., Chu, X., Anbar, A.D. 2008. Tracing the stepwise oxygenation of the Proterozoic ocean. Nature, 452; 456-459.

Scott, C., Planavsky, N.J., Dupont, C.L., Kendall, B., Gill, B.C., Robbins, L.J., Husband, K.F., Arnold, G.L., Wing, B.A., Poulton, S.W., Bekker, A., Anbar, A.D., Konhauser, K.O., Lyons, T.W. 2013. Bioavailability of zinc in marine systems through time. Nature Geoscience, 6; 125-128.

Slack, J.F., Grenne, T., Bekker, A., Rouxel, O.J., Lindberg, P.A. 2007. Suboxic deep seawater in the late Paleoproterozoic: Evidence from hematitic chert and iron formation related to seafloor-hydrothermal sulfide deposits, central Arizona, USA. Earth and Planetary Science Letters, 255; 243-256.

Swanner, E.D., Planavsky, N.J., Lalonde, S.V., Robbins, L.J., Bekker, A., Rouxel, O.J., Saito, M.A., Kappler, A., Mojzsis, S.J., Konhauser, K.O. 2014. Cobalt and marine redox evolution. Earth and Planetary Science Letters, 390; 253-263.

Tangalos, G.E., Beard, B.L., Johnson, C.M., Alpers, C.N., Shelobolina, E.S., Xu, H., Konishi, H., Roden, E.E. 2010. Microbial production of isotopically light iron(II) in a modern chemically precipitated sediment and implications for isotopic variations in ancient rocks. Geobiology, 8; 197-208.

Thompson, P.H. 2005. A new metamorphic framework for gold exploration in the Timmins–Kirkland Lake area, western Abitibi greenstone belt: Discover Abitibi Initiative; Ontario Geological Survey, Open File Report 6162, 104p.

Thurston, P.C., Chivers, K.M. 1990. Secular variation in greenstone sequence development emphasizing Superior Province, Canada. Precambrian Research, 46; 21-58.

Thurston, P.C. 2008. Depositional gaps in Abitibi greenstone belt stratigraphy: a key to exploration for syngenetic mineralization. Economic Geology, 103; 1097-1134.

Thurston, P.C., Kamber, B.S., Whitehouse, M. 2012. Archean cherts in banded iron formation: insight into Neoarchean ocean chemistry and depositional processes. Precambrian Research, 214-215; 227-257.

Tsikos, H., Matthews, A., Erel, Y., Moore, J.M. 2010. Iron isotopes constrain biochemical redox cycling of iron and manganese in a Palaeoproterozoic stratified basin. Earth and Planetary Science Letters, 298; 125-134.

van den Boorn, S.H.J.M., van Bergen, M.J., Vroon, P.Z., de Vries, S.T., Nijman, W. 2010. Silicon isotope and trace element constraints on the origin of ~3.5 Ga cherts: Implications for Early Archaean marine environments. Geochimica et Cosmochimica Acta, 74; 1077-1103.

von Blanckenburg, F., Mamberti, M., Schoenberg, R., Kamber, B.S., Webb, G.E. 2008. The iron isotope composition of a microbial carbonate. Chemical Geology, 249; 113-128.

Wu, L.L., Beard, B.L., Roden, E.E., Johnson, C.M. 2011. Stable Iron Isotope Fractionation Between Aqueous Fe(II) and Hydrous Ferric Oxide. Environmental Science and Technology, 45; 1847-1852.

Yamaguchi, K.E., Johnson, C.M., Beard, B.L., Ohmoto, H. 2005. Biogeochemical cycling of iron in the Archean-Paleoproterozoic Earth: Constraints from iron isotope variations in sedimentary rocks from the Kaapvaal and Pilbara Cratons. Chemical Geology, 218; 135-169.

Chapter 5: Conclusions

5.1 Answering the Key Questions

In the Introduction to this thesis, three key questions were asked: How can multiple S and Fe isotope data be used to interpret the environmental conditions recorded by the sedimentary rocks that are the major contaminants that triggered sulfur saturation and the formation of the Voisey's Bay and Hart Ni-Cu-(PGE) deposits? Can multiple S and Fe isotope data identify the source of contamination in these deposits and be used to vector towards zones of mineralization? To answer these questions, three research projects were completed. The first project, at the Voisey's Bay Ni-Cu-(PGE) deposit, primarily used the relationship between $\delta^{33}S$ and $\delta^{34}S$ to identify the signature of bacterial sulfate reduction in the Tasiuyak Gneiss and mineralized zones of the Voisey's Bay troctolite, linking the deposit to the source of S. The second project, at the Hart komatiite-associated Ni-Cu-(PGE) deposit, used $\delta^{34}S$, $\Delta^{33}S$, and $\delta^{56}Fe$ to link the two mineralized zones to two different dominant S sources, and showed that these isotope systems (primarily $\Delta^{33}S$ and $\delta^{56}Fe$) can be used to vector towards the deposit at a range of a few hundred metres. The third project, again in the Hart deposit area, examined the depositional and diagenetic environmental conditions of formation of the exhalite and graphitic argillite units, with anomalously high Mn concentrations, suggesting that localized, or possibly transient, oxygen oases existed in this area during the time of deposition when the seawater composition was generally anoxic.

The Tasiuyak Gneiss at Voisey's Bay, and the exhalite and graphitic argillite units at Hart, are identified as the sources of sulfur for the Voisey's Bay and Hart deposits, respectively. Sulfides in all three sedimentary units were determined to have formed during diagenesis through bacterial sulfate reduction of seawater sulfate, and, in the case of the Archean Hart area sedimentary units, the sulfate had been mass-independently fractionated in the anoxic Archean atmosphere. The exhalite and graphitic argillite units at the Hart project are also interpreted to have been formed in marine

environments that had been influenced by hydrothermal plumes, although deposition was distal from the hydrothermal source. Additionally, the unusually low $\delta^{56}Fe$ values in the exhalite and graphitic argillite units of the Hart area are interpreted to be the result of Rayleigh fractionation of Fe isotopes from an expanding hydrothermal plume, where heavier isotopes of Fe are preferentially incorporated into Fe-oxides and Fe-oxyhydroxides forming oxide-facies iron formation closer to the hydrothermal source in the Hart area.

In both the Voisey's Bay and Hart mineralized zones, which typically have $\delta^{34}S$ data within the mantle range, multiple sulfur isotope data conclusively identified the sources of S contamination. Iron isotopes in the Voisey's Bay deposit were heavily buffered by the silicate magma, but could be used to identify contamination in the Hart deposit. The use of Fe isotope data to identify the source of magma contamination may be limited in some cases by a lack of understanding of potential fractionation of Fe isotopes in crystallizing magmas. The contamination at the Hart deposit formed distinct trends in the S isotope data, both vertically (up in the stratigraphy) and laterally within mineralized flows, where the data trended towards mantle values as distance from the mineralized zones increased. These trends could be used to identify the signature of contamination up to a few hundred meters from the mineralized zones, and could be used to vector towards a mineralized zone in this area.

Data from both the Hart and Voisey's Bay deposits indicates that the multiple sulfur isotope techniques are less sensitive to increasing R-factor than iron isotopes. As such, multiple elements or isotopes should be used to calculate R-factor. These should be selected based on: initial concentration in the sulfide xenomelt, initial concentration in the silicate magma, and, for elements, partition coefficient between silicate and sulfide liquids. This will ensure that the combination of the elements or isotopes used will result in a range of the estimated R-factor, thus reducing error.

5.2 Limitations of Interpretations

In the Voisey's Bay project (Chapter 2), the primary limitation on the interpretation is the error on the relationship between $\delta^{33}S$ and $\delta^{34}S$ (i.e. the slope on a plot of $\delta^{33}S^*$ vs. $\delta^{34}S^*$). In the case of the Nain gneiss, the relationship was defined by only 2 points, leaving the potential for the relationship to be dramatically changed by the addition of more data. Additionally, no trend could be generated for the enderbitic gneiss, although this was due to a lack of S in the enderbitic gneiss samples, so it is unlikely the enderbitic gneiss was a significant S source. However, the range of possible slopes within errors, producing multiple possible pathways for S isotope fractionation may be the most problematic, requiring geologic control to determine the most valid interpretation. More data would likely reduce the overall error on these relationships, leading to a more robust interpretation.

In the Hart deposit project (Chapter 3), there are two main limitations on the interpretation of the data. The first is the lack of understanding of Fe isotope fractionation at magmatic temperatures, which leads to uncertainty in identifying the signature of contamination in the mineralized zones. Additionally, the high concentration of Fe in the komatiitic magma leads to the isotopic signature of the contaminant being unidentifiable at relatively low R-factors, effectively eliminating the Fe isotope system's usefulness as a vector towards mineralization. More work is needed to identify and constrain Fe isotope fractionation in real magmas between different Fe-bearing silicate minerals and between silicates and sulfides.

The second limitation on the interpretation of the data in the Hart deposit project is the overlapping ranges in isotope values ($\delta^{56}Fe$, $\Delta^{33}S$ and $\delta^{34}S$) for the potential contaminant lithologies (exhalite and graphitic argillite). The $\delta^{56}Fe$ and $\Delta^{33}S$ values have similar ranges in exhalite and graphitic argillite, making it impossible to distinguish the two potential contaminants with these values alone. However, the $\delta^{34}S$ values, although typically within the mantle range in the mineralized zones at the Hart deposit,

were the most useful in distinguishing between the two potential sedimentary S sources. The range of $\delta^{34}S$ values for the exhalite and graphitic argillite did overlap, leading to some uncertainty in the interpretation, but exhalite tended to have negative values, whereas the graphitic argillite tended to have positive values, allowing for some confidence in the interpretation of sedimentary S source. Other geochemical proxies for contamination (e.g. REEs, trace elements, Re-Os isotopes, etc.) may be useful to provide a clear distinction between the exhalite and graphitic argillite that can be used as a signature of contamination in komatiite.

In the Hart area sedimentary rock project (Chapter 4), the largest limitation may be the limited understanding of how the redox conditions of the oceans changed from the Archean, through the GOE in the early Proterozoic, and into the Phanerozoic. The concept of oxygen oases in the Archean seawater is relatively recent, and, although it fits some of the geochemical data for the exhalite in the Hart area, it is not supported by all the data, such as the trace element data that suggests anoxic conditions. Further study is warranted to determine the nature and extent, both in space and in time, of these oxygen oases.